

On the propagation of pressure and flow waves through the patient specific arterial system

Citation for published version (APA):

Bessems, D. (2007). *On the propagation of pressure and flow waves through the patient specific arterial system*. [Phd Thesis 1 (Research TU/e / Graduation TU/e), Biomedical Engineering]. Technische Universiteit Eindhoven. <https://doi.org/10.6100/IR629017>

DOI:

[10.6100/IR629017](https://doi.org/10.6100/IR629017)

Document status and date:

Published: 01/01/2007

Document Version:

Publisher's PDF, also known as Version of Record (includes final page, issue and volume numbers)

Please check the document version of this publication:

- A submitted manuscript is the version of the article upon submission and before peer-review. There can be important differences between the submitted version and the official published version of record. People interested in the research are advised to contact the author for the final version of the publication, or visit the DOI to the publisher's website.
- The final author version and the galley proof are versions of the publication after peer review.
- The final published version features the final layout of the paper including the volume, issue and page numbers.

[Link to publication](#)

General rights

Copyright and moral rights for the publications made accessible in the public portal are retained by the authors and/or other copyright owners and it is a condition of accessing publications that users recognise and abide by the legal requirements associated with these rights.

- Users may download and print one copy of any publication from the public portal for the purpose of private study or research.
- You may not further distribute the material or use it for any profit-making activity or commercial gain
- You may freely distribute the URL identifying the publication in the public portal.

If the publication is distributed under the terms of Article 25fa of the Dutch Copyright Act, indicated by the "Taverne" license above, please follow below link for the End User Agreement:

www.tue.nl/taverne

Take down policy

If you believe that this document breaches copyright please contact us at:

openaccess@tue.nl

providing details and we will investigate your claim.

**On the propagation of pressure
and flow waves through the
patient-specific arterial system**

A catalogue record is available from the Eindhoven University of Technology Library

ISBN: 978-90-386-1091-7

Cover design: David Bessems & Bregje Schoffelen, Oranje Vormgevers
Printed by Universiteitsdrukkerij TU Eindhoven, Eindhoven, The Netherlands.

This research was performed in the scope of the hemodyn project, a cooperation between Philips Medical systems (Healthcare IT - Advanced Development), Best, the Technische Universiteit Eindhoven (Biomedical Engineering department), Eindhoven and the Erasmus University (Thoraxcenter, Biomedical Engineering), Rotterdam. The Hemodyn project is partly funded by SenterNovem (Dutch Ministry of economic affairs).

On the propagation of pressure and flow waves through the patient specific arterial system

PROEFSCHRIFT

ter verkrijging van de graad van doctor
aan de Technische Universiteit Eindhoven,
op gezag van de Rector Magnificus, prof.dr.ir. C.J. van Duijn,
voor een commissie aangewezen door het College voor Promoties
in het openbaar te verdedigen op
woensdag 19 september 2007 om 16.00 uur

door

David Bessems

geboren te Maastricht

Dit proefschrift is goedgekeurd door de promotor:

prof.dr.ir. F.N. van de Vosse

Copromotoren:

dr.ir. M.C.M. Rutten

en

dr.ir. M. Breeuwer

Contents

Summary	vii
1 General Introduction	1
1.1 Physiology and Pathology	4
1.2 Computational aspects	6
1.3 Objective and outline	8
2 A wave propagation model of blood flow using an approximate velocity profile function.	11
2.1 Introduction	12
2.2 Theory	13
2.2.1 Conservation of mass and momentum in one dimension	13
2.2.2 An approximate velocity profile function	15
2.2.3 Viscous layer thickness	18
2.2.4 Wave propagation	19
2.2.5 General set of equations	21
2.2.6 Computational method	21
2.3 Results	22
2.3.1 Velocity profile function	22
2.3.2 Wave propagation	24
2.4 Discussion	28
2.5 Conclusion	30
3 A time-domain based wave propagation model of blood flow in viscoelastic vessels	31
3.1 Introduction	32
3.2 Methods	32
3.2.1 Numerical methods	32
3.2.2 Solid model	33
3.2.3 Experimental setup	36
3.2.4 Parameter estimation	38
3.3 Results	40
3.4 Discussion	44
3.5 Conclusion	47

4	The pressure drop over arterial stenoses under physiological conditions	49
4.1	Introduction	50
4.2	Methods	51
4.3	Results	53
4.4	Discussion	62
4.5	Conclusion	66
5	The pressure drop over aneurysms under physiological conditions	67
5.1	Introduction	68
5.2	Methods	69
5.3	Results	71
5.4	Discussion	79
5.5	Conclusion	82
6	Application and general discussion	83
6.1	Introduction	84
6.2	Methods	84
6.2.1	Boundary conditions	86
6.2.2	Stenoses and aneurysms	87
6.2.3	Computational Method	88
6.2.4	Physiological data	89
6.3	Results	94
6.4	General Discussion	102
6.4.1	Model restrictions	103
6.4.2	Perspectives	105
6.5	Conclusion	105
	References	106
A	Derivation of non-linear part	111
B	Spatial discretisation	113
C	Linearisation of equations	117
	Samenvatting	119
	Dankwoord	121
	curriculum vitae	123

Summary

On the propagation of pressure and flow waves through the patient-specific arterial system

For pre-operative decision making in cardiovascular surgery, patient-specific physiological data are needed. These data (e.g. pressure, flow and wall shear stress) can be obtained using a computational model of the arterial system. Because of the high computational costs involved with fully three-dimensional models of the total arterial tree, one-dimensional wave propagation models are more suited to provide clinically relevant information. Current models of the arterial system are based on assumptions concerning the frictional and convection forces in the one-dimensional momentum balance that yield an inaccurate representation of the physiological situation. Moreover, the constitutive law, relating the local pressure to the local cross-sectional area, is usually based on purely elastic material properties of the arterial wall, whereas arteries are known to possess viscoelastic properties as well. Furthermore, standard one-dimensional wave propagation methods are based on the assumption of fluid flow through straight or slightly tapered vessels where the velocity component in the radial direction is negligibly small with respect to its axial counterpart. In pathological regions such as stenoses and aneurysms these assumption do not hold.

In the current study, a one-dimensional wave propagation model is developed, using an approximate velocity profile function to provide an estimate for the frictional forces and the non-linear term. The resulting wall shear stress and convection forces are compared to the analytical solution for pulsatile flow in a rigid tube showing good agreement. With respect to the arterial wall, a constitutive law, based on the viscoelastic behaviour of the standard linear solid model is introduced, that relates the local cross-sectional area of the vessel lumen to the local blood pressure. The resulting one-dimensional wave propagation model is validated by a comparison to data obtained from an experimental setup, modelling fluid flow through straight and tapered polyurethane vessels. In order to apply the one-dimensional wave propagation model to patient-specific arterial systems, a bifurcation model is implemented to relate the pressure and flow of the parent artery to the pressure and flow of the child arteries. Also, terminal impedances based on a three-element Windkessel model are introduced to obtain appropriate boundary conditions at the truncated ends of the arterial network. Furthermore, to accurately model the fluid dynamics near pathological regions, such as stenoses and aneurysms, relations between the pressure drop

and flow characteristics as a function of the local geometry are developed. These relations are based on the results of a computational study of blood flow through two-dimensional axisymmetric stenoses and aneurysm models. The final model is applied to an idealised arterial network known from literature to investigate the influence of the different model assumptions made on the pressure, the flow and on the wall shear stress. The pressure and flow waves computed using the approximate velocity profile function, show only moderate changes with respect to those obtained using Poiseuille profiles. The resulting wall shear stress, however, does differ significantly. The introduced viscoelastic properties of the arterial wall are shown to significantly contribute to the pressure and flow wave attenuation and the influence of a femoral stenoses and an abdominal aortic aneurysms has been demonstrated. In conclusion, the resulting one-dimensional wave propagation model can be used to obtain clinically relevant information that may be crucial in surgical planning.

Chapter 1

General Introduction

Since ancient times, the detection of the arterial blood pulse has been used to diagnose arterial abnormalities and diseases. In ancient Greek civilisation it was believed that a good physician could diagnose diseases and even detect early pregnancy solely by palpation of the arterial pulse, without any knowledge of the underlying physiological phenomena. From studying the arterial system of the deceased, they thought the arterial system was filled with air and the pulsatile sensation was attributed to an active dilation of the arteries (from the Greek 'aer' and 'trachea' which literally means 'air duct') to draw vital spirits from the airways (Tortora and Anagnostakos (1990)). Today, our knowledge of the cardiovascular system is much more elaborate, but as long as cardiovascular diseases are the number one cause of death in Western civilisation, still many problems remain to be solved.

In the various disciplines of cardiovascular surgery, patient-specific physiological data are needed for the diagnosis and treatment of arterial diseases, and also in the understanding of the processes responsible for the development of pathological states. Both the blood pressure and the blood flow through each individual artery are known to be important physiological parameters related to the condition of the arterial wall, since the blood pressure regulates the arterial wall thickness through its effect on wall tension and the flow regulates the lumen diameter by means of the resulting wall shear stress (Pritchard et al. (1995)). The local blood flow is also important to quantify the perfusion of each individual organ. The severity of a stenosis, e.g. can be determined by the blood pressure and flow distal to the obstructed vessel and the risk of rupture of an aneurysm can be predicted when the vessel wall morphology and the stresses exerted on this dilated wall are known.

During the last decades, non-invasive imaging techniques such as magnetic resonance imaging (MRI) and computed tomography (CT) have become an important aid in obtaining clinically relevant data. They are used in the diagnosis, qualification and quantification of arterial diseases and also for post-operative evaluation of a possible intervention. Some crucial information, such as the blood pressure and the wall shear stress, however, cannot easily be deduced using imaging techniques. Also, these images provide information on the current status of a pathological region only, whereas for pre-operative decision making the surgeon should have access to a predictive tool to evaluate intervention alternatives.

To obtain clinically relevant information such as the blood pressure, the blood velocity and the wall shear stress from MR images or CT scans, computational models of blood flow through segmented volumes of these images can be used. By virtually altering the geometries of the segmentation obtained, also intervention alternatives can be modelled and thereby evaluated.

In the next sections the physiology and pathologies of the arterial system will briefly be discussed and an overview will be presented on the computational methods used in the modelling of the arterial system. From thereon, the objective of this work will be stated and the outline of this thesis will be presented.

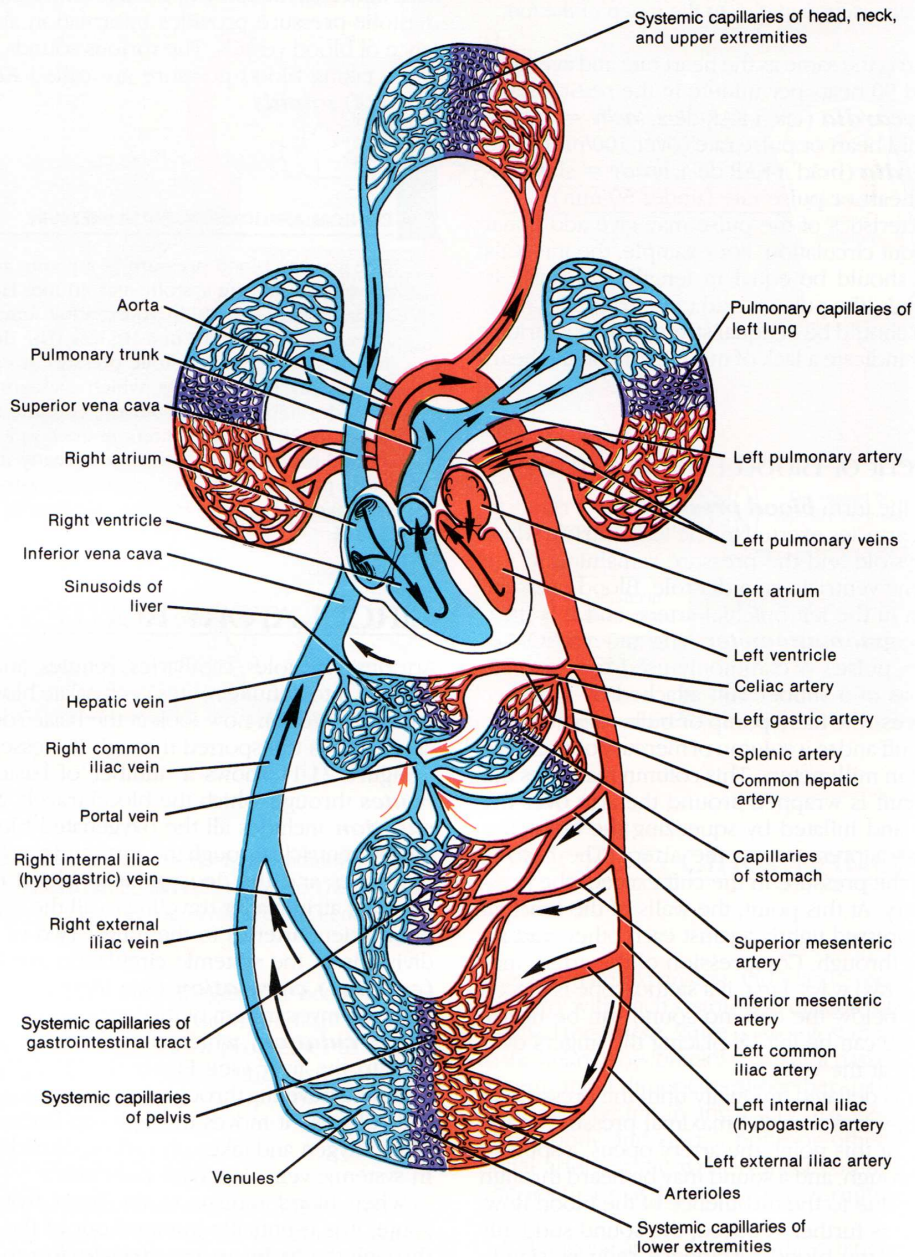


Figure 1.1: Schematic representation of the human circulatory system. From Tortora and Anagnostakos (1990)

1.1 Physiology and Pathology

The cardiovascular system as schematically depicted in figure 1.1 consists of the heart and the vascular system. It takes care of the transport of nutrients, oxygen, carbon oxide and other solutes between organs in the mammalian body using blood as a carrier. The heart is a four-chambered pump that propels blood around the circulatory system by contraction and relaxation of the cardiac muscle. The circulatory or vascular system can be divided into the systemic and the pulmonary circulation. The systemic circulation transports oxygenated blood from the left ventricle to all tissues of the body and transports the deoxygenated blood to the right atrium. The pulmonary circulation transports the deoxygenated blood from the right ventricle to the lungs where the blood is fully oxygenated again. It then returns it to the heart's left atrium to re-enter the systemic circulation. Although their purposes differ, the physical principals of the two circulations are similar. They both consist of a network of arteries, arterioles, capillaries, venules and veins. The arteries are responsible for the convective transport of blood to the tissue. The arterioles are the last small branches of the arterial system and their vascular walls are capable of dilating or (partly) closing the vessel lumen. Thereby, they can adapt the local blood flow to the needs of the tissue. The function of the capillaries is to exchange blood constituents with the surrounding tissue through the very thin capillary wall. Because the total cross-sectional area of the lumen of the capillaries in any organ is many times larger than the cross-sectional area of the lumen of the supplying artery, a low blood velocity is established in the capillaries allowing for enough time for oxygen, nutrients and waste products to be exchanged. The venules collect the blood from the capillaries to gradually reunite into progressively larger veins. The veins convey the blood from the tissue back to the heart. In the arterial system a high blood pressure is needed for the blood that leaves the arteries to pass through the highly resistive network of capillaries within each organ. To withstand such high pressures the arterial wall is much thicker than the walls of the venous system that transports blood under much lower pressures. Because most pathologies occur in these high pressure regions, focus will be on the arterial part of the systemic circulation.

The wall of the larger arteries is composed of three main layers, characterised by their structure and cell types. The internal layer or tunica intima is positioned at the luminal side of the vessel and is composed of an inner single layer of endothelial cells and a layer of elastic cells called the internal elastic lamina. The endothelial layer is in constant contact with blood and can be easily damaged e.g. by excessive shear stresses. The middle layer of the arteries, the tunica media, is usually the thickest layer, consisting of elastic fibres and smooth muscle cells. Depending on its region in the arterial system, the content and orientation of the elastic fibres and the smooth muscle cells in the tunica media vary to result in dominantly elastic mechanical properties for the larger arteries to a more viscoelastic behaviour for the smaller arteries. This viscoelastic behaviour is caused mainly by the smooth muscle cells (Humphrey (1995)) resulting in typical viscoelastic behaviour such as relaxation and creep. The outer layer of the arterial wall, the tunica externa (adventitia) is composed primarily of loose connective tissues and a network of elastic and collagenous fibres oriented in

a helical architecture around the vessel.

Blood consists mainly of blood plasma with red blood cells (erythrocytes), white blood cells (leucocytes) and blood platelets (thrombocytes). Its main functions are the transport of oxygen and other solutes, and the regulation of the body's pH and temperature. The erythrocytes, which occupy approximately 45% of the blood volume, dominate the rheological behaviour of the blood. In a low shear situation, the erythrocytes are brought in contact with each other which causes them to aggregate face to face. These aggregations are known as rouleaux and their presence results in an increase of the blood viscosity. At near zero shear the rouleaux will form three-dimensional structures, inducing an additional increase of the blood viscosity. At high shear rates the erythrocytes align with the flow and deform to decrease the viscosity, which is called shear thinning (Tortora and Anagnostakos (1990)). These complex properties of the erythrocytes are responsible for the complex macroscopic behaviour of blood.

As indicated previously, the normal functioning of the systemic circulation can be disturbed by abnormalities usually referred to as peripheral arterial diseases (PVD). In an advanced stage such PVD can cause the arterial system to no longer perform its primary goal, the satisfactory perfusion of each individual organ. The cause of most types of PVD is atherosclerosis, a common disease of the major blood vessels characterised by hardening of the arteries as a result of fatty streaks and deposits of cholesterol and calcium in the vessel walls. Atherosclerosis can lead to the local narrowing of a vessel's lumen. A significant narrowing of a vessel's lumen, also referred to as a stenosis, can result in a decreased blood flow to the arteries, arterioles and capillaries distal to the stenosis, leading to ischemia of the perfused organ. Another PVD that can be caused by atherosclerosis is a local dilation of the vessel wall, or aneurysm. They most frequently occur in the arteries of the circle of Willis and in the abdominal aorta. Aneurysms are usually asymptomatic, however, the dilated vessel can burst and lead to death at any time.

Peripheral vascular diseases can often be treated with exercise, a healthy diet and by quitting smoking. In case of a PVD in a more severe stage surgical intervention is required to maintain the patient's quality of life. A possible treatment of a stenosis in the peripheral arteries is balloon angioplasty, with or without stent placement. Balloon angioplasty is the mechanical widening of a narrowed blood vessel by inflating a balloon in the vessel lumen at the site of the stenosis. This balloon is positioned in the obstructed vessel by means of a guiding-catheter and optionally a stent is used to prevent recoil. An artery that is stenosed for a larger part of the vessel can be bypassed using either an autologous vein or a synthetic graft. The treatment of a severe aneurysm in the abdominal aorta that has not yet ruptured usually involves the placement of an artificial graft to exclude the aneurysm sac from the high systemic pressure, either by open surgery or by endovascular intervention.

In the next section, the computational methods that can be used in the diagnosis and treatment of the mentioned arterial diseases, will be discussed.

1.2 Computational aspects

Computational models of blood flow through the arterial system can be used to estimate parameters crucial for surgical planning. Much effort has been put into the development and validation of computational methods for fully three-dimensional analysis of time-dependent flow in distensible artery segments (see e.g. Taylor et al. (1998); Gijssen et al. (1999a,b); van de Vosse et al. (2003)). Using these methods, detailed pressure gradients, velocity fields and corresponding wall shear stresses can be obtained within the region of interest. As a result of the large amount of computer resources associated with these computations, however, most three-dimensional computational methods can only be applied to a small segment of the arterial system and hence appropriate assumptions on the proximal and distal part of the arterial tree must be provided. Suitable boundary conditions can be obtained by using appropriate simplified models of the total cardiovascular system, such as zero-dimensional lumped-parameter models (Pater and Berg (1964); Westerhof et al. (1969)) and one-dimensional wave propagation models in the frequency domain (Womersley (1957); Cox (1968, 1970)) and time domain (Anliker et al. (1971); Tsou et al. (1971); Hughes and Lubliner (1973); Stergiopoulos et al. (1992); Lagrée (2000); Olufsen and Peskin (2000); Formaggia et al. (2001); Wan et al. (2002); Sherwin et al. (2003); Wang and Parker (2004)). Some important phenomena of wave propagation are difficult to describe with lumped-parameter models, whereas the non-linear characteristics of the governing equations and the constitutive equations that describe the mechanical properties of the arterial wall cannot always be described in the frequency domain. Moreover, as three-dimensional patient-specific computational models are generally defined in the time domain, time-domain-based one-dimensional models are preferable for the provision of boundary conditions. They have been shown to be a simple tool in describing the propagation of the pressure and flow waves travelling through the arterial system (Schaaf (1972); Stergiopoulos et al. (1992); Olufsen and Peskin (2000); Sherwin et al. (2003); Wang and Parker (2004)) or through a segment of this system (Raines et al. (1974); Balar et al. (1989)). Moreover, using such one-dimensional wave propagation models, the surgical alternatives in treating an arterial pathology can be evaluated pre-operatively. Also, when appropriate estimates for the pressure and wall shear stress are obtained using a one-dimensional wave propagation model, the adaptation of the arterial system to changes in the peripheral resistance can be predicted. For instance, the adaptation of the arteries and veins after the introduction of an arteriovenous shunt in the lower arm can be computed to determine whether the increased flow through this extremity indeed results in the desired maturation of the concerned vessels.

In the derivation of a one-dimensional wave propagation model of the arterial system assumptions need to be made on the velocity profile as a function of the local flow characteristics, to obtain appropriate estimates for the frictional forces and non-linear forces in the one-dimensional balance-of-momentum equation. Current models assume either Poiseuille profiles (Schaaf (1972); Stergiopoulos et al. (1992); Wan et al. (2002); Wang and Parker (2004)) or the velocity profile to be some other function of the local flow (Hughes and Lubliner (1973); Olufsen and Peskin (2000); Formaggia

et al. (2001); Sherwin et al. (2003)), all resulting in frictional forces and non-linear forces that are in-phase with the flow. From a physical point of view, however, it is known that a phase difference can be present between the velocity in the core of the vessel and the velocity in a layer close to the vessel wall (Womersley (1957)), resulting in an out-of-phase behaviour of both the frictional forces and non-linear effects. Therefore, the velocity profile functions used today may yield an inaccurate representation of the pressure and flow wave propagation with respect to the physiological situation. Also, the wall shear stress obtained using these models may be inaccurate, resulting in an inappropriate stimulus for possible vessel wall remodelling.

With respect to the vessel wall behaviour, current one-dimensional wave propagation models of the arterial system in the time domain assume either linear elastic (Schaaf (1972); Raines et al. (1974); Sherwin et al. (2003); Wang and Parker (2004)) or non-linear elastic (Balar et al. (1989); Stergiopoulos et al. (1992); Olufsen and Peskin (2000)) material properties, thereby neglecting the viscoelastic properties of the arterial wall. These viscoelastic properties, mainly caused by the smooth muscle cells present in the tunica media of the arterial wall, are amongst others responsible for the attenuation of the pressure and flow waves travelling through the arterial tree and should, therefore, be taken into account in the modelling of the arterial system. Most one-dimensional wave propagation models in the frequency domain, as reviewed by Cox (1968), do model the arterial wall to be viscoelastic. In the frequency domain, however, the non-linear fluid mechanics cannot be incorporated so these methods are inappropriate in modelling one-dimensional wave propagation in the arterial system. The equations for one-dimensional wave propagation are derived under the assumption of fully developed flow through straight or slightly tapered vessels where the fluid velocity in radial direction is negligibly small with respect to its axial component. This assumption may well hold in healthy arteries, but in pathological regions such as stenoses and aneurysms where the lumen radius rapidly changes the flow is no longer fully developed. In these regions standard one-dimensional wave propagation theory cannot be applied. In the literature, several publications have appeared on the (time-dependent) velocity field and resulting wall shear stress in a stenotic region (Siouffi et al. (1984); Tu et al. (1992); Cavalcanti (1995); Tu and Deville (1996); Siouffi et al. (1998); Chakravarty and Mandal (2000); Long et al. (2001); Mandal (2005)). Because of its application in a one-dimensional wave propagation model, our interest however, is mainly on the axial pressure drop related to this velocity field. Among others, Stergiopoulos et al. (1992) introduced a stenosis model into a one-dimensional wave propagation model of the arterial system to investigate the effect of such a stenosis on the pressure and flow waves travelling through the arterial tree. This stenosis model was based on the work of Young (1979) where an empirical relation between the pressure drop over a PMMA model of a stenosis and the flow characteristics are determined as a function of the stenosis shape and its severity. This experimental work was performed in only one type of vessel with a constant frequency of the flow signal whereas we expect the pressure drop over a stenosis to depend on the oscillatory behaviour of the flow. For aneurysms, a lot of research has focussed on the time-dependent velocity field and corresponding stresses exerted on the dilated vessel wall (Wille (1981); Perktold (1987); Rathish-Kumar and

Naidu (1996); Egelhoff et al. (1999); Finol et al. (2003); Wolters et al. (2005); Deplano et al. (2007)). The pressure drop over aneurysms as a function of the flow characteristics through the dilated vessel, however, has not yet been investigated.

1.3 Objective and outline

As indicated in the previous paragraphs, one-dimensional wave propagation models of blood flow through the patient-specific arterial system may be an aid in the diagnosis and treatment of arterial diseases. The models used today, however, lack several crucial features with respect to the modelling of the patient-specific arterial tree. First, a velocity profile function should be incorporated that takes into account the phase difference between the core velocity and the blood velocity in a layer close to the vessel wall, to obtain appropriate estimates for the frictional forces and non-linear term in the one-dimensional momentum balance. Also, a constitutive relation that models the non-linear viscoelastic arterial wall behaviour should be developed to properly relate the local instantaneous cross-sectional area of the vessel lumen to the local instantaneous pressure in one-dimensional wave propagation. Moreover, one-dimensional models of blood flow through pathological regions such as stenoses and aneurysms should be developed and incorporated into the one-dimensional model of blood flow through the patient-specific arterial system. Therefore,

The main objective of this work is to develop a one-dimensional wave propagation model of the patient-specific arterial system that can be an aid in the diagnosis and treatment of arterial diseases, based on images obtained by MR or CT scanning.

For this purpose, the one-dimensional wave propagation model as proposed by Hughes and Lubliner (1973) is taken as a point of departure. Using this model, the propagation of pressure and flow waves through straight or slightly tapered vessels can be modelled. In chapter 2 (see also Bessems et al. (2007)) the model by Hughes and Lubliner (1973) is modified by introducing a velocity profile function that depends on the Womersley parameter α , the local flow and the local pressure gradient. It is based on the division of the blood flow through a vessel into an inviscid core flow near the axis of the vessel and a friction-dominated flow layer close to the vessel wall, allowing for a phase difference between these two regions. It will be shown that the velocity profile function obtained provides proper estimates for the wall shear stress and non-linear term and that introducing these into the one-dimensional balance-of-momentum equation influences the propagation of pressure and flow waves through the arterial system.

Chapter 3 focuses on the mechanical behaviour of the arterial wall in one-dimensional wave propagation. A differential equation, based on the viscoelastic behaviour of the standard linear-solid model is introduced to relate the vessel's instantaneous local cross-sectional area to the local instantaneous blood pressure. The resulting one-dimensional wave propagation model is validated by a comparison to the pressure and flow waves measured in an experimental setup.

In chapters 4 and 5 a two-dimensional axisymmetric computational model of blood flow through stenoses and aneurysms is used to define a relation between the pressure drop over these pathological regions and the local flow characteristics. By assuming that this pressure drop occurs linearly over the length of the pathological region, for both stenoses (chapter 4) and aneurysms (chapter 5) a one-dimensional balance-of-momentum equation can be derived that can be used in the modelling of the propagation of pressure and flow waves through such regions.

In chapter 6 the individual components introduced in chapters 2 through 5 will be combined into a model of the total arterial system. To this end, an interface relation is introduced that couples the individual arterial segments at their bifurcations. Moreover, appropriate boundary conditions at the proximal inlet and the truncated ends of the region of interest are proposed. Using the arterial tree as tabulated in Stergiopoulos et al. (1992), the influence of the different model parameters introduced in previous chapters is shown. Also, computations based on a patient-specific arterial system obtained from MR-images are performed and different alternatives of surgical intervention are evaluated.

At the end of this chapter, the main results of the present thesis are summarised and discussed, and recommendations are provided for further improvement of the current model. The content of the second and the third chapter are based on published and submitted articles respectively, which has resulted in recurrence and overlap between these chapters.

Chapter 2

A wave propagation model of blood flow using an approximate velocity profile function.

This chapter is based on: D. Bessems, M.C.M. Rutten and F.N. van de Vosse, *A wave propagation model of blood flow in large vessels using an approximate velocity profile function*, J. Fluid. Mech., **580**, 2007, 145–168.

2.1 Introduction

Propagation of pressure and flow waves in the arterial system and especially its influence on the development of stenotic regions, aneurysms and other vascular diseases has been subject of many studies (Anliker et al. (1971); Hughes and Lubliner (1973); Young and Tsai (1973b); Stergiopoulos et al. (1992); Olufsen and Peskin (2000); Lagr e (2000); Formaggia et al. (2001); Wan et al. (2002); Sherwin et al. (2003); Wang and Parker (2004)). Hemodynamic factors such as blood pressure and flow have received much attention as intraluminal pressure is found to regulate the arterial wall thickness through its effects on wall tension (Fung (1993)), whereas blood flow regulates the lumen diameter through changes in wall shear stress (Fung (1993)). To obtain detailed information on these crucial parameters in the development of atherosclerosis, much effort has been put into the development and validation of computational methods for fully three-dimensional analysis of time-dependent flow in distensible artery segments (see e.g. Taylor et al. (1998); Gijzen et al. (1999a,b); van de Vosse et al. (2003)). Using these methods, detailed velocity fields and pressure gradients can be obtained within the region of interest. As a result of the large amount of computer resources associated with these computations, however, most three-dimensional computational methods can only be applied to a small segment of the arterial system and hence appropriate assumptions on the proximal and distal part of the arterial tree must be provided. Suitable boundary conditions can be obtained by using appropriate simplified models of the total cardiovascular system, such as zero-dimensional lumped-parameter models (Pater and Berg (1964); Westerhof et al. (1969)) and one-dimensional wave propagation models in the frequency domain (Womersley (1957); Cox (1968, 1970)) and time domain (Tsou et al. (1971); Hughes and Lubliner (1973); Stergiopoulos et al. (1992); Olufsen and Peskin (2000); Formaggia et al. (2001); Wan et al. (2002); Sherwin et al. (2003); Wang and Parker (2004)).

Some important phenomena of wave propagation in the arterial system are difficult to describe with lumped-parameter models, whereas the non-linear characteristics of the governing equations and the constitutive equations that describe the mechanical properties of the arterial wall cannot always be described in the frequency domain. Moreover, as three-dimensional patient-specific computational models are generally defined in the time-domain, time domain-based one-dimensional models are preferable in the provision of boundary conditions. They have been shown to be a simple tool in describing the propagation of the pressure and flow waves travelling through the arterial system or through a segment of this system. When dealing with one-dimensional wave propagation formulations, assumptions need to be made on local velocity profiles in order to obtain proper estimates for the non-linear and friction term in the momentum equation integrated over the local cross-sectional area. The papers mentioned previously assume either a Poiseuille profile (Stergiopoulos et al. (1992); Wan et al. (2002); Wang and Parker (2004)) or the velocity profile to be some other function of the local flow (Hughes and Lubliner (1973); Olufsen and Peskin (2000); Formaggia et al. (2001); Sherwin et al. (2003)), both resulting in friction forces in phase with the flow. When interest is in the attenuation of the pressure wave and in the wall shear stress, however, these assumptions are insufficient as from a fluid dynamical point of view a phase difference between the wall shear stress and the local flow may occur as a result of a time-dependent phase difference between the velocity in the central core of the vessel and the velocity near the vessel wall.

In this chapter an approximate velocity profile function will be introduced, providing proper estimates for the non-linear and friction terms. In section 2.2, a mathematical formulation of the one-dimensional wave propagation theory for flow in large vessels according to Hughes and Lubliner (1973) will briefly be described. Then this theory will be extended by introducing a velocity profile function that depends on the Womersley parameter α , the local flow and the

pressure gradient. This model is different from the model proposed by Olufsen (1999) where a linear boundary layer profile was introduced, again not allowing for a phase difference between the boundary layer flow and the flow in the inviscid core of the vessel. The model is also different from the approach of Tsou et al. (1971) where the velocity profile is represented by a third-degree polynomial expansion where the coefficients depend on time and axial position. In that case an extra equation has to be solved to obtain the coefficients of the expansion and no distinction between the viscous layer and the inviscid core can be made. In the work of Zagzoule et al. (1991) an asymptotic expression, relating the wall shear stress to the instantaneous flow, was deduced. The use of this expression in one-dimensional wave propagation, however, restricts the model to low Womersley number regions ($\alpha < 6$) so it cannot be used in the total physiological range of α . Lagrée (2000) closes the system of one-dimensional equations by defining a set of coefficients dependent solely on α , derived from Womersley's theory and based on the fundamental mode of the flow pulse. The resulting wall shear stress and non-linear term for single harmonic flow pulses closely approximate their analytical counterparts based on the Womersley theory. For multi-harmonic flow pulses at high values of α , however, the closure used by Lagrée no longer provides accurate estimates for the wall shear stress and the non-linear term, even for the case where the Womersley solution should be retained.

In this study approximate profiles are derived by assuming inertia-dominated flow in the central core of the tube and friction-dominated flow near the vessel wall. Solutions in these areas are coupled using cross-sectional mass conservation, allowing for profiles different from Womersley profiles based on a single harmonic. This approach allows the possibility of extending the method to constitutive models for which no analytical solution is available and non-harmonic input, provided that a reasonable distinction between the central core and the viscous layer can be modelled.

In section 2.3, the friction term obtained from the theory proposed in this study is compared to the one presented in Young and Tsai (1973b) based on Womersley's solution in the frequency domain (Womersley (1957)). The non-linear term is compared to the one obtained directly from velocity profiles derived from Womersley's theory. Finally, the effect of the friction term on wave propagation is illustrated by comparing the pressure gradient and flow resulting from wave propagation using our velocity profile approximation with wave propagation using Poiseuille friction, in a physiological range.

2.2 Theory

2.2.1 Conservation of mass and momentum in one dimension

The derivation of the governing equations for one-dimensional wave propagation in incompressible fluids, including outflow due to branching, is taken from Hughes and Lubliner (1973). Based on the Reynolds transport theorem, the differential equations for conservation of mass and momentum balance are derived for a geometry such as depicted in figure 2.1. The integrated continuity equation in area-velocity (A, \bar{v}_z)-formulation is written as

$$\frac{\partial A}{\partial t} + \frac{\partial}{\partial z}(A\bar{v}_z) + \Psi = 0, \quad (2.1)$$

with t being the time, z the axial coordinate, A the local cross-sectional area and Ψ the volumetric outflow per unit length. The fluid velocity $\mathbf{v} = (v_x, v_y, v_z)$ in the axial direction is denoted by v_z and an overbar indicates the cross-sectional mean. The physiologically more relevant pressure-flow (p, q)-formulation can be obtained by introducing a constitutive relation

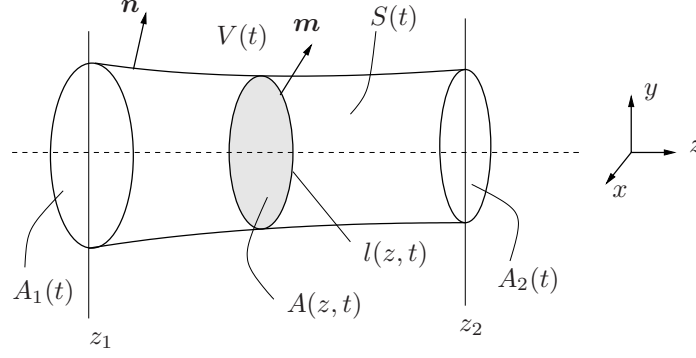


Figure 2.1: The geometry of part of a vessel along the z -axis, bound by cross-sectional surfaces $A_1(z=z_1)$ and $A_2(z=z_2)$ and circumferential surface S . The total volume is denoted by the symbol V , an arbitrary cross-section perpendicular to the z -axis by A and its boundary by l .

expressing the response of the vessel wall to pressure variations. For reasons of simplicity, here an $A = A(p(t))$ relation is chosen according to

$$\frac{\partial A}{\partial t} = \frac{\partial A}{\partial p} \frac{\partial p}{\partial t} \equiv C \frac{\partial p}{\partial t}, \quad (2.2)$$

but more complicated and viscoelastic properties can also be modelled. Here $C(z, t)$ is the compliance of the vessel which can be obtained either from experimental data or from a constitutive model of the arterial wall. A more detailed description of the constitutive model used in this chapter is presented in section 2.3. After introducing volume flow $q \equiv A\bar{v}_z$, the following (p, q) -formulation can be derived:

$$C \frac{\partial p}{\partial t} + \frac{\partial q}{\partial z} + \Psi = 0. \quad (2.3)$$

When assuming a no-slip condition for the local velocity profile, the momentum balance from Hughes and Lubliner (1973) can be written as:

$$\frac{\partial q}{\partial t} + \frac{\partial A\bar{v}_z^2}{\partial z} + \frac{A}{\rho} \frac{\partial p}{\partial z} = Af_z + \oint_l \left(\frac{\eta}{\rho} \frac{\partial v_z}{\partial \mathbf{m}} \right) dl + A \frac{\eta}{\rho} \frac{\partial^2 \bar{v}_z}{\partial z^2}. \quad (2.4)$$

Here, f_z are the body forces acting on the fluid in axial direction and $\mathbf{m} = (m_x, m_y, 0)$ is the outward normal to l . The fluid density and viscosity are referred to as ρ and η respectively. The last term on the right of (2.4) is obtained by retaining the diffusion forces in the derivation from Hughes and Lubliner (1973). We choose to keep this term for reasons of numerical stability. Equation (2.4) is the one-dimensional momentum balance in an (A, q) -formulation. For a more thorough derivation of the above equations, see Hughes and Lubliner (1973). On using the approximation of a perfectly circular lumen

$$\oint_l \frac{\eta}{\rho} \frac{\partial v_z}{\partial \mathbf{m}} dl \approx \frac{2\pi a}{\rho} \tau_w \quad (2.5)$$

with τ_w as the wall shear stress and a the lumen radius, and the definition

$$\gamma \equiv A\overline{v_z^2} = \int_A v_z^2 dA, \quad (2.6)$$

equation (2.4) becomes

$$\frac{\partial q}{\partial t} + \frac{\partial \gamma}{\partial z} + \frac{A}{\rho} \frac{\partial p}{\partial z} = Af_z + \frac{2\pi a}{\rho} \tau_w + \frac{\eta}{\rho} \frac{\partial^2 q}{\partial z^2}, \quad (2.7)$$

where the last term on the right-hand side has been derived using the Leibniz theorem in combination with boundary conditions $v_z|_{r=a} = 0$ and $\partial v_z/\partial z|_{r=0} = 0$. Note that (2.5) is exact for circular cross-sections A but can be generalised for non-circular cross-sections using $a = \sqrt{A/\pi}$. The term γ will be referred to as the (non-linear) convection term. To solve (2.7) with respect to the pressure p and the flow q in combination with the one-dimensional mass conservation equation (2.2) and a constitutive relation between p and A , more information about the local velocity profile v_z is needed to provide proper estimates for the convection term γ (2.6) and the wall shear stress τ_w (2.5), expressed in terms of p and q . Note that, for this, we do not need an exact description of the velocity profile as long as we have good approximations for the integral of its square and its derivative at the wall. Whereas previous work in the time domain used mainly flat or Poiseuille profiles, in this work an alternative profile function will be derived to approximate the above terms, as will be presented next.

2.2.2 An approximate velocity profile function

Here a relation for $v(\mathbf{x}, t)$ expressed in terms of $p(z, t)$ and $q(z, t)$ is derived to provide proper estimates for the convection term γ and the friction term τ_w . Hughes and Lubliner (1973) provide the following expression:

$$\mathbf{v}_A = \mathbf{0} \quad \text{and} \quad v_z(\mathbf{x}_A, t) = \phi(x, y)\overline{v}_z(z, t) \quad (2.8)$$

with ϕ such that the axial velocity at the wall is zero (and so $\phi|_l = 0$) and the mean cross-sectional velocity equals $\overline{v}_z(z, t)$. This formulation implies that in all cases the shape of the profile is both constant over time and constant along the axis of the vessel. From a mathematical point of view this is a convenient choice that will simplify the momentum equation (2.4) significantly. From a physical perspective, however, the choice presented in (2.8) is less obvious. As the velocity in the core of the vessel does not need to be in-phase with the velocity in the outer layer, a velocity profile that changes its shape in time must be chosen.

Here we consider the Navier-Stokes equations for fully developed flow in straight tubes driven by a given pressure gradient

$$\rho \frac{\partial v_z}{\partial t} = -\frac{\partial p}{\partial z} + \eta \frac{1}{r} \frac{\partial}{\partial r} \left(r \frac{\partial v_z}{\partial r} \right) \quad (2.9)$$

with $r = \sqrt{x^2 + y^2}$ as the radial coordinate. We will consider the situation as depicted on the left in figure 2.2. To obtain a good approximation of the solution of (2.9) close to the wall, we take the limit as r approaches a

$$\lim_{r \rightarrow a} \left(\rho \frac{\partial v_z}{\partial t} \right) = \lim_{r \rightarrow a} \left(-\frac{\partial p}{\partial z} + \eta \frac{1}{r} \frac{\partial}{\partial r} \left(r \frac{\partial v_z}{\partial r} \right) \right) \quad (2.10)$$

Owing to the no-slip condition at the wall, the left-hand side of (2.10) will be zero. As the pressure gradient is constant over the cross-sectional area, we have

$$0 = -\frac{\partial p}{\partial z} + \lim_{r \rightarrow a} \left(\eta \frac{1}{r} \frac{\partial}{\partial r} \left(r \frac{\partial v_z}{\partial r} \right) \right) \quad (2.11)$$

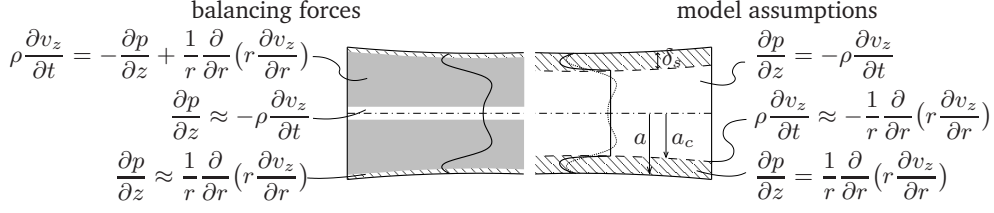


Figure 2.2: The geometry of part of a vessel with local radius a . The present fluid dynamical forces are shown on the left and on the right our approximation, where a_c is the core radius and $\delta_s = a - a_c$ the viscous layer. The solid curve on the left represents an exact velocity profile and the solid curve on the right the approximation according to our method.

close to the wall. In the central core viscous forces are assumed to be negligible, so

$$\rho \frac{\partial v_z}{\partial t} = -\frac{\partial p}{\partial z}, \quad (2.12)$$

which implies a flat profile in this region. In the region between these two limiting cases the grey area is defined (see figure 2.2) where all three terms should balance according to equation (2.9). In this area the velocity profile will be continuous and bounded both by the velocity near the wall and the velocity in the central core. Exact solutions of (2.9), providing exact velocity profiles, can only be derived in the frequency domain (Womersley (1957)). As our only interest is in providing reasonable approximations for the non-linear term $\gamma = \int v_z^2 dA$ and the friction term $\partial v_z / \partial r|_{r=a}$ any other velocity profile doing so is admissible, as long as mass conservation $\int v_z dA$ is satisfied. We chose to model the limiting case where the grey area of figure 2.2 becomes infinitesimally small, leaving only the inviscid area in the central core and the purely viscous layer near the vessel wall as depicted on the right in figure 2.2. At the transition between these two areas we connect the velocity v_z in the viscous layer to the velocity in the central core v_c , which is still unknown but can be eliminated (written in terms of q) using cross-sectional mass conservation. A first-order estimate of the thickness of the viscous layer δ_s for fully developed flow in straight rigid tubes is derived from the equilibrium between inertia forces $\rho \partial v_z / \partial t$ and viscous forces $\eta \partial^2 v_z / \partial r^2$ at the transition from the viscous layer to the inviscid core. This yields $\delta_s = \mathcal{O}(\sqrt{\eta / \rho \omega}) = \mathcal{O}(a / \alpha)$, with α being the Womersley parameter and ω representing the angular frequency. Consequently, the central core is related to the Womersley parameter according to

$$\frac{a_c}{a} = \max \left[0, \left(1 - \frac{k}{\alpha} \right) \right] \quad \text{with} \quad \alpha = a \sqrt{\frac{\rho \omega}{\eta}} \quad \text{and} \quad k = \mathcal{O}(1), \quad (2.13)$$

where the exact value of k will be defined later in this section. For blood flow a rough estimation yields: $\eta / \rho \approx 6 \cdot 10^{-6}$ [m²/s] (Gijzen et al. (1999a)) and $\omega = 2\pi / T \approx 6$ [s⁻¹] resulting in $\delta_s \approx 1$ [mm] (specifically, $\delta_s \approx \min [a, 1 \text{ mm}]$) for all arteries. To incorporate the above into the velocity profile function the governing equations in the viscous layer will be solved for the axisymmetric case. This shall be done using proper boundary conditions to connect the velocity profile in this layer to the velocity in the central core. In this central core (2.12) results in a flat profile according to

$$v_z(r, z, t) = v_c(z, t) \quad \text{for} \quad r < a_c, \quad (2.14)$$

where v_c is left undetermined. In the viscous layer, equilibrium between the pressure gradient and the friction forces is assumed according to (2.11)

$$0 = -\frac{\partial p}{\partial z} + \eta \frac{1}{r} \frac{\partial}{\partial r} \left(r \frac{\partial v_z}{\partial r} \right) \quad \text{for } a_c \leq r < a. \quad (2.15)$$

After integration of (2.15) with respect to the radius r twice, together with the boundary conditions $v_z|_{r=a_c} = v_c$ and $v_z|_{r=a} = 0$ the following profile is obtained:

$$v_z = -\frac{a^2}{4\eta} \frac{\partial p}{\partial z} (1 - \xi^2) + \frac{\ln \xi}{\ln \xi_c} \left[v_c + \frac{a^2}{4\eta} \frac{\partial p}{\partial z} (1 - \xi_c^2) \right] \quad \text{for } a_c \leq r < a, \quad (2.16)$$

with $\xi = r/a$ the dimensionless radius, and $\xi_c = a_c/a$ the dimensionless core diameter. Integration of (2.14) and (2.16) over the cross-sectional area A results in a relation between the core velocity $v_c(z, t)$ and the cross-sectional mean velocity $\bar{v}_z \equiv q/A$ dependent on the radius of the core a_c and the pressure gradient $\partial p/\partial z$, according to

$$v_c = \left[\frac{\ln \zeta_c}{\zeta_c - 1} \right] \bar{v}_z + \frac{a^2}{4\eta} \left[1 - \zeta_c + \frac{1}{2} (\zeta_c + 1) \ln \zeta_c \right] \frac{\partial p}{\partial z}, \quad (2.17)$$

with $\zeta_c = \xi_c^2$.

Substitution of this relation in (2.16) yields an expression for the total velocity profile $v_z(\mathbf{x}, t)$:

$$v_z = \frac{-\ln \hat{\zeta}}{1 - \zeta_c} \bar{v}_z - \frac{a^2}{4\eta} \left[1 - \hat{\zeta} + \frac{1}{2} (\zeta_c + 1) \ln \hat{\zeta} \right] \frac{\partial p}{\partial z}, \quad (2.18)$$

with

$$\zeta = \xi^2 \quad \text{and} \quad \hat{\zeta} = \max [\zeta, \zeta_c]. \quad (2.19)$$

The simple relation (2.8) of Hughes and Lubliner (1973) is now replaced by the more complex one

$$v_z(\mathbf{x}, t) = \phi_1(\zeta, \zeta_c) \bar{v}_z(z, t) - \phi_2(\zeta, \zeta_c) \frac{a^2}{4\eta} \frac{\partial p(z, t)}{\partial z} \quad (2.20)$$

with ϕ_1 and ϕ_2 defined by:

$$\phi_1(\zeta, \zeta_c) = \frac{-\ln \hat{\zeta}}{1 - \zeta_c} \quad \text{and} \quad \phi_2(\zeta, \zeta_c) = 1 - \hat{\zeta} + \frac{1}{2} (\zeta_c + 1) \ln \hat{\zeta} \quad (2.21)$$

Note that, in cylindrical coordinates

$$\int_0^1 \phi_1 \xi d\xi = \frac{1}{2} \quad \text{and} \quad \int_0^1 \phi_2 \xi d\xi = 0 \quad (2.22)$$

and, consequently, the mean velocity does not depend on the second term on the right-hand side of (2.20). For the axisymmetric case the wall shear stress τ_w can be computed as

$$\tau_w \left(\frac{\partial p}{\partial z}, q, A, \xi_c \right) = \eta \frac{\partial v_z}{\partial r} \Big|_{r=a} = -\frac{2\eta}{(1 - \zeta_c)a} \frac{q}{A} + \frac{a}{4} (1 - \zeta_c) \frac{\partial p}{\partial z}. \quad (2.23)$$

A detailed derivation of the non-linear term $\gamma = \overline{Av^2_z}$ is presented in Appendix A, leading to the expression

$$\gamma\left(\frac{\partial p}{\partial z}, q, A, \xi_c\right) = \delta_1 \frac{q^2}{A} + \delta_2 q \frac{a^2}{4\eta} \frac{\partial p}{\partial z} + \delta_3 A \left(\frac{a^2}{4\eta} \frac{\partial p}{\partial z}\right)^2, \quad (2.24)$$

where δ_1 , δ_2 and δ_3 are functions dependent solely on the dimensionless core thickness ζ_c according to:

$$\left. \begin{aligned} \delta_1(\zeta_c) &= \int_0^1 \phi_1^2 d\zeta = \frac{2 - 2\zeta_c(1 - \ln \zeta_c)}{(1 - \zeta_c)^2} \\ \delta_2(\zeta_c) &= -2 \int_0^1 \phi_1 \phi_2 d\zeta = \frac{1 + 4\zeta_c(1 + \ln \zeta_c) - \zeta_c^2(5 - 2 \ln \zeta_c)}{1 - \zeta_c} \\ \delta_3(\zeta_c) &= \int_0^1 \phi_2^2 d\zeta = \frac{1}{3} + \zeta_c(3 + 2 \ln \zeta_c) - \zeta_c^2(3 - 2 \ln \zeta_c) - \frac{1}{3}\zeta_c^3. \end{aligned} \right\} \quad (2.25)$$

The resulting velocity profiles, corresponding wall shear stresses and non-linear forces at different Womersley numbers α will be compared to Womersley's theory in section 2.3.1.

2.2.3 Viscous layer thickness

The only parameter yet to be determined in order for the velocity profile function (and thus the wall shear stresses and non-linear forces) to be known, is the viscous layer thickness. A physically relevant value for this parameter must be provided as a function of the local geometry and the local fluid dynamical parameters. For friction-dominated flow ($\alpha < k$) Poiseuille friction can be recovered by substitution of

$$\frac{\partial p}{\partial z} = -R_0 q = \frac{-8\eta}{\pi a^4} q \quad (2.26)$$

into equation (2.23) and setting $\zeta_c = 0$. For inertia-dominated flow ($\alpha \gg 1$) (2.13) gives

$$1 - \zeta_c = 1 - \xi_c^2 \approx \frac{2k}{\alpha}. \quad (2.27)$$

Moreover,

$$\frac{\partial q}{\partial t} \approx -\frac{A}{\rho} \frac{\partial p}{\partial z} \quad (2.28)$$

or, on introducing the harmonic solutions $q = \hat{q} e^{i\omega t}$ and $p = \hat{p} e^{i\omega t}$

$$\hat{q} \approx \frac{iA}{\rho\omega} \frac{\partial \hat{p}}{\partial z}, \quad (2.29)$$

with \hat{p} and \hat{q} respectively the complex amplitude of p and q for each harmonic of the pressure. In this case, by substitution of (2.29), (2.27) and (2.13) into (2.23), the corresponding complex amplitude of the wall shear stress $\hat{\tau}_w$ becomes

$$\hat{\tau}_w = \frac{1}{\alpha} \left(k - i\frac{2}{k}\right) \hat{\tau}_w^p, \quad (2.30)$$

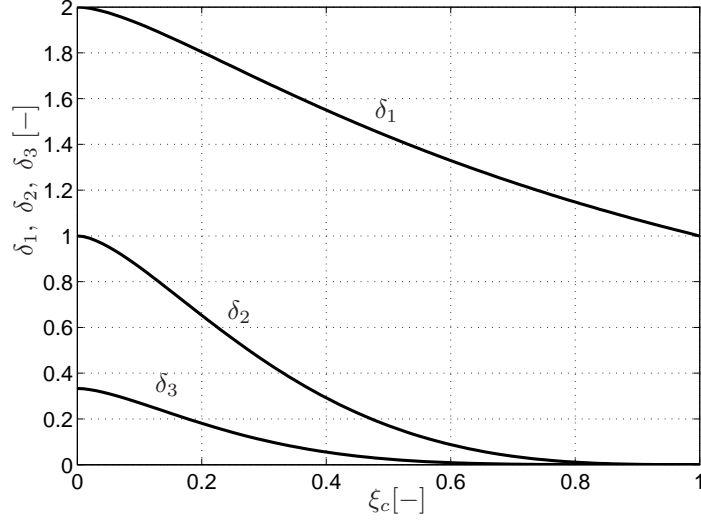


Figure 2.3: Parameters δ_1 , δ_2 , and δ_3 as a function of the core radius ξ_c .

with τ_w^p equal to the Poiseuille wall shear stress. As our main interest is in providing the proper wall shear stress, (2.30) is compared to Womersley's theory and for $k = \sqrt{2}$ they are fully equivalent. Consequently, for relatively cylindrical parts of the vessel (for $\partial A/\partial z \ll a$) and sufficiently far from geometrical discontinuities, the following approximation for ξ_c can be used:

$$\xi_c = \max [0, 1 - \sqrt{2}/\alpha]. \quad (2.31)$$

2.2.4 Wave propagation

In addition to the $(1 + \delta)q^2/A$ term in the original equation of Hughes and Lubliner (1973) extra non-linear terms now appear in $\gamma(p, q)$, given in (2.24). Since the multiplication factors corresponding to δ_i are of the same order of magnitude, the importance of the terms on the right-hand side of equation (2.24) depends on the magnitude of the functions δ_1 , δ_2 and δ_3 . These are plotted against the dimensionless core radius ξ_c in figure 2.3. The case of a Poiseuille flow, where $\zeta_c \rightarrow 0$ and $\partial p/\partial z = -(8\eta/a^2)\bar{v}_z$, yields $1 + \delta = \delta_1 - \delta_2 + \delta_3 = 4/3$. For a flat profile, $\zeta_c \rightarrow 1$, which results in $1 + \delta = \delta_1 = 1$, so both limiting cases are in complete correspondence with the original method. Since the influence of the non-linear term is important mainly for large arteries at high Womersley numbers ($\alpha \gg 1$ and so $\xi_c \rightarrow 1$), in the remainder of this work the contributions of δ_2 and δ_3 will be neglected (see figure 2.3), resulting in a non-linear term similar to the ones presented in the literature, e.g. Hughes and Lubliner (1973). The set of equations that follows from mass conservation, the momentum balance and a constitutive

law for the wall material, together with the profile function and the wall shear stress, is

$$\left. \begin{aligned} \frac{\partial A}{\partial t} + \frac{\partial q}{\partial z} + \Psi &= 0, \\ \frac{\partial q}{\partial t} + \frac{\partial}{\partial z} \left(\delta_1 \frac{q^2}{A} \right) + \frac{A}{\rho} \frac{\partial p}{\partial z} &= Af_z + \frac{2\pi a}{\rho} \tau_w + \frac{\eta}{\rho} \frac{\partial^2 q}{\partial z^2} \\ p(z, t) &= \tilde{p}(A(z, t); z, t), \end{aligned} \right\} \quad (2.32)$$

and

$$\left. \begin{aligned} v_z &= -\frac{\ln \hat{\zeta}}{1 - \zeta_c} \frac{q}{A} - \frac{a^2}{4\eta} \left[1 - \hat{\zeta} + \frac{1}{2}(\zeta_c + 1) \ln \hat{\zeta} \right] \frac{\partial p}{\partial z}, \\ \tau_w &= -\frac{2\eta}{(1 - \zeta_c)a} \frac{q}{A} + \frac{a}{4}(1 - \zeta_c) \frac{\partial p}{\partial z}, \end{aligned} \right\} \quad (2.33)$$

with γ , τ_w , $\hat{\zeta}$ and ζ_c from (2.24), (2.23), and (2.19) respectively. The constitutive law expresses a relation between the local instantaneous pressure $p(z, t)$ and the local instantaneous cross-sectional area $A(z, t)$ for which a linear approach will be proposed in the next section. For a comparison with results from Young and Tsai (1973b) later on, the friction term in (2.33) will now be revised into a comparable format. Introducing the coefficients c_p and c_q as

$$c_p = 1 + \frac{1}{2}(1 - \zeta_c), \quad c_q = \frac{1}{2}(1 - \zeta_c)^{-1}, \quad (2.34)$$

yields

$$\tau_w = -\frac{a}{2} \left[c_q R_0 q - (c_p - 1) \frac{\partial p}{\partial z} \right] \quad (2.35)$$

for the wall shear stress with the resistance R_0 per unit of length defined according to

$$R_0 = \frac{8\eta}{\pi a^4}. \quad (2.36)$$

Using equation (2.13) with $k = \sqrt{2}$ gives

$$c_q = \frac{\alpha}{4k} \left(1 - \frac{\sqrt{2}}{2\alpha} \right)^{-1}, \quad c_p = 1 + \frac{\sqrt{2}}{\alpha} \left(1 - \frac{\sqrt{2}}{2\alpha} \right) \quad \text{for } \alpha > \sqrt{2}. \quad (2.37)$$

For shear dominated flow in small arteries (quasi-static Poiseuille flow) a similar derivation gives $c_p + c_q = 2$ and since this is also the case for $\alpha = \sqrt{2}$, use of (2.37) gives

$$c_q = \frac{1}{2}, \quad c_p = \frac{3}{2} \quad \text{for } \alpha \leq \sqrt{2}. \quad (2.38)$$

Substitution of (2.35) into the momentum equation of (2.32) without external forces and neglecting the non-linear and diffusion terms gives

$$\frac{\partial p}{\partial z} = - \left[\frac{c_q}{2 - c_p} \right] R_0 q - \left[\frac{1}{2 - c_p} \right] L \frac{\partial q}{\partial t} \quad (2.39)$$

with $L = \rho/A$ [kg/m⁵] the inertance per unit of length.

2.2.5 General set of equations

To simplify the resulting set of equations for the general case a (p, q) -formulation with the pressure and the flow as parameters is proposed as this may be the best option with respect to linearisation in $A(z, t)$. The cross-sectional area can be derived from the pressure using the linearised constitutive relation:

$$A(z, t) = \tilde{A}(p(z, t), z) = A_0(z) + C_0(p - p_0) \quad (2.40)$$

with the compliance per unit length C_0 , based on thin walled cylinder theory for a linear elastic material, defined as

$$C_0 = \left. \frac{\partial A}{\partial p} \right|_{p=p_0} = \frac{2\pi(1-\mu^2)a_0^3}{hE}. \quad (2.41)$$

Here, μ is Poisson's ratio, E is Young's modulus and a_0 is the vessel radius at $p = p_0$. Using the p, q -formulation yields

$$\frac{\partial}{\partial t} \begin{bmatrix} p \\ q \end{bmatrix} + \mathbf{N} \frac{\partial}{\partial z} \begin{bmatrix} p \\ q \end{bmatrix} - \mathbf{D} \frac{\partial^2}{\partial z^2} \begin{bmatrix} p \\ q \end{bmatrix} + \mathbf{H} \begin{bmatrix} p \\ q \end{bmatrix} = \mathbf{f} \quad (2.42)$$

with

$$\mathbf{N} = \begin{bmatrix} 0 & C_0^{-1} \\ (2 - c_p) \frac{A}{\rho} - \delta_1 \frac{q^2}{A^2} C_0 & \delta_1 \frac{2q}{A} \end{bmatrix}, \quad \mathbf{D} = \begin{bmatrix} 0 & 0 \\ 0 & \frac{\eta}{\rho} \end{bmatrix}, \quad (2.43)$$

$$\mathbf{H} = \begin{bmatrix} 0 & 0 \\ 0 & c_q \frac{A}{\rho} R_0 + \frac{q}{A} \left(\frac{\partial \delta_1}{\partial z} - \frac{\delta_1}{A} \frac{\partial A}{\partial z} \right) \end{bmatrix}, \quad \mathbf{f} = \begin{bmatrix} -\Psi C_0^{-1} \\ Af_z \end{bmatrix} \quad (2.44)$$

and in terms of the original theory by Hughes and Lubliner (1973) (see Wan et al. (2002)):

Wan et al. (2002)	this study
$\delta_1 = 1 + \delta = \frac{2+n}{1+n}$	$\delta_1 = \frac{2 - 2\zeta_c(1 - \ln \zeta_c)}{(1 - \zeta_c)^2}$
$c_p = 1$	$c_p = 1 + \frac{1}{2}(1 - \zeta_c)$
$c_q = -\frac{N\rho}{R_0 A^2} = \frac{n+2}{4}$	$c_q = \frac{1}{2}(1 - \zeta_c)^{-1}$
with $N = -2(n+2)\pi\nu$	with $\zeta_c = \left(\frac{a_c}{a}\right)^2 \approx \left(1 - \frac{k}{\alpha}\right)^2$
where n is a free parameter	

(2.45)

Note that, in (2.42) for stability reasons, the term $(\eta/\rho)(\partial^2 q)/(\partial z^2)$ is kept, although it is small compared to the friction term $(2\pi\tau_w a)/\rho$.

2.2.6 Computational method

To analyze wave propagation using the approximate velocity profile function, a spectral element method is employed to solve the above sets of equations by discretisation of the spatial domain using sixth-order one-dimensional spectral elements. A Galerkin weighted residuals method is used to transform the set of partial differential equations into a spectral element

space. This transformation is presented in Appendix B. The time derivatives are treated using a second-order backward differencing scheme and at each time step $\Delta t = 0.001$ [s] a Newton-Raphson iterative scheme is deployed to handle the non-linear terms. This results in the following scheme:

$$\left[\frac{3}{2}\underline{M} + \Delta t \underline{S}_i^{n+1}\right] \mathbf{u}_{i+1}^{n+1} = 2\underline{M}\mathbf{u}^n - \frac{1}{2}\underline{M}\mathbf{u}^{n-1} + \Delta t \underline{M}\mathbf{f}_i^{n+1}, \quad (2.46)$$

where Δt is the time step used, $\mathbf{u} = [u_1 \ u_2]^T = [\underline{p} \ \underline{q}]^T$ and

$$\underline{S}_i^{n+1} = \underline{S}(\mathbf{u}_i^{n+1}), \quad \underline{S}_0^{n+1} = \underline{S}(\mathbf{u}^n), \quad \underline{S} = \underline{N} + \underline{D} + \underline{H}. \quad (2.47)$$

\underline{M} , \underline{N} , \underline{D} and \underline{H} are defined in (B.15). Furthermore,

$$\underline{f}_i^{n+1} = \underline{f}(\mathbf{u}_i^{n+1}), \quad \underline{f}_0^{n+1} = \underline{f}(\mathbf{u}^n), \quad (2.48)$$

where $\underline{f} = [f_1 \ f_2]^T$. The method yields reliable and stable solutions without the use of any kind of upwinding or stabilisation scheme. For a more detailed derivation of the final set of linear equations the reader is referred to Appendix B.

2.3 Results

2.3.1 Velocity profile function

Using $k = \sqrt{2}$ as defined in the previous section, the approximations made for parameters c_p and c_q as defined by equations (2.37) and (2.38), can be evaluated and compared to results found in the literature. Young and Tsai (1973b) gave an expression balancing the pressure gradient with the friction term and inertia forces, according to

$$\frac{\partial p}{\partial z} = -c_v \left(\frac{8\eta}{\pi a^4} \right) q - c_u \frac{\rho}{A} \frac{\partial q}{\partial t} \quad (2.49)$$

with coefficients c_v and c_u calculated from the exact solution as a function of the Womersley parameter α (Womersley (1957)). In this work, equation (2.39) was obtained to compare coefficients $c_q/(2 - c_p)$ and $1/(2 - c_p)$ to the values of c_v and c_u from Young & Tsai respectively in a physiological range of α . Their values, when using equations (2.37) and (2.38) with $k = \sqrt{2}$ are plotted as solid lines in figure 2.4. For large values of α coefficients $c_q/(2 - c_p)$ and $1/(2 - c_p)$ are in good agreement with the values for c_u and c_v from Young & Tsai and for low values of α ($\alpha < k$) the combination of our coefficients as well as c_v and c_u correspond to Poiseuille friction since in this range the pressure gradient and the flow are directly related. Owing to the assumptions made when using the approximate velocity profile function, the intermediate values of α show some differences with respect to Womersley's theory.

The same observation can be made when comparing the non-linear term $\gamma = \int v_z^2 dA$ derived from the approximate velocity profile function to γ derived from Womersley profiles. A single harmonic flow with radial frequency $\omega_q = 2\pi$ [s⁻¹] is prescribed and using values of the Womersley parameter in the range of $0 < \alpha \leq 16$ the corresponding pressure gradient $\partial p/\partial z$ is computed from Womersley's theory for flow in rigid tubes (Womersley (1957)). Using this combination of q and $\partial p/\partial z$ the velocity profiles and the integral of their square root (γ) for both theories can be determined as a function of α and time t . It can easily be shown that for all α , $\gamma(t)$ is a single harmonic signal with radial frequency $\omega_\gamma = 2\omega_q$. This harmonic signal is evaluated for both the approximate profiles (γ_{AP}) and the Womersley profiles (γ_{WP}) in the

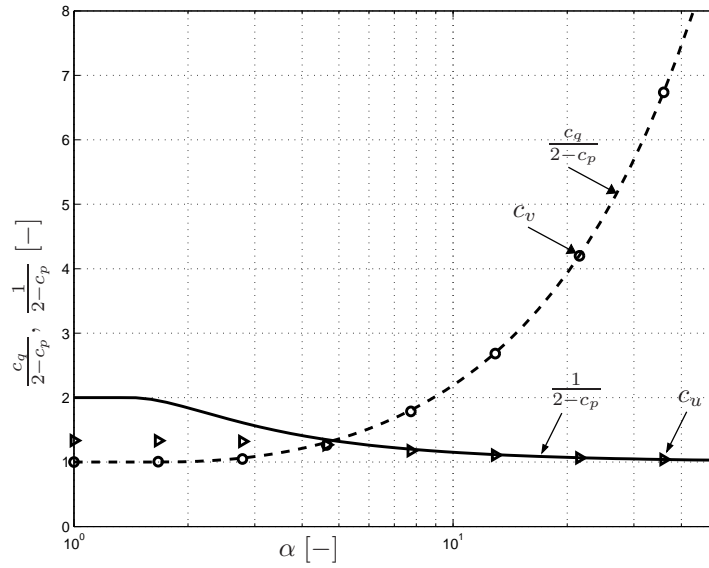


Figure 2.4: Coefficients $c_q/(2-c_p)$ and $1/(2-c_p)$ (dashed and solid lines respectively) as a function of α together with the values of c_v (\circ) and c_u (\triangleright) of Young & Tsai (1973).

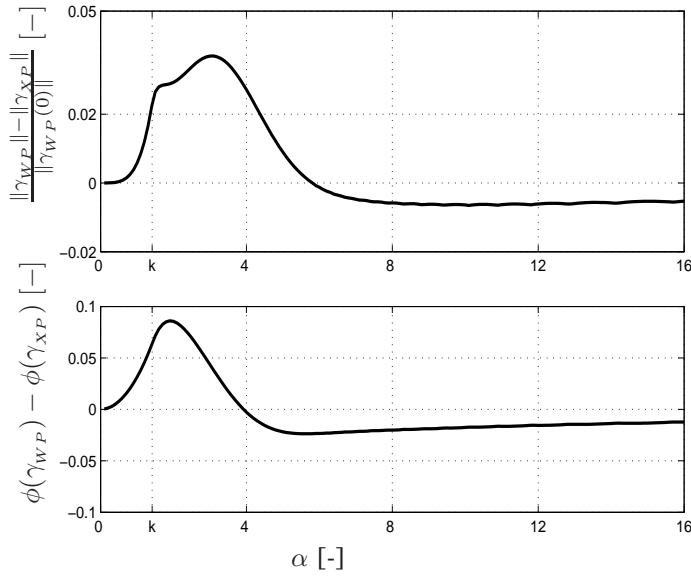


Figure 2.5: (Top) Absolute difference between $\|\gamma_{WP}\|$ and $\|\gamma_{AP}\|$, normalised by $\|\gamma_{WP}(\alpha \rightarrow 0)\|$ as a function of α . (Bottom) The phase difference between γ_{WP} and γ_{AP} as a function of α .

range of given α . Figure 2.5 shows the normalised (with $\gamma_{WP}(\alpha = 0)$) difference in the amplitude and the phase difference between both methods. Both the relative difference in amplitude and the phase difference approach 0 when α approaches 0. For large α , although more slowly, the differences also go to 0. Intermediate values of α show some differences in γ_{AP} and γ_{WP} as a result of the assumptions made when deriving the approximate velocity profile function. The behaviour of τ_w and γ as a function of time is illustrated, along with the corresponding velocity profiles, for $\alpha = 0, 2, 4, 8, 16$ and ∞ in the 6 panels of figure 2.6. Each panel represents a different Womersley number. The left-hand side of each panel shows the normalised flow and pressure gradient as function of the dimensionless time, followed (below) by the wall shear stress τ_w and non-linear term γ from both methods. The illustration on the right-hand side of each panel shows the velocity profiles for both theories at 8 equidistant time steps within one cycle. For low values of the Womersley parameter ($\alpha < \sqrt{2}$) the approximate velocity profile function exactly reproduces the expected Poiseuille profiles. For intermediate values of the Womersley parameter ($\alpha = 2, 4, 8, 16$) the profiles found using the approximate velocity profile method are more flat, however, an appropriate wall shear stress and convection parameter γ are found. Also, the phase shift between the pressure gradient and the wall shear stress as predicted by Womersley's theory is accurately described by the approximation. Note that in the case of a velocity profile proportional only to the flow, as in Hughes and Lubliner (1973) and Olufsen (1999), the wall shear stress would be in phase with the flow also. At higher values of the Womersley parameter ($\alpha \rightarrow \infty$) profiles are flat and well-predicted, resulting in good approximations for the wall shear stress and γ .

To demonstrate the possibility of determining τ_w and γ when imposing a physiological flow signal, multi-harmonic flow pulses from a coronary artery and the aorta (based on the first 10 harmonics of this signal) are used as an input for the previous computations. Figure 2.7 shows the result with $\alpha = 2$ for the left coronary artery and $\alpha = 12$ for the aorta. Although the estimates of α (and so δ_s) are based on the first harmonic of the flow signal, good approximations for the velocity profiles are obtained. The wall shear stress and the convection term resulting from the approximate velocity profiles also show good correspondence with Womersley's theory when imposing a multi-harmonic flow signal.

2.3.2 Wave propagation

The theory introduced in this study has already shown improvements over other assumed velocity profiles in approximating the wall shear stress and the convection term obtained by Womersley's theory. Whereas the new convection term yields only small changes in the one-dimensional equation (δ_2 and δ_3 are small with respect to δ_1), the expression for the friction term is significantly altered when compared to the friction term when assuming a Poiseuille profile. To determine whether the improved friction term influences the modelling of the waves travelling through the arterial system, a comparison in a physiological range is made between the friction term as defined by the velocity profile function and the friction defined by a Poiseuille profile (Hughes and Lubliner (1973)). Using data from Olufsen and Peskin (2000), two compliant tubes are modelled both using six (sixth-order) spectral elements. One is an aorta-like vessel and the other is based on the femoral artery (FA) to include inertia-dominated flow ($\alpha \approx 12$) as well as flow where friction is more important ($\alpha \approx 4$). The geometric data (the radius a and the wall thickness h) of these vessels are given in table 2.3.2.

Note that in our situation the aorta is modelled using less tapering than in Olufsen and Peskin (2000) because in this work no side branches are modelled to subtract fluid from the vessel. The wall behaviour is assumed to be linear elastic according to (2.41) and the corresponding Young's modulus ($E = 4.0 \cdot 10^5$ [N/m]) and Poisson's ratio ($\nu = 0.3$ [-]) for both vessels are

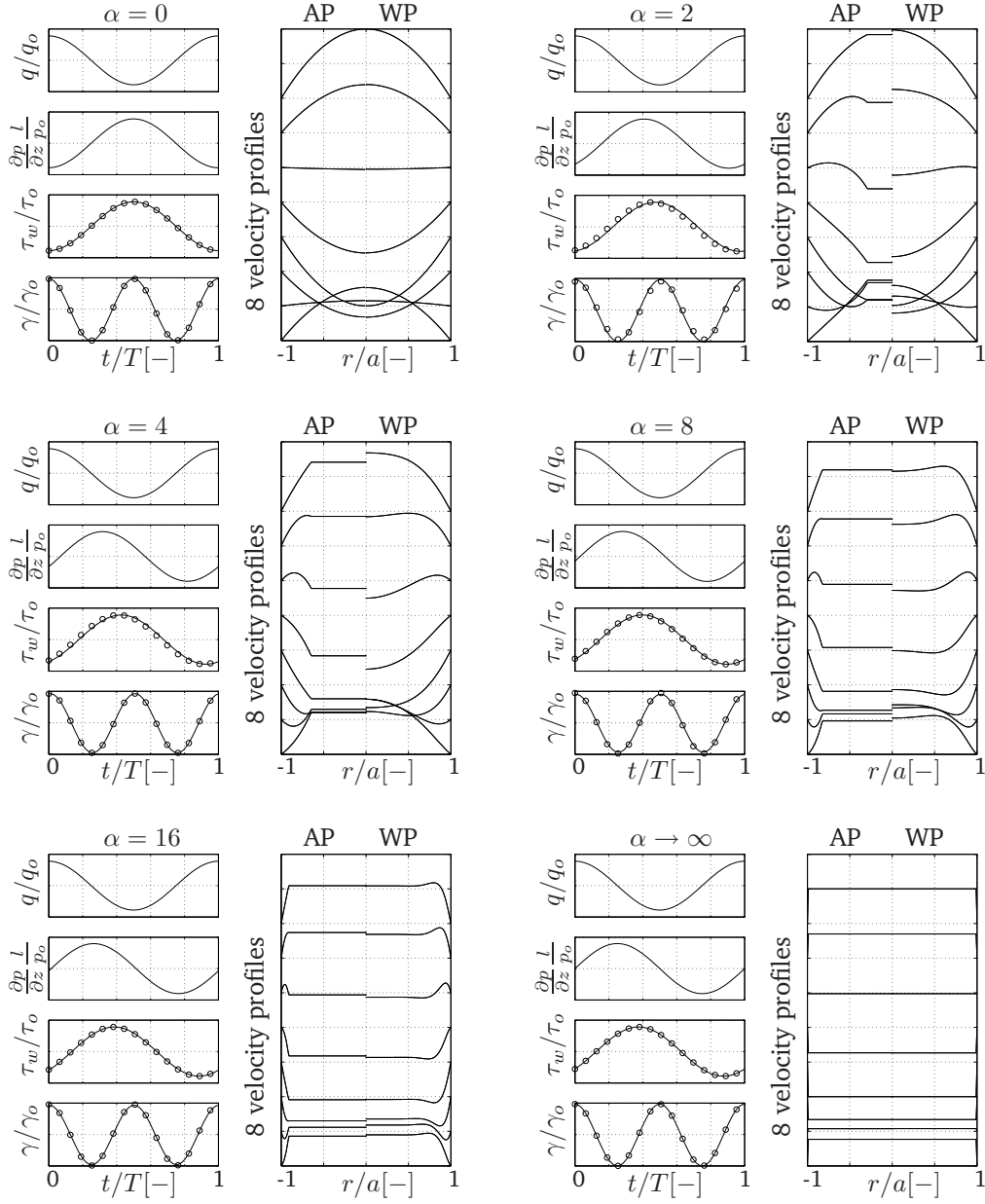


Figure 2.6: Each of the 6 panels represents velocity profiles $v_z(r, t)$ at 8 equidistant time steps (right) for both our approximation (AP) and Womersley theory (WP) as a result of single-harmonic flow pulse q and pressure gradient $\partial p/\partial z$ (left-top) for $\alpha = 0, 2, 4, 8, 16,$ and ∞ . Resulting wall shear stress $\tau_w(t)$ and convection parameter $\gamma(t)$ from the approximate velocity profile function (o) and Womersley theory (–) are depicted in the left-bottom 2 plots.

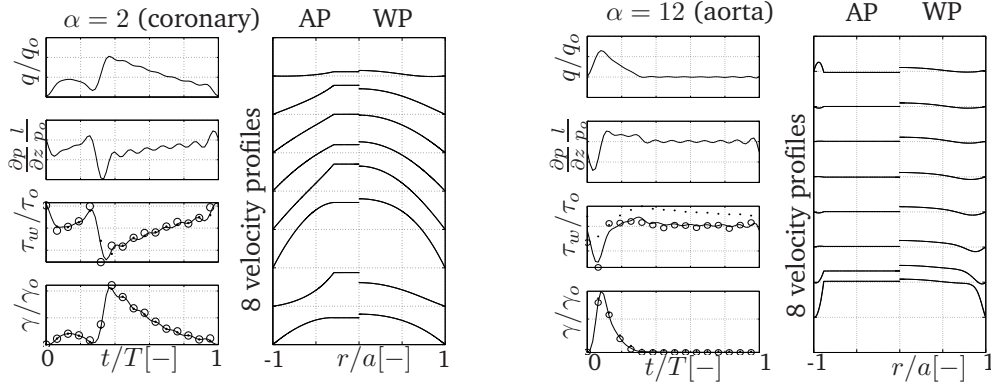


Figure 2.7: both panels represents velocity profiles $v_z(r, t)$ at 8 equidistant time steps (right) for both our approximation (AP) and Womersley theory (WP) as a result of multi-harmonic physiological flow pulse q and pressure gradient $\partial p/\partial z$ (left-top) obtained from the left coronary artery (left panel) and the aorta (right panel). Resulting wall shear stress $\tau_w(t)$ and convection parameter $\gamma(t)$ from Womersley theory (—) and the approximate velocity profile function (o) are depicted in the left-bottom 2 plots.

Vessel type	Length L [mm]	local radius a_0 [mm]	wall thickness h/a_0 [—]	wave speed c_0 [m/s]
Aorta	400	12.5 - 9.0	0.125	5.1
FA	400	4.3 - 3.4	0.3	8.0

Table 2.1: Data of vessels used in numerical experiments.

Vessel type	R_1 [Ns/m ⁵]	R_2 [Ns/m ⁵]	C_T [m ⁵ /N]
Aorta	$2.31 \cdot 10^7$	$7.69 \cdot 10^7$	$1.95 \cdot 10^{-8}$
FA	$2.05 \cdot 10^8$	$1.21 \cdot 10^9$	$1.20 \cdot 10^{-9}$

Table 2.2: Windkessel parameters used in numerical experiments.

obtained from Westerhof et al. (1969). Blood properties are set at $\eta = 4.5 \cdot 10^{-3}$ [kg/m·s] and $\rho = 1.04 \cdot 10^3$ [kg/m³] for the viscosity and the density respectively, according to Porenta et al. (1986). From the above data the constant wave speed c_0 for the two vessels, as given in table 2.3.2, is found using $c_0 = \sqrt{A_0/\rho C_0}$, where A_0 and C_0 are the cross-sectional area and the compliance at the initial pressure p_0 respectively. At the inlet of the aortic and the femoral tube flow pulses $q(z = 0, t)$ as measured by Olufsen and Peskin (2000) are prescribed as depicted in figure 2.8 and 2.9 respectively, whereas at the distal end of the vessels a three-element Windkessel is defined to relate the outlet pressure to the outlet flow (Stergiopoulos et al. (1999)). Parameters R_1 , R_2 and C_T are the corresponding terminal resistance, peripheral resistance and compliance respectively, as defined in table 2.3.2. The values of R_1 were obtained by modelling minimal reflections at the outlets according to

$$R_1 \sim Z_0 = \sqrt{\frac{L_0}{C_0}} = \sqrt{\frac{\rho h E}{2\pi^2(1-\nu^2)a_0^5}} \quad (2.50)$$

with $L_0 = \rho/A_0$ representing the local inertance, C_0 the local compliance as defined by (2.41) and Z_0 the local impedance at the distal end of the vessel. To obtain pressures in the physiological range, R_2 was derived using the total resistance R_T as

$$R_T = R_1 + R_2 = \bar{p}/\bar{q} \quad \text{and} \quad C_T = \tau/R_2, \quad (2.51)$$

with $\bar{p} = 10$ [kPa] the desired mean pressure and \bar{q} the mean flow prescribed at the inlet. By first-order approximation, the time constant $\tau = 1.5$ s was found to result in a physiological pressure drop in the pressure signal comparable to that demonstrated in the data of Olufsen and Peskin (2000)). Note that, similar to the literature, in Poiseuille-friction computations the friction term was altered by replacing the second equation of (2.33) by

$$\tau_w^p = -\frac{a}{2}R_0q = -\frac{4\eta}{\pi a^3}q \quad (2.52)$$

and thus changing only the second term on the right-hand side of the momentum equation in (2.32). The volumetric outflow per unit of length was set to $\Psi = 0$ [m²/s]. Since friction is dependent, as well as on flow q , on the pressure gradient $\partial p/\partial z$ and because we are also interested in the wall shear stress τ_w , these two quantities are depicted along with the flow q as a function of time at four equidistant positions in the aorta-like and femoral-like vessel (figures 2.8 and 2.9 respectively). Results are captured in the 9th to 10th period when time-periodic pressure and flow was found. All quantities are normalised by dividing them by the mean (over time) of the Poiseuille friction as defined by (2.52). In the aorta-like vessel the two different velocity profiles yield very distinctive wall shear stresses. Friction as approximated by the Poiseuille profile shows the expected in-phase behaviour with the flow and is much smaller than the friction according to the approximate velocity profile function. Looking at the resulting pressure gradient and flow waves in the aorta, however, the effect of the friction approximation used appears negligible, as expected from inertia-dominated flow. In the femoral artery the wall shear stress based on the approximate velocity profile function is of the same order of magnitude as friction approximated by assuming a Poiseuille profile. As a result of the in-phase behaviour of the Poiseuille wall shear stress with the flow, however, it is different from the wall shear stress calculated here, which is dependent on pressure gradient as well as flow. Since in medium-sized and smaller arteries friction influences the wave propagation, this also results in differences in the pressure gradient. Hence, a suitable friction model is crucial in predicting the pressure and the flow waves propagating through the arterial system, especially for the medium-sized arteries where Poiseuille friction is not appropriate. The reason why the flow is

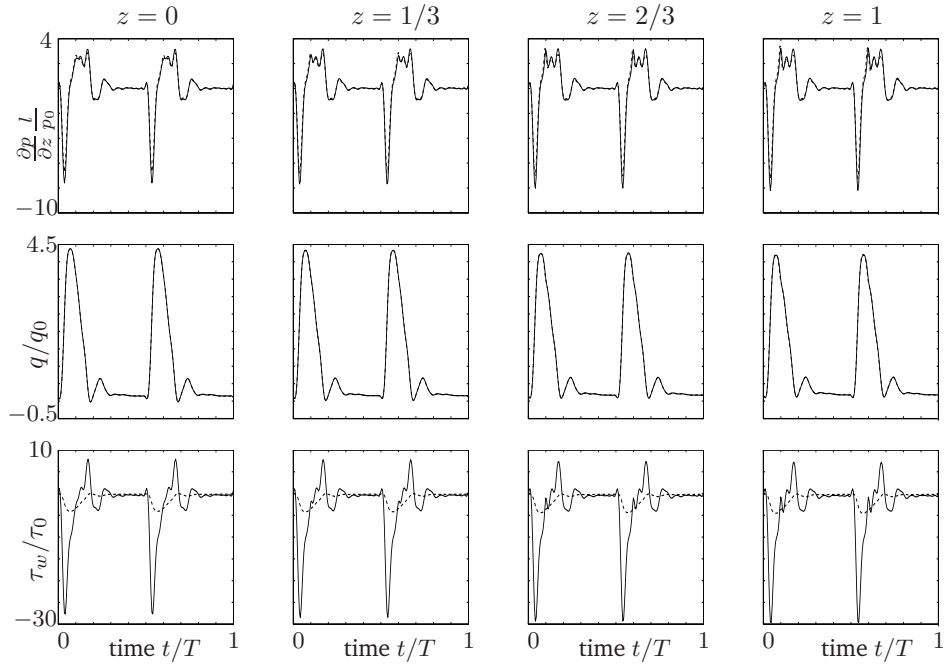


Figure 2.8: Analysis of the friction term in an aorta-like vessel, showing normalised pressure gradient $\partial p/\partial z$ (top), flow q (middle) and wall shear stress τ_w (bottom) as a function of time at four equidistant positions in the modelled vessel. Solid lines show results using our approximate velocity profile function whereas dashed lines show results using Poiseuille friction.

not influenced by the friction term used can be explained by the fact that the flow pulse, as depicted at $z = 0$, is prescribed as an essential boundary condition.

2.4 Discussion

The theory proposed in this chapter uses the division of fluid inside a vessel lumen into a viscous layer close to the wall connected to an inviscid core to obtain first-order approximations for the friction forces and the non-linear term in one-dimensional wave propagation in the time domain. The local thickness of the viscous layer is determined as a function of the Womersley parameter α , where the definition of α is based on the first harmonic of the flow signal. The method proposed here yields wall shear stresses and convection forces in good agreement with Womersley's theory for time-dependent flow in rigid tubes when a single-harmonic flow pulse is imposed. In the limiting cases ($\alpha = 0$ and $\alpha \rightarrow \infty$) Womersley's theory is exactly reproduced by the approximation proposed in this study. For intermediate values of α , both the wall shear stresses and the convection forces show good agreement with Womersley's theory where the velocity profiles obtained show the expected phase difference between the flow in the Stokes layer and the core flow. When comparing velocity profiles, the wall shear stress and the non-linear term based on the approximate velocity profile function with Womersley's solutions, using a more physiological flow pulse based on measurements in the aorta and coronary artery, results

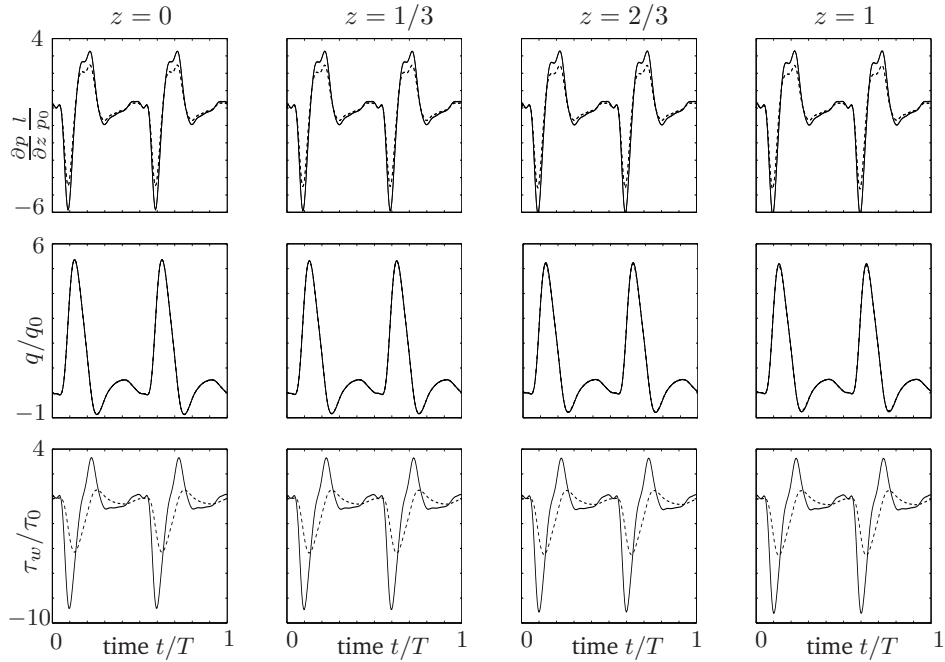


Figure 2.9: As figure 2.8 but for a femoral-like vessel.

similar to Womersley's theory are obtained. So, even though the estimation of the Womersley parameter α is based on only the first harmonic of the flow signal, good approximations for the thickness of the viscous layer for a multi-harmonic flow signal are still obtained, provided the first harmonic is dominant over the higher frequencies involved and not negligibly small compared to the mean level. Since the estimation of the thickness of the Stokes layer was derived for straight vessels with gradual changes in the cross-section area, more sophisticated analysis will be needed to model geometric discontinuities like stenoses and bifurcations. Theories from Schlichting (1960) and Pedley (1980) as well as three-dimensional computational fluid dynamics results and experimental data could be used to derive estimates for the thickness of the Stokes layer in these regions.

The effect of the wall shear stress derived from the velocity profile approximation in one-dimensional wave propagation was examined by comparing its results to the one-dimensional theory based on Poiseuille friction in an aorta-like and a femoral-like tapered vessel. From these simulations the conclusion could be drawn that in large, inertia-dominated vessels friction is largely over-estimated by assuming Poiseuille profiles, although the influence of an appropriate friction model on the wave propagation phenomena is insignificant. In smaller vessels, however, the choice of an appropriate friction model is important for obtaining reliable wall shear stresses as well as physiological pressure and flow wave propagation characteristics. This implies that using an explicit method to determine the wall shear stress, i.e. no proper friction approximation in the one-dimensional wave propagation equations, will not yield reliable results.

The spectral element framework used for discretisation enables simple connection of tubes by adding continuity of pressure and flow in bifurcations. This, together with appropriate proximal and distal boundary conditions may lead to the modelling of the total arterial tree, where

further improvements may be obtained by introducing an appropriate model to predict the local blood viscosity.

In this work, a constant fluid viscosity was assumed whereas it is known that blood viscosity is dependent on the local shear rate through, for example, the aggregation of erythrocytes present in the plasma. Such behaviour may change local velocity profiles resulting in different wall shear stresses. Furthermore, a viscoelasticity model may be incorporated to model the arterial wall behaviour, giving the model more physiological characteristics. This may be achieved by, instead of substituting the constitutive equation into the mass balance, explicitly defining a differential equation describing the wall behaviour (e.g. the standard linear-solid model) and building a system of equations with three variables (A, q, p) instead of two (p, q) .

Proper evaluation of the model proposed, apart from a comparison to Womersley's theory, could be accomplished by coupling the one-dimensional solutions to a three-dimensional fluid-structure interaction (FSI) model and comparing the predicted wall shear stresses of both theories, or by a comparison of the pressure and flow wave propagation to data sets obtained from experiments.

The model proposed may be used to simulate pressure and flow wave propagation in the time domain to determine the effect of a local arterial pathology on the total arterial system. Bypass surgery alternatives may be evaluated and, combining the pressure and wall shear stress data obtained from this work with a suitable adaptation law for the arterial wall, remodelling of the total arterial system may be studied. As the centre-line velocity, corresponding to v_c in the model proposed, can be assessed in-vivo by ultrasound systems (Brands et al. (1996)), this model can also serve as a first-order method to derive the wall shear stress from ultra-sound measurements as an alternative to extrapolation of velocity profiles.

2.5 Conclusion

A wave propagation model in the time domain is developed where assumptions concerning the velocity profiles are based on a newly developed velocity profile function, dependent not only on the main velocity, but also on the pressure gradient. Using this method, a phase difference between the wall shear stress and the mean velocity similar to that found in physiological situations and by Womersley's theory in the frequency domain is obtained. Also, the approximation of the non-linear term based on the approximate velocity profile function shows good agreement with Womersley's theory. Implications of the friction term for one-dimensional wave propagation characteristics are illustrated and shown to be significant.

Chapter 3

A time-domain based wave propagation model of blood flow in viscoelastic vessels

The contents of this chapter have been submitted for publication: D. Bessems, C.G. Giannopapa, M.C.M. Rutten and F.N. van de Vosse, *Experimental validation of a time-domain-based wave propagation model of blood flow in viscoelastic vessels*, J. Biomech.

3.1 Introduction

Wave propagation models of blood flow in the arterial system have been subject of many studies throughout the last century. From apparently the first author to publish the results on wave propagation in distensible tubes (Witzig (1914)) until the early seventies these models were mainly based on analytical solutions of the equations of axisymmetric motion of viscous, incompressible fluid in cylindrical coordinates in the frequency domain. An overview of these methods is presented by Cox (1968), showing several models describing the propagation of pressure and flow waves through elastic and viscoelastic tubes. The most prominent shortcoming of these methods is their lack of describing the non-linear fluid behaviour that has shown to be crucial in the alternation of the pressure pulse shape while propagating through the larger or tapered arteries (Anliker et al. (1968)). From 1970 onwards, with the introduction of faster digital computers, space-time numerical methods became increasingly important in describing blood flow in the arterial system. Descriptions from Hughes and Lubliner (1973) and Anliker et al. (1971) showed that one-dimensional wave propagation models in the time domain are well capable of describing the non-linear behaviour of the convection forces in blood flow through larger elastic vessels.

The mechanical behaviour of the arterial wall is usually modelled as purely elastic. While examining the blood flow in the aorta, this assumption may well hold. In the smaller arteries, however, the composition of the arterial wall results in a non-linear and viscoelastic response to cyclic pressure loads that yields the typical hysteresis and attenuation in wave propagation (Learoyd and Taylor (1966)). With respect to the non-linear behaviour, an incremental effective Young modulus $E(z, p)$ depending on the pressure can be used to obtain a first-order appropriate model from linear theory. With respect to the viscoelastic behaviour of arteries, the viscous contribution varies between the 10 and 60%, depending on the mechanical properties of the artery that vary with the distance of the artery to the heart (Learoyd and Taylor (1966)). Since current one-dimensional time-domain-based wave propagation models of blood flow in the arterial system consider the arterial wall to be purely elastic, the importance of its viscoelastic characteristics on the attenuation of pressure and flow waves is neglected.

In this chapter, a constitutive law describing a linear viscoelastic relation between the local pressure and the cross-sectional area, suitable for implementation in time domain based wave propagation models, is proposed. This law is based on the standard linear-solid model, or Kelvin body (Fung (1993)), and was also used by Cox (1968) in the frequency domain. In section 3.2.1 the differential equation governing this model will be solved along with the conservation of mass and the momentum balance from chapter 2 describing one-dimensional wave propagation.

To validate the model, the pressure and flow obtained from the numerical simulations are compared to their measured counterpart, as obtained from Giannopapa (2004). The setup used in this work is described in section 3.2.3 and in section 3.3 the results are presented. In section 3.4, the methods used and the results obtained are discussed.

3.2 Methods

3.2.1 Numerical methods

The derivation of the governing equations for one-dimensional wave propagation of incompressible fluids in distensible tubes was taken from Hughes and Lubliner (1973). A proper velocity profile function that provides approximations for the frictional forces and non-linear

term present in these equations is presented in chapter 2, where the final set of equations defined in terms of the cross-sectional area A , flow q and pressure p is derived as

$$\left. \begin{aligned} \frac{\partial A}{\partial t} + \frac{\partial q}{\partial z} &= 0 \\ \frac{\partial q}{\partial t} + \frac{\partial}{\partial z} \left(\delta_1 \frac{q^2}{A} \right) + \frac{A}{\rho} \frac{\partial p}{\partial z} &= Af_z + \frac{2\pi a}{\rho} \tau_w + \frac{\eta}{\rho} \frac{\partial^2 q}{\partial z^2} \\ p(z, t) &= \tilde{p}(A(z, t); z, t). \end{aligned} \right\} \quad (3.1)$$

The first equation of (3.1) describes conservation of mass with t the time and z the axial coordinate. The second equation represents the momentum balance where η and ρ are the fluid viscosity and density respectively, f_z is a body force acting on the fluid in axial direction and a is the local lumen radius. Following chapter 2, the wall shear stress τ_w is given by

$$\tau_w = -\frac{2\eta}{(1-\zeta_c)a} \frac{q}{A} + \frac{a}{4}(1-\zeta_c) \frac{\partial p}{\partial z} \quad (3.2)$$

with $\zeta_c = (\max[0, (1 - \sqrt{2}/\alpha)])^2$ where α is the Womersley parameter. The parameter δ_1 in equation (3.1) can be derived as

$$\delta_1 = \frac{2 - 2\zeta_c(1 - \ln \zeta_c)}{(1 - \zeta_c)^2}. \quad (3.3)$$

The third equation in (3.1) represents the constitutive law relating the local instantaneous pressure to the local instantaneous cross-sectional area. In chapter 2 a linear elastic material law based on thin walled cylinder theory is proposed, resulting in

$$\frac{\partial A}{\partial t} = C_0 \frac{\partial p}{\partial t} \quad \text{with} \quad C_0 = \frac{2\pi(1-\mu^2)a_0^3}{hE}, \quad (3.4)$$

with C_0 the compliance per unit of length of the vessel and h its local wall thickness. The parameters μ and E are Poisson's ratio and Young's modulus of the wall material respectively. Subscript $_0$ indicates the reference state at the initial pressure $p = p_0$. In this approach, the constitutive relation can be directly substituted into the conservation of mass equation resulting in a (p, q) -system with only 2 equations. Since the assumption of linear elastic behaviour ignores the viscoelastic properties of the arterial wall, in the next section a more physiological wall model including viscoelasticity will be introduced.

3.2.2 Solid model

Neglecting the inertia and body forces, the momentum equation for a solid material in the time-space domain reads:

$$\nabla \cdot \boldsymbol{\sigma} = \mathbf{0}, \quad (3.5)$$

with $\boldsymbol{\sigma}$ the Cauchy stress tensor. In cylindrical coordinates (see figure 3.1), because of geometrical and constitutive symmetry, the only non-trivial component of the momentum equations is:

$$\frac{\partial \sigma_{rr}}{\partial r} + \frac{\sigma_{rr} - \sigma_{\theta\theta}}{r} = 0. \quad (3.6)$$

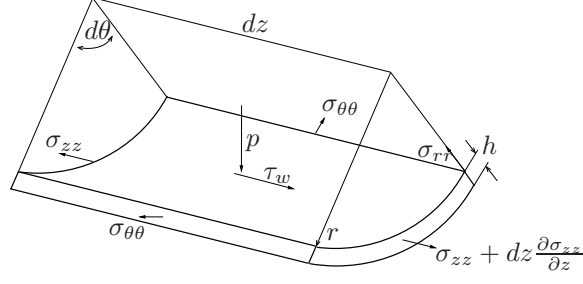


Figure 3.1: Infinitesimal arterial wall volume showing the forces acting on it.

From this equation and boundary condition $\sigma_{rr}|_{r=a+h} = 0$ on the outer surface of the tube, the radial Cauchy stress σ_{rr} is:

$$\sigma_{rr}(\xi) = \int_{\xi}^{a+h} \frac{\sigma_{rr} - \sigma_{\theta\theta}}{r} dr, \quad a \leq \xi \leq a+h. \quad (3.7)$$

The internal pressure $p = -\sigma_{rr}|_{r=a}$ is then defined as:

$$p = \int_a^{a+h} \frac{\sigma_{\theta\theta} - \sigma_{rr}}{r} dr \quad (3.8)$$

Since for thin walled cylindrical tubes ($h \ll a$) the radial stresses are negligibly small ($\sigma_{rr} \ll \sigma_{\theta\theta}$), this leads to an internal pressure p equal to

$$p - p_e \approx \frac{h}{a} \sigma_{\theta\theta} \quad (3.9)$$

with h the wall thickness, a the radius of the deformed tube and p_e the external pressure. In addition, the momentum balance in axial direction of a thin walled tube undergoing small deformations is given by

$$\epsilon_{zz} = \frac{\partial u_z}{\partial z} = \frac{1}{E} (\sigma_{zz} - \mu \sigma_{\theta\theta} - \mu \sigma_{rr}) \quad (3.10)$$

with μ the Poisson ratio, E Young's modulus and u_z the wall displacement in axial direction. Here we assume linear elastic behaviour in axial direction. Since this axial displacement of the vessel is assumed to be constrained by surrounding organs ($\epsilon_{zz} = 0$) and again $\sigma_{rr} \ll \sigma_{\theta\theta}$, the axial stress equals

$$\sigma_{zz} = \mu \sigma_{\theta\theta}. \quad (3.11)$$

To relate the circumferential stress $\sigma_{\theta\theta}$ to the circumferential strain $\epsilon_{\theta\theta}$ a three parameter description based on the Kelvin model as depicted in figure 3.2 is used. Both springs are assumed to behave linearly elastic and the dashpot provides a linear relation between the stress and strain rate, so

$$\sigma_e = \frac{E_e}{(1-\mu^2)} \epsilon \quad \text{and} \quad \sigma_v = \frac{E_v}{(1-\mu^2)} \epsilon_e = \eta_w \dot{\epsilon}_v. \quad (3.12)$$

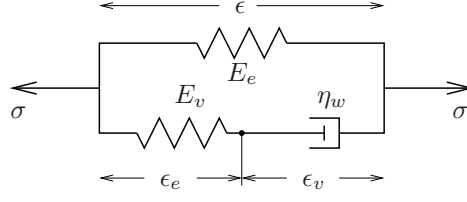


Figure 3.2: Standard linear-solid model representing an elastic part and a viscous part with Young's moduli E_e and E_v respectively. The dashpot has a constant coefficient of viscosity η_w . The stress σ and the strain ϵ are related through relation (3.13).

Here, E_e and E_v are Young's moduli of the springs of the elastic and viscous part of the model respectively and η_w is the dashpot's coefficient of viscosity. The strains ϵ , ϵ_e and ϵ_v are the strains of the individual components of the Kelvin body as shown in figure 3.2. The corresponding differential equation relating the total strain ϵ to the total stress $\sigma = \sigma_e + \sigma_v$ reads (Fung (1993))

$$\sigma + \frac{\eta_w}{E_v} \dot{\sigma} = \frac{E_e}{1 - \mu^2} \epsilon + \frac{\eta_w}{1 - \mu^2} \left(1 + \frac{E_e}{E_v}\right) \dot{\epsilon} \quad (3.13)$$

Positioning this model in circumferential direction of a vessel according to figure 3.1 (so $\sigma = \sigma_{\theta\theta}$ and $\epsilon = \epsilon_{\theta\theta}$), and introducing the relaxation time for constant strain τ_ϵ and the relaxation time for constant stress τ_σ according to

$$\tau_\epsilon = \frac{\eta_w}{E_v} \quad \text{and} \quad \tau_\sigma = \frac{\eta_w}{E_e} \left(1 + \frac{E_e}{E_v}\right) \quad (3.14)$$

respectively, yields

$$\sigma_{\theta\theta} + \tau_\epsilon \dot{\sigma}_{\theta\theta} = \frac{E_e}{1 - \mu^2} (\epsilon_{\theta\theta} + \tau_\sigma \dot{\epsilon}_{\theta\theta}). \quad (3.15)$$

For the remainder of this chapter, subscripts $\theta\theta$ will be omitted. Using (3.9) and $\epsilon_{\theta\theta} = (a - a_0)/a_0 \approx (A - A_0)/2A_0$, (3.13) can be expressed in terms of p and A . This gives the final set of equations as

$$\left. \begin{aligned} \frac{\partial A}{\partial t} + \frac{\partial q}{\partial z} &= 0 \\ \frac{\partial q}{\partial t} + \frac{\partial}{\partial z} \left(\delta_1 \frac{q^2}{A} \right) + \frac{A}{\rho} \frac{\partial p}{\partial z} &= Af_z + \frac{2\pi a}{\rho} \tau_w + \frac{\eta}{\rho} \frac{\partial^2 q}{\partial z^2} \\ \frac{a}{h} p + \tau_\epsilon \frac{\partial}{\partial t} \left(\frac{a}{h} p \right) &= \frac{E_e}{1 - \mu^2} \left(\frac{A - A_0}{2A_0} + \frac{\tau_\sigma}{2A_0} \frac{\partial A}{\partial t} \right) \end{aligned} \right\} \quad (3.16)$$

In an (A, q, p) -formulation this yields the following general set of equations:

$$\mathbf{M} \frac{\partial}{\partial t} \begin{bmatrix} A \\ q \\ p \end{bmatrix} + \mathbf{N} \frac{\partial}{\partial z} \begin{bmatrix} A \\ q \\ p \end{bmatrix} - \mathbf{D} \frac{\partial^2}{\partial z^2} \begin{bmatrix} A \\ q \\ p \end{bmatrix} + \mathbf{H} \begin{bmatrix} A \\ q \\ p \end{bmatrix} = \mathbf{f} \quad (3.17)$$

with

$$\begin{aligned}
\mathbf{M} &= \begin{bmatrix} 1 & 0 & 0 \\ 0 & 1 & 0 \\ -\frac{\tau_\sigma}{2A_0} & 0 & \tau_\epsilon \frac{a}{h} \end{bmatrix}, \quad \mathbf{N} = \begin{bmatrix} 0 & 1 & 0 \\ -\delta_1 \frac{q^2}{A^2} & \delta_1 \frac{2q}{A} & \frac{A}{2\rho}(1 + \zeta_c) \\ 0 & 0 & 0 \end{bmatrix}, \\
\mathbf{H} &= \begin{bmatrix} 0 & 0 & 0 \\ -f_z & \frac{A}{\rho(1 - \zeta_c)} R + \frac{q}{A} \frac{\partial \delta_1}{\partial z} & 0 \\ -\frac{E_e}{2A_0} & 0 & \frac{1}{h} \left(a + \tau_\epsilon \frac{\partial a}{\partial t} - \frac{a}{h} \frac{\partial h}{\partial t} \right) \end{bmatrix}, \\
\mathbf{D} &= \begin{bmatrix} 0 & 0 & 0 \\ 0 & \frac{\eta}{\rho} & 0 \\ 0 & 0 & 0 \end{bmatrix}, \quad \mathbf{f} = \begin{bmatrix} 0 \\ 0 \\ -\frac{1}{2} E_e \end{bmatrix}.
\end{aligned} \tag{3.18}$$

The linearisation of this set of equations is presented in Appendix C. To solve it, a spectral element method is employed by discretisation of the spatial domain using sixth-order one-dimensional spectral elements. A Galerkin weighted residuals method is used to transform the set of partial differential equations into a spectral element space. The time derivatives are treated using a second-order backward differencing scheme and at each time step Δt a Newton-Raphson iterative scheme is applied to handle the non-linear terms. This results in the following scheme:

$$\left[\frac{3}{2} \underline{\mathbf{M}} + \Delta t \underline{\mathbf{S}}_i^{n+1} \right] \mathbf{u}_{i+1}^{n+1} = 2 \underline{\mathbf{M}} \mathbf{u}^n - \frac{1}{2} \underline{\mathbf{M}} \mathbf{u}^{n-1} + \Delta t \underline{\mathbf{M}} \mathbf{f}_i^{n+1}, \tag{3.19}$$

where $\mathbf{u} = [u_1 \ u_2 \ u_3]^T = [A \ q \ p]^T$ and

$$\underline{\mathbf{S}}_i^{n+1} = \underline{\mathbf{S}}(\mathbf{u}_i^{n+1}), \quad \underline{\mathbf{S}}_0^{n+1} = \underline{\mathbf{S}}(\mathbf{u}^n), \quad \underline{\mathbf{S}} = \underline{\mathbf{N}} + \underline{\mathbf{D}} + \underline{\mathbf{H}}. \tag{3.20}$$

The matrices $\underline{\mathbf{M}}$, $\underline{\mathbf{N}}$, $\underline{\mathbf{D}}$ and $\underline{\mathbf{H}}$ are the discretised versions of \mathbf{N} , \mathbf{D} , \mathbf{H} and \mathbf{f} respectively from (3.18). Furthermore,

$$\mathbf{f}_i^{n+1} = \mathbf{f}(\mathbf{u}_i^{n+1}), \quad \mathbf{f}_0^{n+1} = \mathbf{f}(\mathbf{u}^n), \tag{3.21}$$

where $\mathbf{f} = [f_1 \ f_2 \ f_3]^T$. Essential boundary conditions are prescribed by imposing $u_j(z, t) = u_{j,in}(t)$ at Γ_{in} and $u_j(z, t) = u_{j,out}(t)$ at Γ_{out} where u_j represents either the flow ($j = 2$) or the pressure ($j = 3$). $\mathbf{u}^0(z, t = 0) = [u_1^0(z), u_2^0(z), u_3^0(z)]$ is used as an initial condition over the total spatial domain. The method yields reliable and stable solutions without the use of any kind of upwinding or other stabilisation method.

3.2.3 Experimental setup

To validate the computational model described in the previous section, a comparison is made between the pressure and the flow as obtained from the numerical model and the pressure and flow from the experimental setup of Giannopapa (2004). This experimental setup is depicted in figure 3.3. The device consists of a polyurethane vessel marked as D constrained in horizontal position inside an open water filled container C . The water column above the tube prescribes the pressure outside the vessel, which is assumed constant over the height of the vessel. The vessel was pre-strained axially to 3% to keep it straight after being pressurised. One end of the

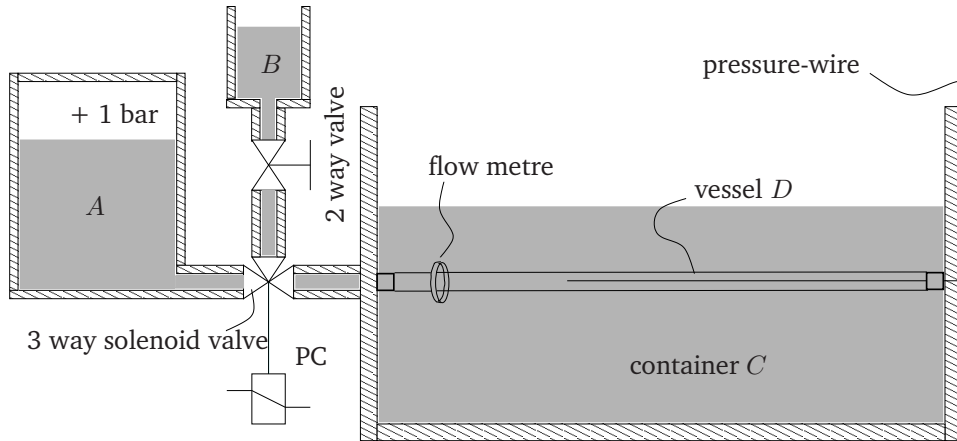


Figure 3.3: Schematic representation of the experimental setup filled with water. *A*: closed container at constant pressure. *B*: open container. *C*: open container. *D*: polyurethane tube. The three-way solenoid valve is operated by a PC and the two-way valve is manually operated. The pressure and the flow are measured using a flow metre and a pressure wire.

tube is connected to a three-way solenoid valve controlled by a PC and the other end is closed. The three-way valve connects to either the closed tank *A* or via a two-way manually operated valve to the open tank *B*. Closed tank *A* is constantly pressurised at 100 [kPa]. When the solenoid valve is not engaged, the water column inside tank *B* imposes the (initial) pressure inside the polyurethane tube. By engaging the solenoid valve, it opens for a short period of time (50 [ms]) and generates a pressure pulse that will travel up and down the polyurethane vessel. According to Giannopapa (2004), the duration of the opening of the valve was chosen to be as short as possible because the wavelength of the waves should be small enough to distinguish between forward and backward travelling waves. The flow through the vessel is measured with a perivascular flow sensor (type MC28AX, Transonic, the Netherlands). A pressure sensor inside the vessel (pressurewireXT, Radi Medical Systems, Uppsala, Sweden) is used to simultaneously measure the pressure.

Two polyurethane vessels (from HemoLab, www.hemolab.nl) with lumen radius and wall thickness as shown in figure 3.4 were used. Vessel S (serie PUt25.450) is a straight vessel with constant wall thickness and vessel T (serie PUt25.450.t) is tapered with a varying wall thickness to obtain a constant wave velocity similar to the wave speed of vessel S. This pulse-wave velocity, based on the Moens-Korteweg definition

$$c_0 = \sqrt{\frac{E h}{2\rho(1 - \mu^2)a}} \quad (3.22)$$

was estimated to be $c_0 \approx 8$ [m/s] when assuming an effective Young modulus of $E_e \approx 13$ [MPa]. The way the parameters E_e , E_v and η_w used in the computational model were determined will be described in the next section.

The vessels used by Giannopapa (2004) were pre-loaded by container *B* at 3 [kPa] relative to the pressure outside the vessels and before each measurement the pressure wires were calibrated to zero. During measurements the two-way valve was closed to preserve the volume

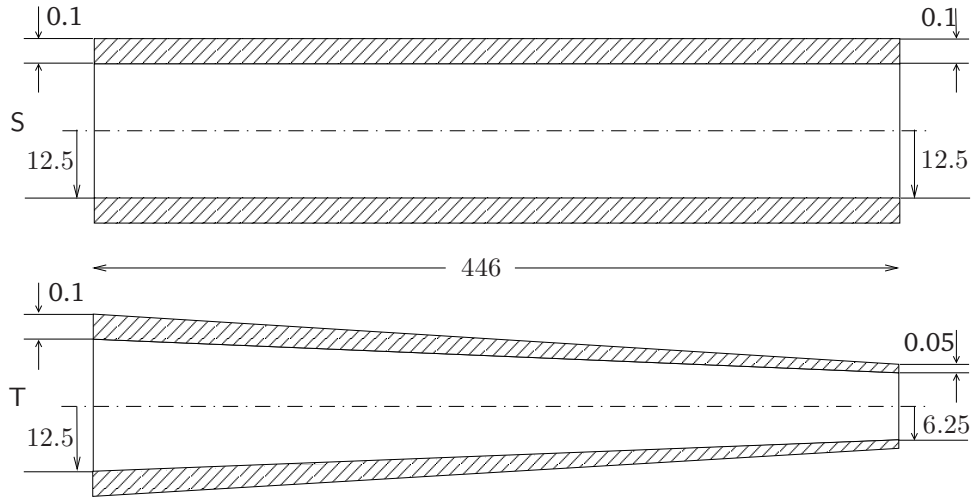


Figure 3.4: Schematic representation of the two polyurethane tubes. Tube S (serie PUt25.450) is straight with constant wall thickness and vessel T (serie PUt25.450t) is tapered with a varying wall thickness to obtain a constant wave speed. Dimensions are in [mm].

of water in the tube and the duration of the opening of the solenoid valve which initiated the pulse was set to be 50 [ms]. Measurements were performed at ten positions along the 460 [mm] length (3 % stretched) of the vessel, i.e. at $z=[29\ 50\ 100\ 150\ 200\ 250\ 300\ 350\ 400\ 450]$ [mm]. Measurements at each position were repeated sixteen times per position, the mean of which was taken for further processing.

3.2.4 Parameter estimation

The parameters used in the description of the constitutive relation (3.13) are obtained directly from the wave propagation experiments. The Young modulus of the parallel spring E_e can be derived from the total pressure difference between the start and the end of the wave propagation experiment Δp , in combination with the volume increase during the opening of the solenoid valve ΔV . Assuming that the material is completely relaxed at the end of the experiment, the wall behaviour can be modelled as purely elastic according to equation (3.4), so E_e can be determined using the static compliance as

$$E_e = \frac{2\pi(1 - \mu^2)La_0^3}{h} \frac{\Delta p}{\Delta V} \quad (3.23)$$

where L is the length of the polyurethane vessel and a_0 should now be interpreted as the static radius of the vessel after the waves have attenuated. Note that for the tapered vessel this radius should be determined by assuming a quadratic decay of the compliance with respect to z , because

$$C \propto \frac{a^3}{h} \quad \text{with} \quad h \propto a \quad \text{and} \quad a \propto z \quad \text{so} \quad C \propto z^2. \quad (3.24)$$

The values of E_v and η_w are estimated using wave analysis in the frequency domain. By assuming that the contribution of non-linear and frictional forces can be neglected in our model. The governing equations for wave propagation in straight vessels without leakage can then be derived as

$$\left. \begin{aligned} C \frac{\partial p}{\partial t} + \frac{\partial q}{\partial z} &= 0 \\ \frac{\partial q}{\partial t} + \frac{A}{\rho} \frac{\partial p}{\partial z} &= 0 \end{aligned} \right\} \quad (3.25)$$

with C the compliance as defined in (3.4). Due to the linearity assumed, this set of equations can be solved in the frequency domain by introducing harmonic solutions

$$p(\omega, z, t) = \hat{p}(\omega, 0) e^{i(\omega t - kz)} \quad (3.26)$$

$$q(\omega, z, t) = \hat{q}(\omega, 0) e^{i(\omega t - kz)} \quad (3.27)$$

where $\hat{p}(\omega, 0)$ and $\hat{q}(\omega, 0)$ are the complex amplitudes of p and q respectively measured at $z = 0$, and k is the complex wave number. By substituting these harmonic solutions into (3.25) an expression for k can be derived as

$$k(\omega) = \pm \sqrt{\frac{\rho C}{A}} \omega. \quad (3.28)$$

For viscoelastic tubes, a complex Young's modulus can be defined as $E^* = E_r(1 + if_v)$ with $f_v = E_i/E_r$, where E_r and E_i are the real and the imaginary part of the modulus respectively. Substituting this relation in equation (3.4) for thin-walled vessels and inserting the expression obtained for C in (3.28) yields

$$k = \frac{\omega}{c_0} \frac{1}{\sqrt{1 + if_v}}. \quad (3.29)$$

For small values of f_v this expression can be approximated by

$$k \approx \frac{\omega}{c_0} \left(1 + \frac{1}{2} if_v\right). \quad (3.30)$$

For the standard linear-solid model, the expressions for E_r and E_i can be derived by introducing harmonic solutions

$$\sigma(\omega, z, t) = \hat{\sigma}(\omega, 0) e^{i(\omega t)} \quad (3.31)$$

$$\epsilon(\omega, z, t) = \hat{\epsilon}(\omega, 0) e^{i(\omega t)} \quad (3.32)$$

into equation (3.15). Its complex modulus $E^*(\omega)$ is then defined as

$$E^*(\omega) = \frac{\hat{\sigma}}{\hat{\epsilon}} = \frac{E_e}{1 - \mu^2} \frac{1 + i\omega\tau_\sigma}{1 + i\omega\tau_\epsilon} \quad (3.33)$$

or

$$E^* = \frac{E_e}{1 - \mu^2} \left[\frac{1 + \tau_\sigma\tau_\epsilon\omega^2}{1 + \tau_\epsilon^2\omega^2} + i \frac{(\tau_\sigma - \tau_\epsilon)\omega}{1 + \tau_\epsilon^2\omega^2} \right]. \quad (3.34)$$

Fraction f_v of the standard linear-solid model can thus be written as

$$f_v = \frac{E_i}{E_r} = \frac{(\tau_\sigma - \tau_\epsilon)\omega}{1 + \tau_\sigma\tau_\epsilon\omega^2} \quad (3.35)$$

By determining the imaginary part of wave number k from the experiments, using equation (3.30) an estimate for fraction f_v can be obtained. This imaginary part of k represents the attenuation of the measured waves so it can be estimated by determining the attenuation constant of the pressure pulse. To do so, the pressure as a function of time measured at $z = 0.25$ [m] is used because at this position the forward and backward travelling waves can be separated on sight. By determining the maximum value of each pressure pulse and the corresponding travelled distance of each pulse (after all, the distance of $z = 0.25$ [m] to the reflection points is known) an attenuation constant can be found by fitting an exponential function according to

$$p = X_3 + X_2 e^{-X_1 z} \quad (3.36)$$

through these maxima. The value of X_1 , found by a least squares fitting procedure, is an approximation of the attenuation rate and can be compared to the imaginary part of wave number k . Introducing X_1 in equation (3.30) gives

$$f_v = 2 \frac{c_0}{\omega} X_1. \quad (3.37)$$

where wave speed c_0 can easily be found by dividing the travelled distance of each reflected wave peaks through the elapsed time. ω can be estimated from the length (in time) of the flow pulse at the inlet as derived in the previous section. Knowing now the value of f_v , c_0 , ω and E_e from the experiment data, in combination with the analytical expression for f_v from (3.35) a relation between E_v and η_w can be obtained. In conclusion, the value of E_v is varied to obtain a proper wave speed, changing the value of η_w accordingly. For the tapered tube, the same value of f_v is adopted as defined for the straight tube. The values of E_v and η_w for the tapered vessel are also obtained by fitting the computational wave speed to the experimental data. To illustrate the sensitivity of the computational results to these parameters, computations were executed with a 30% variation on each of them. The choice of a 30% variation on all three parameters is based on the expectation that it should be possible to measure these parameters in vivo with an accuracy of at least 30%.

3.3 Results

Parts of the results shown in this section are obtained from Giannopapa (2004), under the courtesy of the author. To ensure that the vessels undergo small deformations during the experiment the vessel was inflated incrementally by repeatedly adding a known amount of fluid to the closed vessel. The resulting pressure as a function of the radius (a) is presented in figure 3.5, showing a linear relation regardless of the pressure level. The corresponding strains are less than 3% and may be considered small.

To assess the reliability and reproducibility of the results for each of the measured variables their standard deviations σ were determined. Typical values of σ for the pressure and flow signal are presented in figure 3.6 and are in range of the noise of the signal.

With respect to the estimation of the parameter E_e used in the standard linear-solid model, total pressure changes Δp of 1.0 [kPa] and 2.2 [kPa] were found for vessels S and T respectively. The volume increase was 2.57 [ml] in both cases, resulting in values for E_e as given in table 3.1 for both tubes. Figure 3.7 shows the maximum values of each pressure pulse passing through $z = 0.25$ [m] of the straight vessel as a function of the travelled distance, along with an exponential fit through these points according to equation (3.36). This exponential decay resulted in $X_1 = 1.27$. The wave speed c_0 and radial frequency ω were determined to

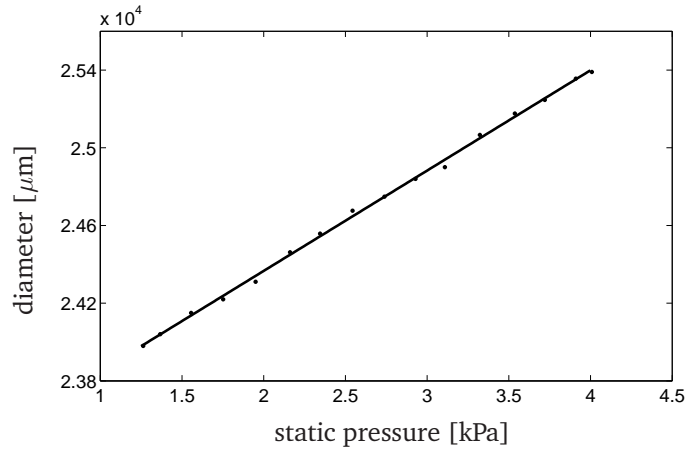


Figure 3.5: Initial diameter versus static pressure measured in the straight vessel S (dots). The straight line is a linear fit through the measured data and shows the linear relation between the diameter and the pressure.

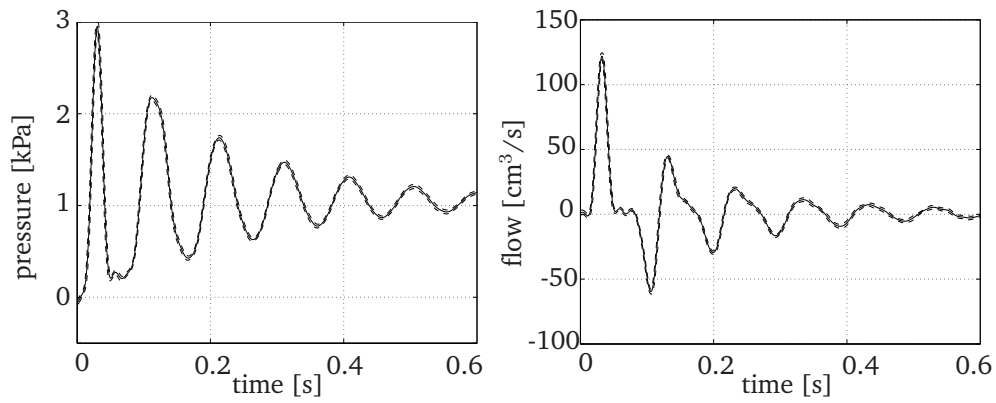


Figure 3.6: Typical result of the sixteen measurements at one position. The solid line indicates the mean value of the pressure and the flow (left plot and right plot respectively) and the dashed lines show this mean \pm its standard deviation.

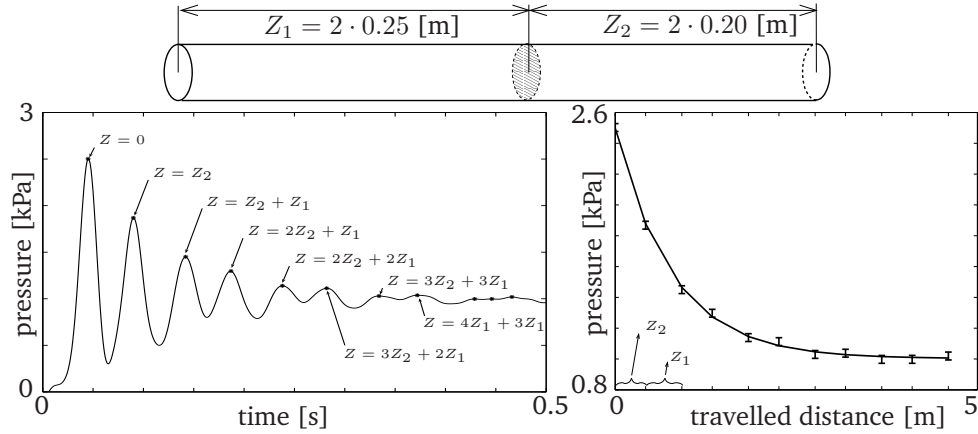


Figure 3.7: Attenuation of the pressure wave in vessel S. At the top a schematic representation of the polyurethane vessel, indicating the measuring position at $z = 0.25$ [m]. On the left the pressure as a function of time measured at $z = 0.25$ [m] where the *'s indicate the pressure peaks. Z_1 and Z_2 refer to the distances travelled by the pulse between each pulse crossing $z = 0.25$ [m]. The right plot shows the pressure peaks as a function of the accumulated travelled distance including an exponential fit through these points according to equation (3.36). The errorbars indicate the standard deviation of the measurements for each peak.

be 9.8 [m/s] and 126 [s^{-1}] respectively in the straight vessel and so, according to (3.37) an imaginary fraction of $f_v = 0.15$. This is in range of the viscous fraction observed in arterial walls, according to Learoyd and Taylor (1966). The corresponding values of E_v and η_w for both vessel types (based on f_v from the straight vessel) are presented in table 3.1.

The simulations are performed using the fluid and solid parameters as given in table 3.1 for both vessels. The geometrical input for the computations is obtained by first stretching the length of the vessel as taken from figure 3.4 by the 3% axial pre-strain and next increasing its radius to a_0 based on the pre-load of 3 [kPa]. The thus obtained geometry and pressure are referred to as the initial state and will be indicated with a subscript $_0$. The one-dimensional spatial domain is discretised using eleven sixth-order spectral elements whose edge nodes are positioned at either the edge of the total domain or at positions corresponding to the mea-

parameter	vessel S	vessel T	units
ρ	$9.98 \cdot 10^2$	$9.98 \cdot 10^2$	kg m^{-3}
η	$1.04 \cdot 10^{-3}$	$1.04 \cdot 10^{-3}$	$\text{kg m}^{-1} \text{s}^{-1}$
μ	0.5	0.5	-
E_e	$1.7 \cdot 10^7$	$2.1 \cdot 10^7$	$\text{kg m}^{-1} \text{s}^{-2}$
E_v	$7.6 \cdot 10^6$	$7.4 \cdot 10^6$	$\text{kg m}^{-1} \text{s}^{-2}$
η_w	$5.0 \cdot 10^4$	$5.1 \cdot 10^4$	$\text{kg m}^{-1} \text{s}^{-1}$

Table 3.1: parameters used for the simulations.

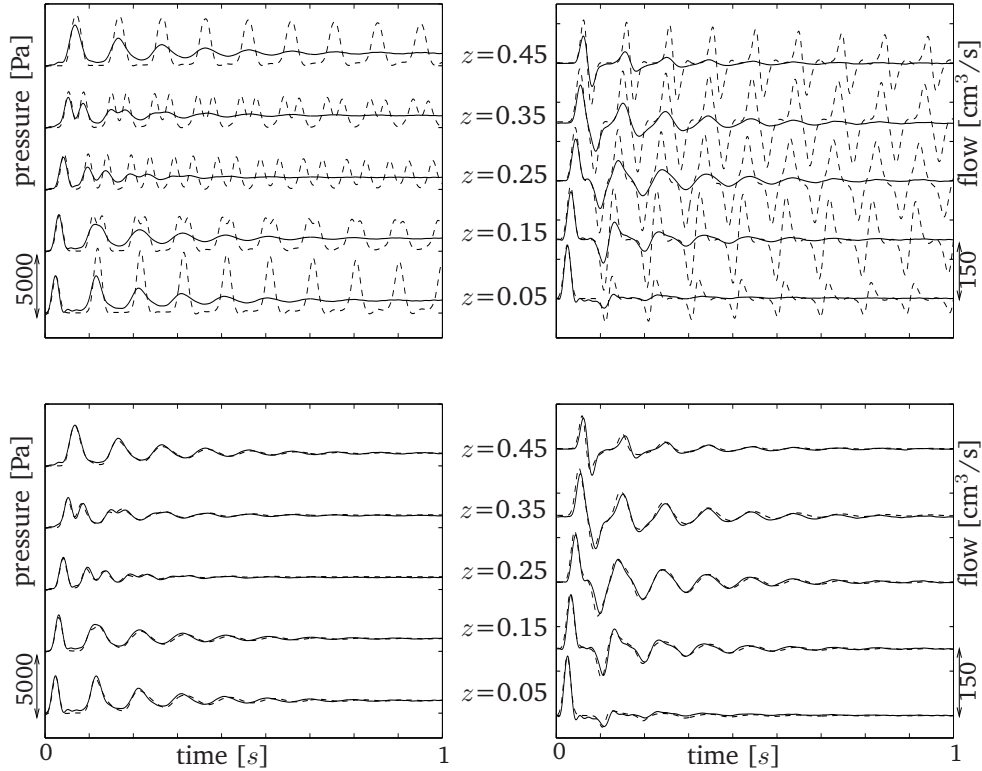


Figure 3.8: The pressure (left) and the flow (right) as a function of time measured at five positions in the straight vessel S (solid lines), along with the corresponding pressure and the flow from numerical simulations (dashed lines). The top figures show the numerical solutions based on purely elastic wall properties whereas the bottom pictures show the solutions from computations with viscoelastic wall properties

surement sites. As temporal discretisation a constant time step size is chosen at $\Delta t = T/50$ [s], with $T = 0.05$ [s] the pulse duration. The boundary conditions for the simulation at the inlet and the end of the vessels are taken from the experimental setup. The end is closed (i.e. $q|_{z=L} = 0$) and at the inlet ($z = 0$) a flow pulse is prescribed, based on a linear transformation of the experimental flow data from the measured positions to the inlet. Apart from the simulations using the viscoelastic model for the arterial wall, also computations with linear elastic wall properties are performed by setting the Young's modulus of the serial spring to $E_v = 0$ and increasing E_e to match the experimental wave speed. In figure 3.8 the computed pressure and flow of these two simulations at 5 positions in tube S are plotted against time, together with their measured counterparts from Giannopapa (2004). From the experimental results, the propagation of both the pressure and the flow waves through the polyurethane vessel can be clearly identified by the time difference between the arrival of the first pulse at $z = 0.05$ [m] and the arrival of this pulse at $z = 0.35$ [m]. Furthermore, at $z = 0.45$ [m] the pressure pulse has almost doubled in height because of a positive reflection at the closed end. The flow

pulse at this position is reflected negatively and becomes positive again after a negative reflecting at the now closed solenoid valve. The pressure wave remains positive due to exclusively positive reflection. During the travelling of both the pressure and the flow waves through the polyurethane vessel, the waves clearly attenuate to finally result in zero flow and a constant pressure, in equilibrium with the circumferential stress within the vessel wall. When considering the numerical results obtained by the model using a linear elastic constitutive relation, a good prediction of the reflection characteristics is found. However, since the attenuation of the waves in the experiment is mainly caused by the viscoelastic properties of the vessel wall, the attenuation of the waves obtained from the computational model using linear elastic wall properties is insufficient. The wave propagation model using viscoelastic wall properties on the other hand, provides an accurate prediction of the propagation of the pressure and flow wave and its attenuation (see figure 3.8). A deviation of the Young modulus E_e of 30%, as illustrated in the 2 plots at the top of figure 3.9, shows a significant change in the wave characteristics. A decrease in E_e leads to a decrease of the wave speed and the pressure amplitude of about 16% and an the expected decrease of the static pressure of 30%. An increase of E_e shows the opposite effect. A 30% variation of parameters E_v and η_w shows no significant change in the wave speed and static pressure, and only small changes of less than 5% in the wave attenuation. Considering the results corresponding to the tapered vessel T as visualised in figure 3.10, the same observations can be made with respect to the comparison between experimental and numerical data. The model using a linear elastic material law underestimates the damping of the system whereas the model based on the standard linear-solid model properly describes the attenuation of both the pressure and flow waves. In figure 3.11 a comparison is made between wave propagation in the straight and in the tapered vessel according to the computational model. The tapering of vessel T causes an expected increase in pressure amplitude towards the distal end (pressure pulse steepening) due to continuous reflections. We also see that the wave velocity in the tapered vessel is higher than the wave velocity in the straight vessel owing to the difference in Young's modulus E_e . The difference in the attenuated pressure is a result of the difference in Young's modulus as well as a difference in the initial volume contained by both vessels.

3.4 Discussion

The wave propagation model of chapter 2 is extended with a constitutive equation based on the viscoelastic behaviour of the standard linear-solid model. The resulting model is validated by a comparison of the pressure and flow obtained from the numerical model to the pressure and flow measured in an experimental setup in which wave propagation through viscoelastic polyurethane tubes, constrained in a water filled tank, was monitored (Giannopapa (2004)). The pressure and flow data measured in two tubes were used, one being a straight vessel with constant wall thickness and the second being tapered with a varying wall thickness to obtain a constant wave speed. The pressure and the flow measured in these two tubes were shown to be reproducible with a standard deviation in range of the signal noise. Also, in the relevant pressure range, a linear relation between the stress and strain of the polyurethane vessels was found, with strains of less than 3% for the pressure pulses produced.

The estimation of the parameters used in modelling the vessel wall behaviour (E_e, E_v, η_w) was based on the wave characteristics of the measurement data from the experimental setup. E_e was obtained from the static compliance after the waves were fully attenuated and a relation between E_v and η_w was obtained from the attenuation constant of the pressure pulse. Their final values were chosen to fit the experimental wave speed. With this method, the standard

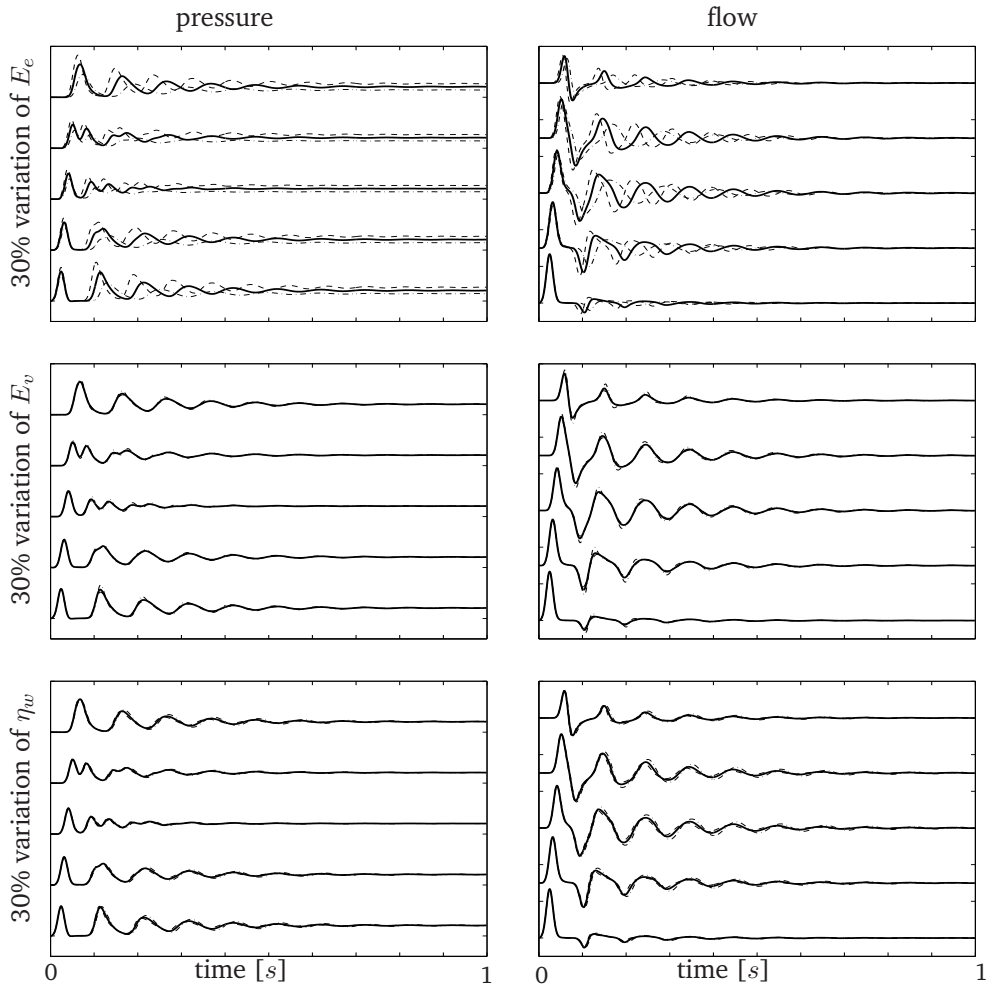


Figure 3.9: Variation of the pressure (left) and the flow (right) as a result of a change in E_e (top), E_v (centre) and η_w (bottom). The solid lines indicate the solutions when using the parameters as estimated, the dashed lines show the pressure and flow when increasing one parameter with 30% and the dash-dot lines are produced by decreasing one parameter with 30%.

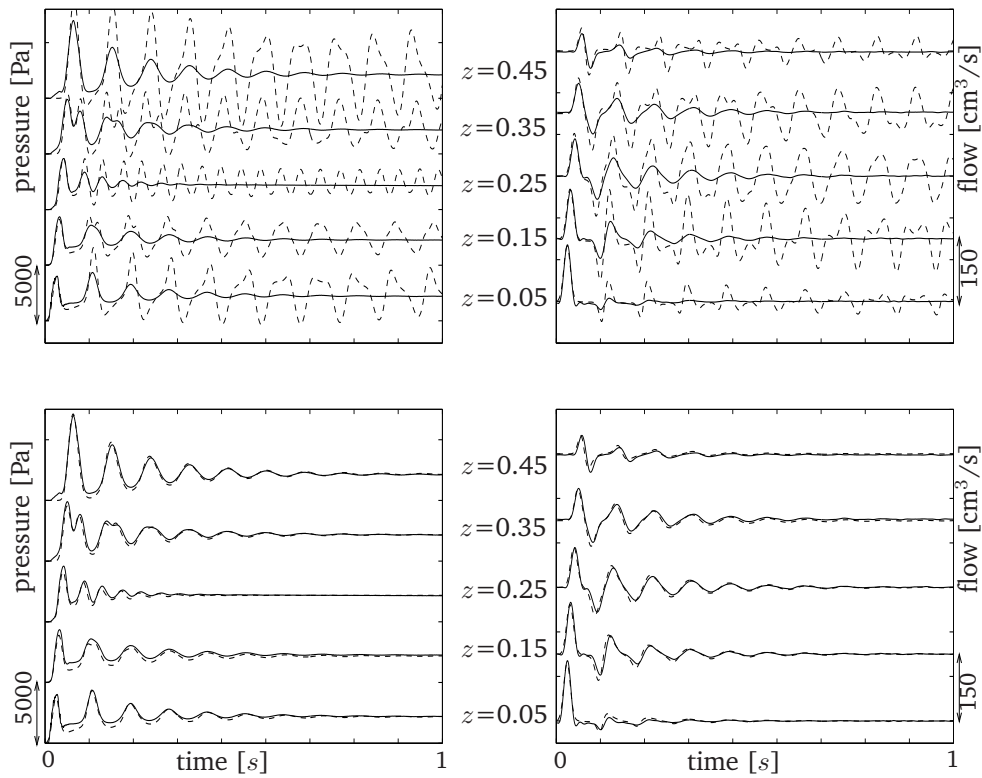


Figure 3.10: The same as figure 3.8 but now for the tapered vessel T.

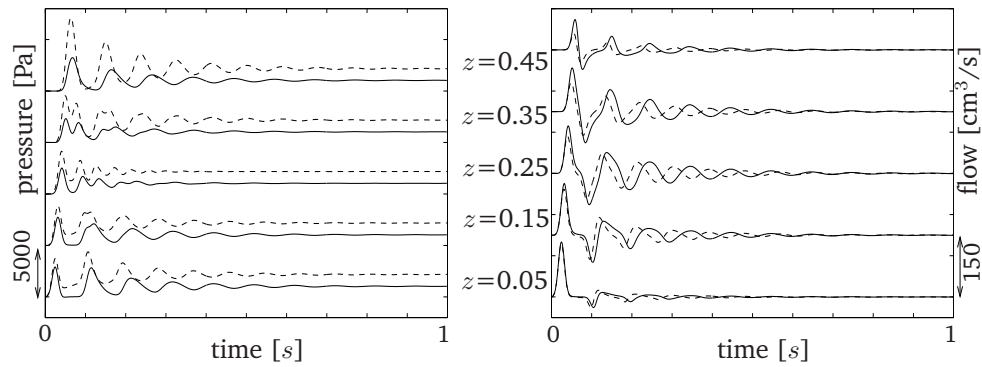


Figure 3.11: Comparison between the numerical pressure and flow as a function of time in the straight vessel S (solid line) and the corresponding solutions in the tapered vessel S (dashed line).

linear-solid model using the estimated parameters describes the mechanical behaviour of the polyurethane vessel wall in combination with its surrounding medium, without the knowledge of the mechanical properties of the individual components. In the physiological situation, when the propagation of pressure and flow waves through the arterial system is modelled, the parameters E_e , E_v and η_w should also describe the behaviour of the local arterial wall in combination with its surrounding tissues. They can be obtained by simultaneously measuring the local wave speed and the arterial wall distension.

A variation of parameters E_e , E_v and η_w of 30% shows that the system is sensitive to errors made in the determination of E_e , but only weakly sensitive to errors made in the estimation of the attenuation constant. A comparison between the experimental and the computational pressure $p(z, t)$ and flow $q(z, t)$ using the estimated parameters showed good agreement in the pressure and the flow wave propagation. The wave speed and wave attenuation are well described by the 1D model as well as the pressure pulse steepening due to the geometric non-linearity of the tapered vessel. The small pressure increase before the arrival of the first pulse in the measurement data of the tapered vessel, as clearly seen at $z = 0.45$ [m], is probably caused by a vibration of the setup caused by the closing of the solenoid valve.

Although the proposed model has shown to be able to accurately predict the propagation of pressure and flow waves through the laboratory setup, its applicability to assess wave propagation through the arterial system still needs further research. Primarily, the arterial system is far from ideal with respect to the assumption made in one-dimensional modelling. Blood flow through geometric discontinuities such as bends, bifurcations and arterial pathologies (e.g. stenoses and dilation) may not be categorised as one-dimensional since the radial components of the velocity field can no longer be neglected. The propagation of pressure and flow waves through such segments needs to be examined more thoroughly before wave propagation in the total arterial tree can be accurately predicted. Furthermore, the local material properties of the arterial wall and its surrounding organs need to be determined to obtain reliable values for its compliance and attenuation characteristics. With respect to the blood viscosity η , the influence of shear thinning on the wall shear stress must be evaluated to determine whether the assumption of purely Newtonian behaviour is valid in estimating the frictional forces in one-dimensional wave propagation.

3.5 Conclusion

A time-domain based wave propagation model is developed where the constitutive relation is based on the mechanical behaviour of a Kelvin body. The model is validated by a comparison to data from an experimental setup of fluid flow through viscoelastic straight and tapered vessels. Using the developed wave propagation model, the propagation and attenuations of pressure and flow waves through viscoelastic vessels such as arteries can be accurately predicted.

Chapter 4

The pressure drop over arterial stenoses under physiological conditions

4.1 Introduction

Research on one-dimensional wave propagation in distensible tubes is often motivated by its applicability to the human arterial system. An appropriate one-dimensional model may provide realistic and clinically relevant information on the pressure and the blood flow through the arterial tree. In the derivation of the one-dimensional equations of mass conservation and momentum balance, however, assumptions on the local lumen geometry and the resulting velocity profiles are made that may not always hold in patient-specific arterial systems. Primarily, the axial change in lumen radius is assumed to be gradual so that the blood velocity in radial direction of the blood vessel is negligibly small with respect to its axial component. This assumption is used in the derivation of the one-dimensional equations from the fully three-dimensional Navier-Stokes equation, but also in the adoption of a velocity profile function to obtain realistic contributions of the friction and convection forces in the one-dimensional momentum balance (chapter 2). It may well hold when modelling wave propagation through straight or slightly tapered vessels, but when modelling a patient-specific arterial tree, pathological regions such as stenoses can no longer be realistically modelled using one-dimensional theory only. The velocity components in the radial direction are no longer negligibly small with respect to their axial counterpart and the velocity profiles can no longer be based on the theory of fully developed flow in straight vessels. So, to obtain a wave propagation method that is suited to model the propagation of pressure and flow waves travelling through patient-specific arterial systems, a one-dimensional model of stenoses is needed. Such a model can be derived when a relation between the pressure drop as a result of the stenosis and the local flow characteristics is known.

In literature, much attention has been paid to the (time-dependent) blood flow near stenoses (Siouffi et al. (1984); Tu et al. (1992); Cavalcanti (1995); Tu and Deville (1996); Siouffi et al. (1998); Chakravarty and Mandal (2000); Long et al. (2001); Mandal (2005)), with a focus on the local velocity field and the wall shear stress. Our interest, however, is mainly on the axial pressure drop as a result of the presence of a stenosis, regardless of the corresponding velocity field. Other work in one-dimensional wave propagation that included stenotic regions (Rooz et al. (1982); Porenta et al. (1986); Stergiopoulos et al. (1992, 1996); Steele et al. (2003); Bakirtas and Antar (2005)) model them either using the assumption of inviscid fluid, or based on the work of Young (1979). This work provides an overview of research on the pressure drop over stenoses as a function of the stenosis geometry and the local flow characteristics expressed in the Reynolds number and the Womersley parameter. This relation is obtained from experimental research on steady (Young and Tsai (1973a)) and unsteady (Young and Tsai (1973b)) flow through rigid stenoses models. A geometry dependent relation between the flow q through a stenosis and the pressure drop Δp_s over the stenosis is found, composed of a viscous term, a non-linear 'turbulence' term and an unsteadiness term, according to

$$\Delta p_s = \frac{\eta K_v}{2\pi a_0^3} q + \frac{\rho K_t}{2A_0^2} \left(\frac{A_0}{A_s} - 1 \right)^2 |q|q + \frac{\rho K_u L_s}{A_0} \frac{\partial q}{\partial t}. \quad (4.1)$$

Here, a_0 and A_0 are the radius and cross-sectional area respectively of the vessel lumen proximal to the stenosis and A_s is the cross-sectional area of the lumen at the neck of the stenosis. L_s represents the stenosis length and ρ and η are the blood density and viscosity. The coefficients K_v , K_t and K_u are empirically determined constants defined as

$$\begin{aligned} K_v &= 16 \frac{L_a}{a_0} \left(\frac{A_0}{A_s} \right)^2 \\ K_t &= 1.0 \text{ (steady flow)} \quad K_t = 1.52 \text{ (unsteady flow)} \\ K_u &= 1.2 \end{aligned} \quad (4.2)$$

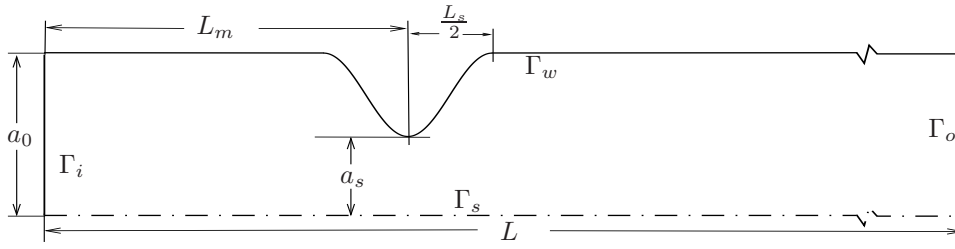


Figure 4.1: Scaled representation of the stenosed vessel, indicating its measures and the boundaries used for the computations.

The expression for K_v is dependent on the stenosis shape and for axisymmetric stenoses with a constant radius A_s over its total length, the expression for L_a is

$$L_a = 0.83L_s + 32.8a_s, \quad (4.3)$$

with a_s the inside radius of the hollow plug (see also figure 4.1). For more complex stenosis shapes, Young suggests that K_v may be estimated by assuming parabolic velocity profiles at each cross-section of the stenosis and integrating the resulting wall shear stress over the stenosis length.

When applying equation (4.1) to unsteady flow in an unobstructed rigid tube ($A_s = A_0$), the non-linear part vanishes and the viscous contribution is independent of the Womersley parameter α . From the analytical solution for instationary flow through straight pipes, however, the viscous contribution (and so K_v) is expected to depend on the frequency (see chapter 2).

In this research a finite element method in a two-dimensional axisymmetric Eulerian domain is used to investigate the effect of stenoses on the pressure gradient in a rigid tube. By simulating steady flow situations at low Reynolds numbers ($0.33 < Re < 10$), we will investigate whether the viscous coefficient K_v can indeed be determined by assuming parabolic velocity profiles throughout the stenosis. Next, by simulating unsteady flow at various frequencies, the frequency dependency of both the viscous term K_v and the unsteadiness term K_u will be investigated. To also validate the turbulence coefficient K_t , computations of both steady and unsteady flow situations at higher Reynolds numbers ($10 < Re < 1000$) will be performed. Finally, the pressure drop over a stenosis when prescribing a physiological flow pulse through the stenosis is simulated to validate the final relation between Δp_s and the flow characteristics. The methods used are discussed and the final stenosis relation is compared to the relation defined by Young (1979).

4.2 Methods

To investigate the pressure drop over a stenosis a two-dimensional axisymmetric finite element method based on the Navier-Stokes equations in cylindrical coordinates is used. A representation of the domain used is shown in figure 4.1. The radius of the healthy part of the stenosed vessel is chosen to be a_0 and the stenosis geometry is described according to

$$a = a_0 - \frac{a_s}{2} \left[1 - \cos \left(2\pi \frac{z - L_m - L_s/2}{L_s} \right) \right] \quad \text{for } L_m - L_s/2 < z < L_m + L_s/2 \quad (4.4)$$

where a_s is the maximum constriction in the centre of the stenosis, $L_m = 50a_0$ dictates the axial location of this centre and z is the axial position. The length of the stenosis is set at

$L_s = 25a_0$ based on physiological data from chapter 6. It will not be varied in the derivation of the relation between the pressure drop over the stenosis and the flow, but it will be introduced as a variable in this relation. The vessel has a total length of $L = 250a_0$ to provide sufficient length distal to the stenosis for the velocity field to develop. The stenosis severity S (defined as $S = (1 - A_s/A_0) \cdot 100\%$) is varied between 0, 65, 75 and 85% by setting a_s to 4.00, 2.37, 2.00 and 1.55 [10^{-4} m]. The spatial domain is discretised using 960 bi-quadratic quadrilateral elements of the Crouzeix-Raviart type. In axial direction 120 elements are used, 20 elements of which are between $0 \leq z < L_m$ and 100 elements are between $L_m \leq z \leq L$. The mesh is refined towards the stenosis with a ratio 1:3 between the length of the elements near the stenosis and the ends of the fluid domain. In radial direction 8 elements are used with a similar mesh refinement towards the vessel wall.

The fluid within the domain is modelled as Newtonian with density $\rho = 1.05 \cdot 10^3$ [kg/m^3] and dynamic viscosity $\eta = 5 \cdot 10^{-3}$ [$\text{Pa}\cdot\text{s}$]. At the inlet Γ_i a velocity profile is prescribed, the outlet Γ_o is left stress free and the vessel wall Γ_w is endowed with no slip conditions. At the axis of symmetry Γ_s the radial velocity is constrained.

$$\begin{cases} v_z &= v_z(\alpha, t, r), & v_r = 0 & \text{at } \Gamma_i \\ v_z &= 0, & v_r = 0 & \text{at } \Gamma_w \\ v_r &= 0 & & \text{at } \Gamma_s \\ \boldsymbol{\sigma} \cdot \mathbf{n} &= 0 & & \text{at } \Gamma_o \end{cases} \quad (4.5)$$

with v_z and v_r the fluid velocities in axial and radial direction respectively, $\boldsymbol{\sigma}$ the Cauchy stress tensor and \mathbf{n} the vector normal to the outflow plane Γ_o . Simulations are performed using steady flow conditions at the inlet Γ_i by providing Poiseuille profiles with a flow q of 0.01, 0.02, 0.04, 0.08, 1, 2, 4, 8, 10, 12, 14, 18, 20, 22, 24, 28 and 30 [10^{-6} m^3/s]. The corresponding Reynolds numbers Re , according to

$$Re = \frac{2\rho}{\pi\eta a_0} q, \quad (4.6)$$

are in a range of $Re = [0.33 - 1000]$. The results of these computations are divided into two regions, i.e. low Reynolds numbers ($0.33 < Re < 10$) and high Reynolds numbers ($10 \leq Re < 1000$).

Next, computations are performed by prescribing oscillatory flow according to

$$q(t) = \bar{q}[1 - \cos(2\pi ft)] \quad (4.7)$$

at the inlet Γ_i , where t is the time and \bar{q} is the time average of the flow signal. Simulations with frequencies f of 0.1, 0.2, 0.4, 0.8, 1, 2, 4, 8 and 10 [Hz] are performed and for each frequency five cycles are simulated the last of which is monitored. The resulting Womersley parameter α , defined by

$$\alpha = a_0 \sqrt{\frac{2\pi\rho f}{\eta}} \quad (4.8)$$

varies between $\alpha = 1.45$ and $\alpha = 14.5$. The temporal discretisation Δt for each frequency is $\Delta t = T/100$ with T the cycle period of $T = 1/f$. The time-dependent velocity profiles that are prescribed at the inlet Γ_i , corresponding to each frequency, are based on the Womersley solution. For each frequency a wide range of Reynolds numbers ($Re = [0.33 - 1000]$) is again addressed with average flows \bar{q} of 0.005, 0.01, 0.02, 0.04, 0.05, 1, 2, 4, 5, 6, 7, 9, 10, 11, 12, 14 and 15 [10^{-6} m^3/s] and a similar division into low and high Reynolds numbers is made.

Finally, a multi-harmonic physiological flow pulse through the stenosed ($S = 75\%$) femoral artery is prescribed, based on the shape of the flow pulse in the femoral artery by Olufsen and Peskin (2000). The shape of these stenoses is chosen equal to that of the other simulations but next to the standard length $L_s = 25a_0$ now also length of $L_s = 5a_0$ and $L_s = 50a_0$ are chosen to evaluate the influence of this variable.

The axial pressure distribution from each computation is obtained by taking the mean of the pressure over the discretised cross-sections. The pressure drop over the stenosis Δp_s is obtained by subtracting the pressure drop over the straight ('healthy') part of the vessel (which has a length of $L_h = L - L_s$), based on the analytical solution for fully developed flow in a straight pipe by Womersley (1957), from the total pressure drop over the tube. This analytical pressure drop Δp_a can be derived by Womersley's theory using

$$\Delta p_a = Z_L L_h q \quad \text{with} \quad Z_L = 2i\pi f \frac{\rho}{\pi a_0^4} \frac{1}{1 - F_{10}(\alpha)}. \quad (4.9)$$

Here, $F_{10}(\alpha)$ is the Womersley function according to

$$F_{10}(\alpha) = \frac{2J_1(s)}{sJ_0(s)}, \quad \text{with} \quad s = i^{3/2}\alpha \quad (4.10)$$

and J_0 and J_1 are Bessel functions of the first kind of order 0 and 1. For steady flow ($\alpha = 0$) this results in

$$\Delta p_a = R_0 \Delta L_h q \quad (4.11)$$

where $R_0 = 8\eta/(\pi a^4)$ represents the friction coefficient per unit of length for steady flow in a straight tube. Notice that the pressure drop is defined to be positive when the pressure gradient is negative, e.g. $\Delta p = p(\Gamma_i) - p(\Gamma_o)$.

Before performing the computations described above, the numerical method is tested by simulating fully developed flow through a straight pipe ($S = 0$) at Reynolds number $Re = 100$ for Womersley parameters $\alpha = 0, 5$ and 10 and comparing the computed local pressure to the pressure obtained from equation (4.9). The maximum deviation of the computed pressure to the analytical pressure was less than 2% of the analytical pressure. Also, for the mesh of the $S = 75\%$ stenosis, a mesh convergence test was performed for a steady computation at $Re = 100$. The pressure drop of the final mesh showed no significant improvement with further mesh refinement.

4.3 Results

Figure 4.2 shows the pressure as a function of the axial position for the steady flow simulation in the 75% stenosed vessel with flows of 1, 10 and 20 [10^{-6} m³/s] ($Re = 33, 334$ and 668) along with the analytical pressure in case of a straight tube without a stenosis. The presence of the stenosis at higher Reynolds numbers can be identified by a sudden pressure drop at the stenosis site and a slow pressure recovery distal to the stenosis. The sudden pressure drop at the entrance of the stenosis and the (partial) pressure recovery distal to the stenosis neck are a result of the change in cross-sectional area of the vessel lumen, according to Bernoulli's law. The recovery of the pressure distal to the stenosis is retarded because of the presence of a recirculation zone that locally influences the effective cross-sectional area as can be seen in figure 4.3 for steady flow with $q = 10^{-5}$ [m³/s]. Proximal to the stenosis and far enough distal to the stenosis the pressure gradient $\partial p/\partial z$ is similar to that for fully developed flow in

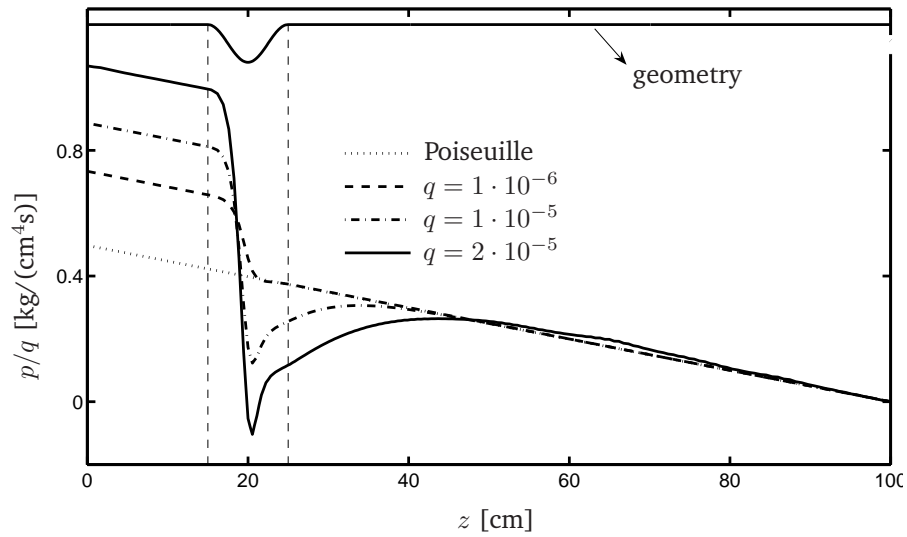


Figure 4.2: The pressure divided by the flow as a function of the axial position in the vessel, obtained from steady flow computations with flows of 1, 10 and 20 [10^{-6} m^3/s]. The dotted line shows the pressure based on Poiseuille flow in a straight tube.

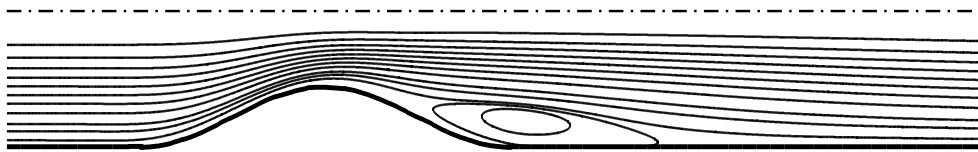


Figure 4.3: Scaled velocity field around the 75% stenosed vessel including a single vortex in a steady flow situation of $q = 1 \cdot 10^{-5}$ [m^3/s].

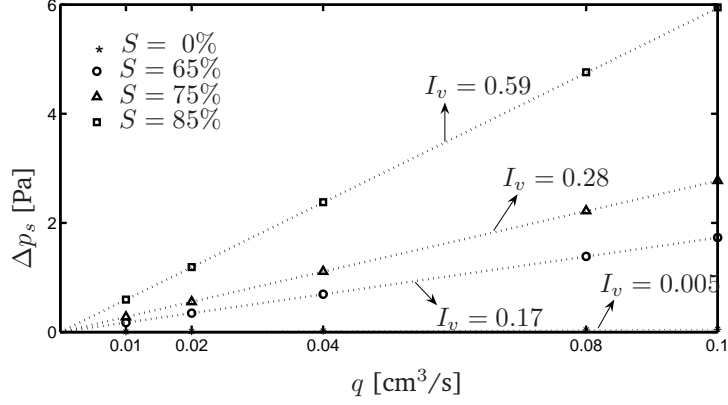


Figure 4.4: The pressure drop as a results of the stenosis versus the flow, for the steady flow simulations through stenoses with severities of $S = 0, 65, 75$ and 85% . The dotted lines show the linear relation between Δp_s and q according to equation (4.14).

a straight pipe. When considering steady flow at low Reynolds numbers, the unsteadiness and non-linear part can be neglected from (4.1) and so only the viscous part Δp_v of the pressure drop remains, according to

$$\Delta p_s = \Delta p_v = I_v q. \quad (4.12)$$

Looking at the pressure drop over the stenosis as a function of the flow for low Reynolds numbers obtained from the steady flow simulations (figure 4.4), for each stenosis indeed a constant friction coefficient I_v exists. The values of I_v are listed in table 4.3 for each stenosis severity. As expected, these values are identical to the analytical friction coefficient when assuming fully developed flow (Poiseuille profiles) at each position across the stenosis, according to

$$I_v = R_s = \int_0^{L_s} R(z) dz = R_0 \int_0^{L_s} \frac{a_0^4}{a^4(z)} dz \quad (4.13)$$

So, for steady flow at low Reynolds numbers, the pressure drop over a stenosis can be written as

$$\Delta p_s = R_s q \quad \text{with} \quad R_s = R_0 \int_0^{L_s} \frac{a_0^4}{a^4(z)} dz. \quad (4.14)$$

At higher Reynolds numbers, recirculation zones will develop and the non-linear term becomes increasingly important so, according to Young and Tsai (1973a):

$$\Delta p_s = R_s q + \Delta p_t = R_s q + \frac{\rho K_t}{2A_0^2} \left(\frac{A_0}{A_s} - 1 \right)^2 |q| q. \quad (4.15)$$

To estimate the value of K_t for each stenosis, the viscous pressure drop $\Delta p_v = R_s q$ as computed before was subtracted from the total pressure drop over the stenosis Δp_s , so the non-linear part

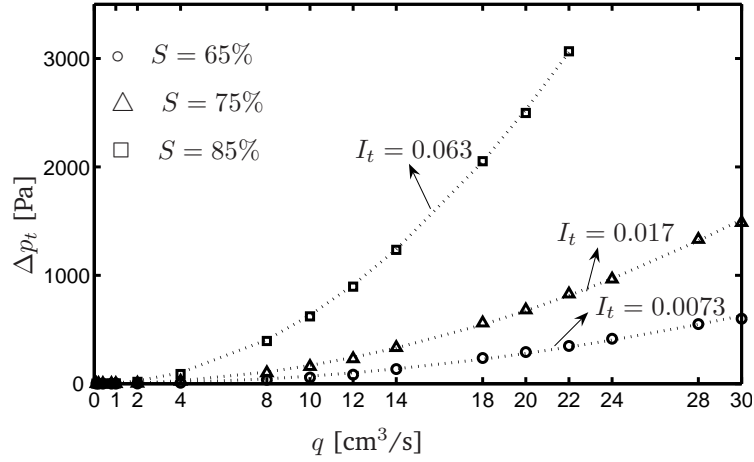


Figure 4.5: The pressure drop due to the non-linear term as a function of the flow in case of steady flow through stenoses with severities of $S = 65, 75$ and 85% . The dotted lines show the quadratic relations according to equation (4.16) using constant I_t as indicated.

severity	0%	65%	75%	85%
I_v	0.005	0.173	0.277	0.593
I_t	-	0.0727	0.0171	0.0632

Table 4.1: values of I_v and I_t for steady flow.

Δp_t remains,

$$\Delta p_t = I_t |q|q. \quad (4.16)$$

A clear quadratic relation between Δp_t and q exists as shown in figure 4.5, dependent on the stenosis severity S . The values of I_t are listed in table 4.3 for each stenosis severity. I_t can be written as

$$I_t = \frac{\rho K_t}{2A_0^2} \left(\frac{A_0}{A_s} - 1 \right)^2 \quad (4.17)$$

which means, that for our computations the value of K_t varies between 0.91 and 1.02, dependent on the stenosis severity. For steady flow, Young and Tsai (1973a) found values of K_t in the same range, so the pressure drop over a stenosis for stationary flow can be computed using equation (4.15).

Next, time-dependent flow through the stenosed vessel is investigated to determine the contribution of the unsteadiness to the pressure drop. Only the results for the 75% stenosed vessel are presented, except when mentioned otherwise. The flow signal with a frequency of $f = 1$ [Hz] and a time average flow $\bar{q} = 0.5 \cdot 10^{-6}$ [m³/s] is presented in figure 4.6 as a function of time, along with the corresponding pressure drop over the stenosis Δp_s and the pressure drop Δp_a over a length equal to the length of the stenosis L_s for the case no stenosis is present

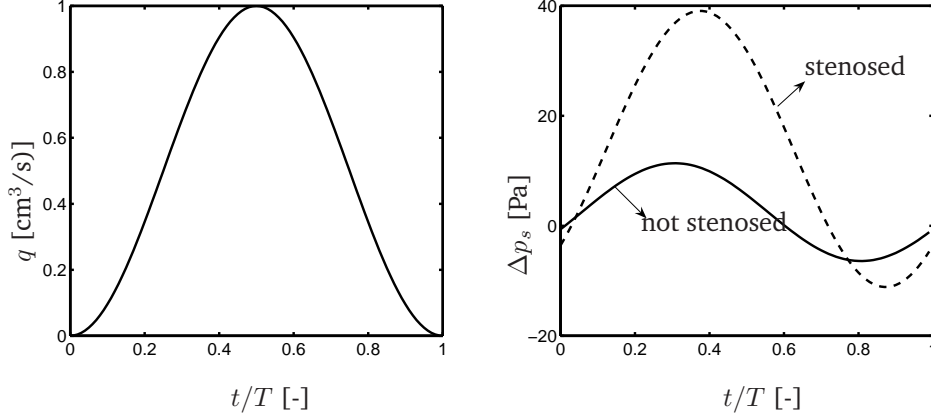


Figure 4.6: The flow (left) and pressure drop (right) as a function of time for oscillatory flow with a frequency of $f=1$ [Hz] and a mean flow \bar{q} of $0.5 \cdot 10^{-6}$ [m^3/s]. The dashed line indicates the pressure drop as a results of a stenosis of 75% and the solid line shows the pressure drop over a length of L_s when no stenosis is present.

($A_s = A_0$). According to Young and Tsai (1973b) the pressure drop Δp_v and Δp_t for the unsteady flow situation can be approximated by their expressions obtained from the steady flow simulations. An extra term, representing the contribution of the unsteadiness of the flow on the pressure drop over the stenosis can be added to this viscous and non-linear part obtained from steady flow computations, so

$$\Delta p_s = R_s q + \frac{\rho K_t}{2A_0^2} \left[\frac{A_0}{A_s} - 1 \right]^2 |q|q + \frac{\rho K_u L_s}{A_0} \frac{\partial q}{\partial t} \quad (4.18)$$

The pressure drop over the stenosis for oscillating flow at varying frequencies is again first investigated for low Reynolds numbers, so we can neglect the influence of the non-linear term. By subtracting the known contribution of the friction term obtained from the steady flow simulations from the total pressure drop, the pressure drop Δp_u caused by the unsteadiness of the flow remains. For $f = 1$ [Hz] and $\bar{q} = 0.5 \cdot 10^{-6}$ [m^3/s] this results in a relation between Δp_u and q as is illustrated in figure 4.7. The dashed line on the right-hand side of this figure shows that the relation between Δp_u and $\partial q/\partial t$ is not one-to-one. By multiplying the friction coefficient R_s with an 'optimisation' constant K_v , however, a linear relation between Δp_u and $\partial q/\partial t$ can be found as is shown in figure 4.8. Notice that for $\partial q/\partial t = 0$ the value of Δp_u is not equal to 0, so for low Reynolds numbers

$$\Delta p_s = K_v R_s q + \frac{\rho K_u L_s}{A_0} \frac{\partial q}{\partial t} + \Delta p_c \quad (4.19)$$

where Δp_c represents this offset. The procedure of optimising R_s to obtain a linear relation between Δp_u and $\partial q/\partial t$ is done for all unsteady computations on all stenosis geometries. Neither K_v nor the unsteadiness coefficient K_u seem to depend on \bar{q} but they do change with the Womersley parameter α . The relation between α and K_v is approximated using a quadratic fit according to

$$K_v = 1 + 0.053 \frac{A_s}{A_0} \alpha^2. \quad (4.20)$$

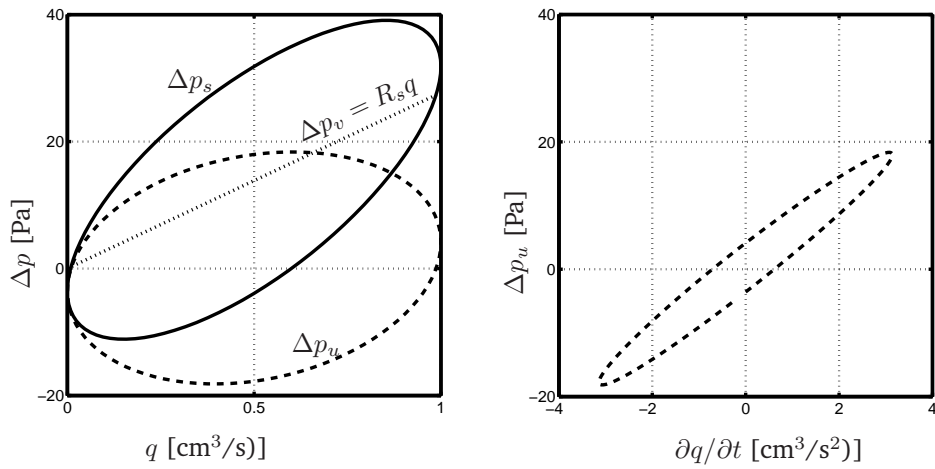


Figure 4.7: (left) The pressure drop as a function of the flow for $f=1$ [Hz] and $\bar{q}=1 \cdot 10^{-6}$ [m³/s]. The solid line represents the pressure drop over the 75% stenosis and the dotted line shows the viscous contribution to this pressure drop based on the value of I_v from the steady computations. The dashed line indicates the remaining pressure drop ($\Delta p_u = \Delta p_s - \Delta p_v$). (right) The remaining pressure drop (Δp_u) as a function of the flow change.

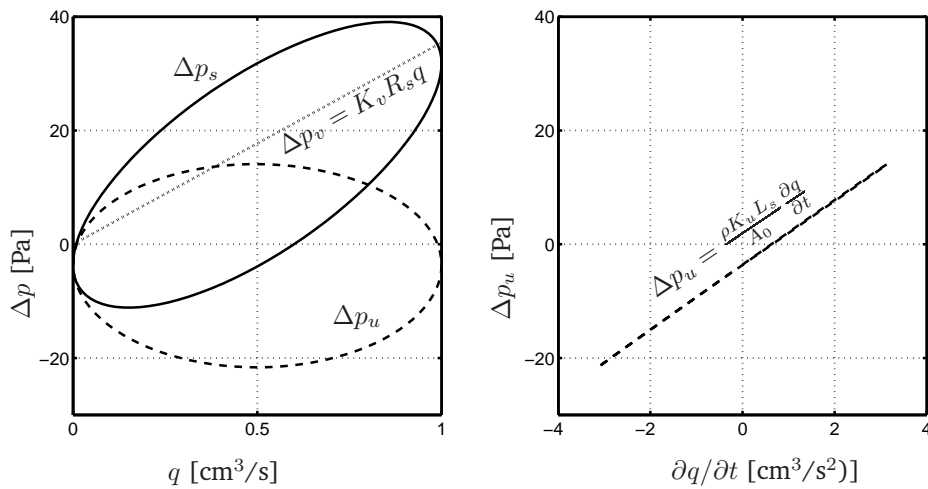


Figure 4.8: The same as figure 4.7 but now the viscous contribution to the pressure drop has been multiplied by K_v , so $\Delta p_v = K_v R_s q$. Now a linear relation exists between Δp_u and $\partial q / \partial t$.

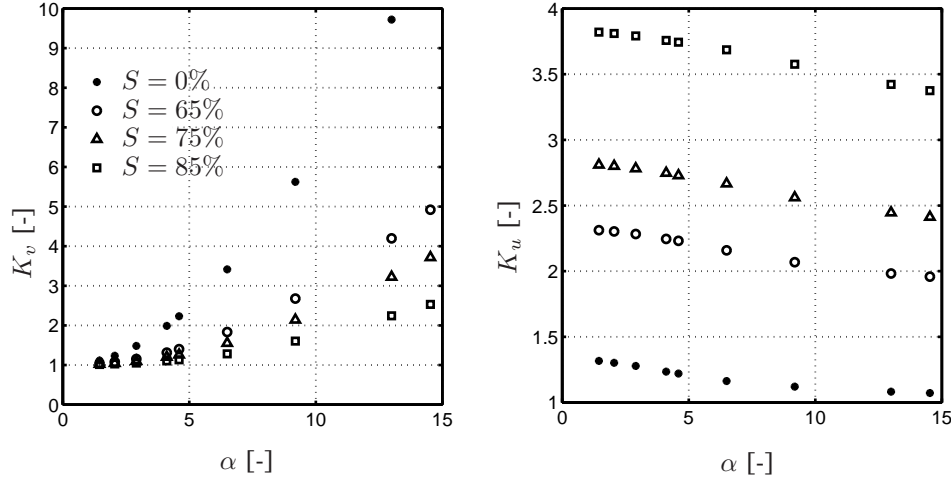


Figure 4.9: The viscous coefficient K_v (left) and the unsteadiness coefficient K_u (right) as a function of the frequency f for stenosis with severities of $S = 0, 65, 75$ and 85% . The values for K_u are obtained from equation (4.19).

and is depicted on the left in figure 4.9. Notice that, as the frequency approaches zero, the values of $K_v(\alpha)$ approach $K_v = 1$. Based on our simulations, the values of K_u vary in a range of $K_u = [1 - 4]$ (see figure 4.9, right), which is higher than the empirically determined value from Young of $K_u = 1.2$. When altering the 2^{nd} term on the right hand side of equation (4.19) by taking into account the shape of the stenosis, so

$$\Delta p_u = K_u L_u \frac{\partial q}{\partial t} \quad \text{with} \quad L_u = \frac{\rho}{A_0} \int_0^{L_s} \frac{a_0^2}{a^2(z)} dz, \quad (4.21)$$

the values for K_u are now in the range of $K_u = [1.05 - 1.35]$ with a mean value of $K_u = 1.2$ (figure 4.10). The dashed lines show the approximations for K_v according to equation (4.20). Note, that in relation (4.21) coefficient L_u is not a length scale but the local inertance of the fluid inside the stenosis. The offset Δp_c is caused by the phase difference between the flow signal and the pressure drop, similar to flow through straight vessels (Womersley (1957)) and so it depends on both \bar{q} and the frequency parameter α . Using a least squares fitting procedure provided by Matlab (The Mathworks, Inc) a linear relation is found between Δp_c and \bar{q} and a quadratic relation is found between Δp_c and α (Figure 4.11), so

$$\Delta p_c = K_c R_s \bar{q} \quad \text{with} \quad K_c = 0.0018 \alpha^2. \quad (4.22)$$

Introducing this relation into equation (4.19), the pressure drop over a stenosis for low Reynolds numbers becomes

$$\Delta p_s = K_v(\alpha) R_s q + K_u L_u \frac{\partial q}{\partial t} + K_c R_s(\alpha) \bar{q}. \quad (4.23)$$

Similar to the steady flow situation, at higher Reynolds numbers the pressure drop due to the non-linear term Δp_t can no longer be neglected. The contribution of the non-linear term is now

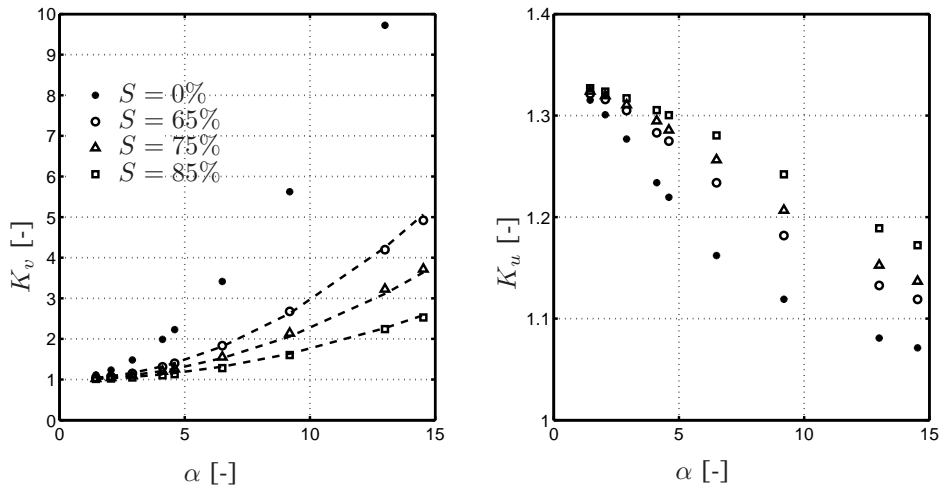


Figure 4.10: The viscous coefficient K_v (left) and the unsteadiness coefficient K_u (right) as a function of the frequency f for stenosis with severities of $S = 0, 65, 75$ and 85% . The dashed lines are based on equation (4.20) and the values for K_u are obtained from equation (4.21).

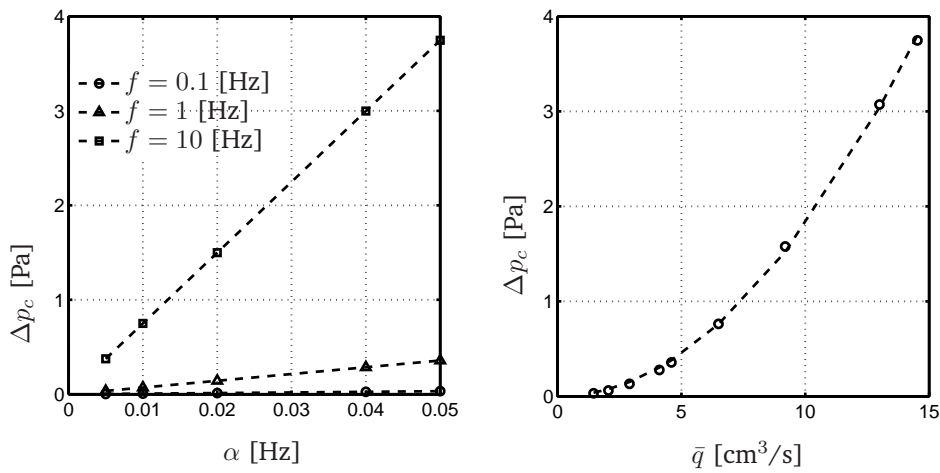


Figure 4.11: (left) the offset K_c as a function of the mean flow \bar{q} for frequencies of $0.1, 1$ and 10 [hz]. The dashed line indicate a linear relation between \bar{q} and K_c . (right) The offset K_c as a function of α for $\bar{q} = 1 \cdot 10^{-6}$ [m^3/s] including a quadratic fit.

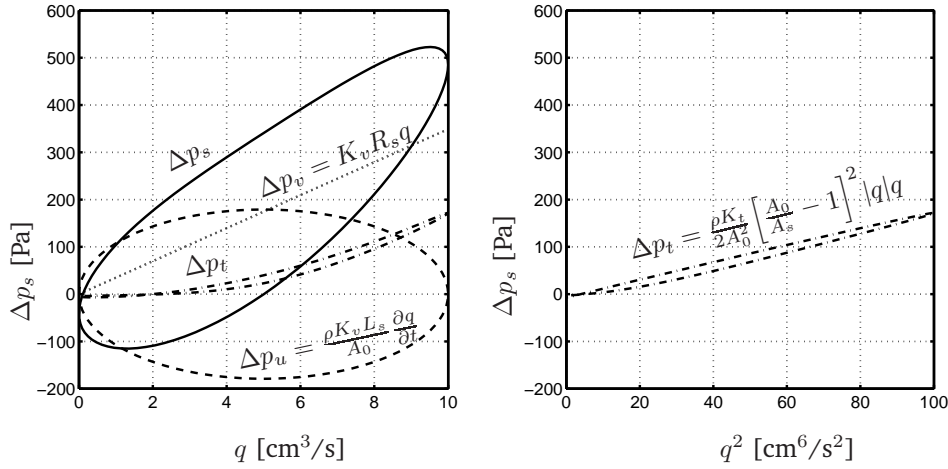


Figure 4.12: On the left, the pressure drop as a function of the flow for $f=1$ [Hz] and $\bar{q} = 5 \cdot 10^{-6}$ [m³/s]. The solid line represents the pressure drop over the 75% stenosis, the dotted line shows the viscous contribution to this pressure drop using the optimised value of I_v and the dashed line shows the unsteadiness contribution. The dash-dot line indicates the remaining pressure drop ($\Delta p_s - \Delta p_v - \Delta p_u$). On the right, this remaining pressure drop Δp_t is shown as a function of the square of the flow which shows an almost linear relation.

estimated by subtracting the known viscous and unsteady part from the pressure drop over the stenosis. The remaining pressure drop Δp_t is shown against the square of the flow in figure 4.12 and an almost linear relation between the two can be established for the case of $f=1$ [Hz] and $\bar{q} = 5 \cdot 10^{-6}$ [m³/s]. This procedure is repeated for all frequencies addressed and for frequencies below $f = 4$ [Hz] a linear relation between the remaining pressure drop and the square of the flow was found. For each severity a slight dependency of K_t on the frequency is observed (figure 4.13). The largest differences, however, occur between the different stenosis severities. Introducing the shape of the stenosis into the expression for the non-linear term, similar as was done for the viscous and unsteadiness term, does not result in a decrease of this severity dependency of K_t . For now, K_t will be assumed constant at the value of $K_t = 0.95$ obtained from the steady flow simulations. For frequencies above $f = 4$ [Hz], no linear relation between Δp_t and q^2 was found. The final relation between the pressure drop as a result of the presence of a stenosis and the flow characteristics is now given by

$$\Delta p_s = K_v(\alpha) R_s q + \frac{\rho K_t}{2 A_0^2} \left[\frac{A_0}{A_s} - 1 \right]^2 |q| q + K_u L_u \frac{\partial q}{\partial t} + K_c(\alpha) R_s \bar{q} \quad (4.24)$$

with

$$K_v = 1 + 0.053 \frac{A_s}{A_0} \alpha^2, \quad K_t = 0.95, \quad K_u = 1.2 \quad \text{and} \quad K_c = 0.0018 \alpha^2. \quad (4.25)$$

In conclusion, expression (4.24) is used to predict the pressure drop over stenoses ($S = 75\%$) when imposing a multi-harmonic flow pulse based on the flow through the femoral artery according to Olufsen and Peskin (2000). The frequency dependent parameters are based on

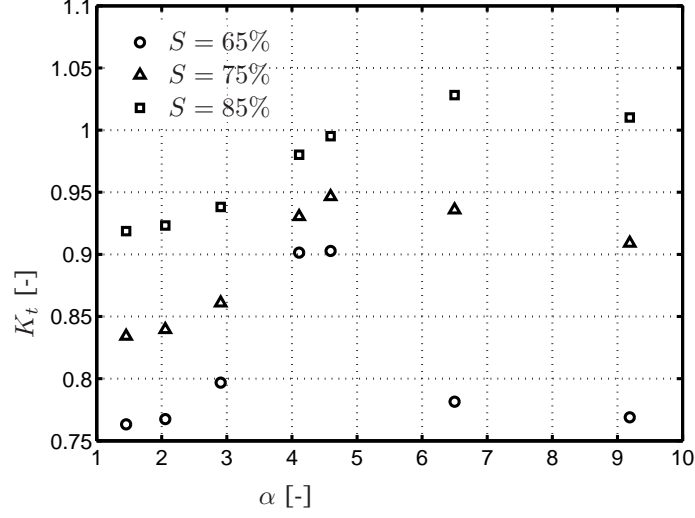


Figure 4.13: Coefficient K_t as a function of α , for stenoses with severities of $S = 65$, 75 and 85% .

the fundamental harmonic of this flow signal, which has a frequency of $f = 1/T = 1$ [Hz]. The resulting pressure drop over each stenosis, computed using equation (4.24) and based on the work by Young and Tsai (1973b), is confronted with the pressure drop obtained from the computational study in figure 4.14 for the stenosis with a length of $L_s = 25a_0$. For the stenoses with a length of $L_s = 5a_0$ and $L_s = 50a_0$, relation (4.24) also shows to be an improvement over the relation found by Young and Tsai (1973b), as demonstrated in figure 4.15.

4.4 Discussion

A finite element method in a rigid 2D axisymmetric domain has been employed to investigate the effect of the presence of a stenosis on the pressure drop over this stenosed vessel. Steady as well as unsteady flow situations with varying frequencies have been simulated over a broad range of Reynolds numbers. Also, several stenosis severities were addressed. For the steady flow simulations, a relation between the pressure drop over the stenosis Δp_s and the flow q was found according to

$$\Delta p_s = R_s q + \frac{\rho K_t}{2A_0^2} \left(\frac{A_0}{A_s} - 1 \right)^2 |q|q \quad (4.26)$$

where, as hypothesised, R_s can be derived analytically by assuming a developed flow situation (Poiseuille profile) at each position across the stenosis. Values of K_t based on the computational model are in the range of $K_t = 0.95 \pm 0.05$ which is in the same range as the values of K_t found by Young and Tsai (1973a) for steady flow over a stenosis. For the oscillatory flow simulation, an extra unsteadiness term and an offset is added to equation 4.26, resulting in a pressure drop over the stenosis according to

$$\Delta p_s = K_v(\alpha) R_s q + \frac{\rho K_t}{2A_0^2} \left(\frac{A_0}{A_s} - 1 \right)^2 |q|q + K_u L_u \frac{\partial q}{\partial t} + K_c(\alpha) R_s \bar{q}, \quad (4.27)$$

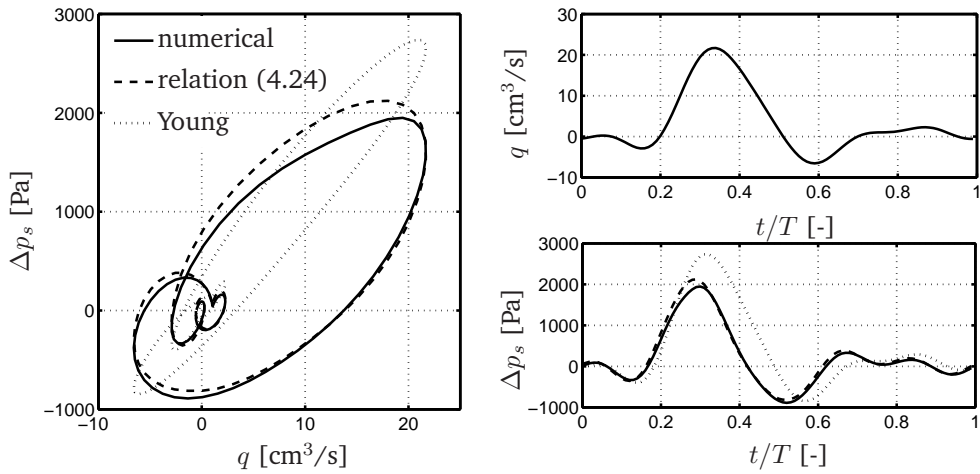


Figure 4.14: The pressure drop over a stenosis ($S = 75\%$) as a function of the flow (left) and as a function of time (right bottom) when imposing a physiological flow signal (right top). The solid line represents the pressure drop as obtained from the computation, the dashed line shows this pressure drop based on our relation and the dotted line shows the pressure drop over the stenosis based on the work of Young.

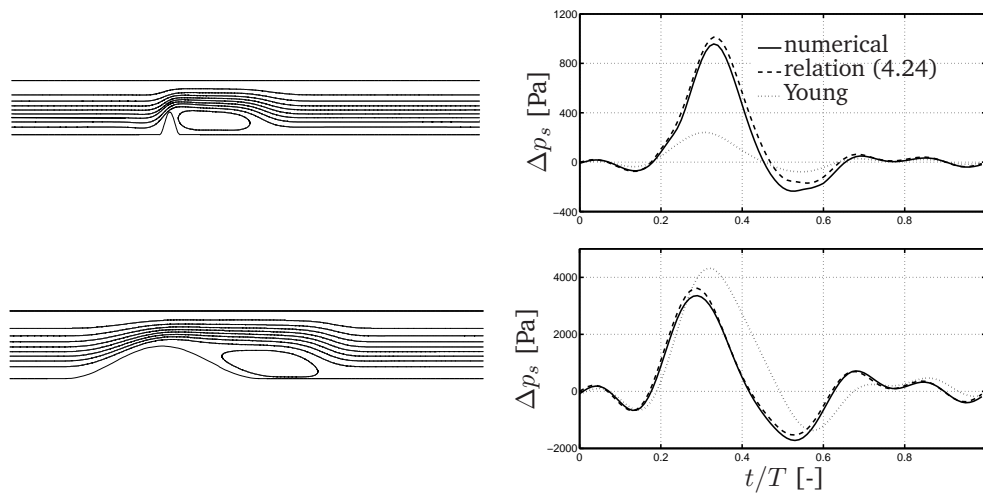


Figure 4.15: On the left the scaled velocity fields at $t = 0.4$ [s] around the stenoses ($S = 75\%$) with a length of $L_s = 5a_0$ (top) and a length of $L_s = 50a_0$ (bottom) when imposing the physiological flow signal from figure 4.14, and on the right the pressure drop over these stenoses as a function of time. The solid line represents the pressure drop obtained from the numerical simulation, the dashed line from our relation and the dotted line from the relation found by Young.

In contrast to the assumption of Young and Tsai (1973b) that the value of K_v remains equal to 1 for unsteady flow situations, here K_v depends on Womersley parameter α . This can be explained by considering flow through a straight vessel, where the friction forces are also a function of the frequency, caused by the changing velocity profiles. The values of the constant K_t obtained from the unsteady flow simulations vary in the same range as they do for steady flow situations, whereas according to Young and Tsai (1973b) this value is altered to $K_t=1.52$ in oscillatory flow through stenoses.

The expression concerning the instationary term is also different from the relation of Young and Tsai (1973b). Although a minor frequency dependency of the unsteadiness coefficient K_u was observed, it can be assumed constant at $K_u = 1.2$ in the physiological range of Womersley numbers. This is similar to the value for K_u found by Young *et al.* Their expression for the contribution of the unsteadiness of the flow to the pressure drop (Δp_u), however, has now changed from

$$\Delta p_u = \frac{K_u \rho L_s}{A_0} \frac{\partial q}{\partial t} \quad (4.28)$$

to

$$\Delta p_u = K_u L_u \frac{\partial q}{\partial t} \quad \text{with} \quad L_u = \int_0^{L_s} \frac{\rho}{\pi a^2(z)} dz, \quad (4.29)$$

and with L_u the local inertance of the stenosis.

The offset $\Delta p_c = K_c(\alpha) R_s \bar{q}$ in equation (4.27) can be explained by flow through a straight tube, where due to a phase shift between the pressure gradient and the flow, a pressure gradient is present when both the flow and the flow change are zero. The magnitude of Δp_c depends on both the Womersley number and the mean flow through the stenosis. For a more detailed description of these dependencies even more simulating can be used with a larger variety of flow signals. The influence of the relation between the mean flow \bar{q} and the maximum of the flow signal on Δp_c should be determined and also flow signals including a negative flow region should be included.

Also, only 1 shape of stenoses is addressed in this work. Although this shape may well represent some of the stenoses present in the human arterial system, other shapes could be investigated as well. The results from the computations with different length of stenoses in a physiological flow situation already show that the model is applicable for stenoses with a large variety of length. Preliminary results on other stenoses shapes indicate that the expression for K_v depends, although not strongly, on the shape of the stenosis.

The pressure drop over the stenosis, when imposing a multi-harmonic physiological flow pulse illustrates an evident improvement in predicting the pressure drop over the stenosis when using frequency dependent parameters for the viscous and unsteadiness term. For this computation, the parameters $K_v(\alpha)$ and $K_c(\alpha)$ are taken from the computations with oscillatory flow of $f=1$ [Hz], based on the fundamental harmonic of the flow signal.

The computational method used to determine the pressure drop over a stenosed vessel provided stable solutions for Reynolds numbers over $Re=700$ for all stenosis severities addressed. The solutions in this range are laminar without instabilities indicating the onset to turbulence. In their work Young and Tsai (1973b), however, observed turbulence at Reynolds numbers below $Re=500$ for all their stenoses. This cannot be described with the finite element method used in this study. Nevertheless, the turbulence term found by Young is unaltered in our relation, indicating that the contribution of this term is not turbulence related but should be interpreted as an expansion term based on Bernoulli's law.

The assumption of an axisymmetrical stenosis geometry falls short of describing the physiological situation. Amongst others, Long et al. (2001) showed that the velocity field near axisymmetrical stenoses are markedly different from those near axisymmetrical stenoses. Seeley and Young (1976) found, however, that for a severity of 90%, the eccentricity of the stenosis lumen did not significantly influence the pressure drop over the stenosis. Because of these findings, and because taking into account asymmetry would significantly increase the number of variables, the influence of the eccentricity on the pressure drop was not investigated.

The pressure drop over the stenosis as investigated in this work, is the absolute value of the pressure drop over the total tube as a result of the stenosed region. This means, as can be observed in figure 4.2, that the pressure drop Δp_s does not necessarily occur at the stenotic site. The local pressure gradient throughout the axial direction of the vessel, however, has not been investigated because we are only interested in the global effect of the presence of a stenosis when modelling the arterial system using a one-dimensional wave propagation method. When implementing a stenosis element into one-dimensional theory, as was done by Rooz et al. (1982); Porenta et al. (1986); Stergiopoulos et al. (1992); Steele et al. (2003) using the relation by Young (1979), a constant pressure gradient is assumed over the length of the stenosis that represents the total pressure drop as a result of the stenosis. This implies that surely an incorrect representation of the pressure just after the stenosis will be obtained. The differential equation describing the pressure drop as a result of the stenosis, based on a linear decay of the pressure within the stenosis region, is given by

$$\frac{\partial q}{\partial t} + \frac{I_v}{I_u}q + \frac{I_t}{I_u}|q|q + \frac{L_s}{I_u}\frac{\partial p}{\partial z} + \frac{I_c}{I_u}\bar{q} = 0 \quad (4.30)$$

with the coefficients I_v , I_t , I_u and I_c defined as

$$I_v = K_v(\alpha)R_s, \quad I_t = \frac{\rho K_t}{2A_0^2} \left[\frac{A_0}{A_s} - 1 \right]^2, \quad I_u = K_u L_u, \quad \text{and} \quad I_c = K_c(\alpha)R_s \quad (4.31)$$

This momentum balance, together with the continuity equation

$$\frac{\partial A}{\partial t} + \frac{\partial q}{\partial z} = 0 \quad (4.32)$$

and a constitutive law, relation the change in cross-sectional area to the change in pressure, yields a set of equations describing the propagation of pressure and flow waves through a stenosis.

In the numerical simulations the blood is modelled to behave purely Newtonian whereas it is known that blood is a shear thinning fluid (Chien and Jan (1973)). Among others, Tu and Deville (1996), Ishikawa et al. (1998) and Mandal (2005) investigated the influence of the non-Newtonian behaviour of blood on the velocity profiles across stenoses. They concluded that at low Reynolds numbers, the choice of the rheological properties of blood significantly affects the flow phenomena and so the pressure drop over the stenosis. So, although the Reynolds numbers in physiological situations in which we are interested is usually high enough for the effect of shear-thinning to be neglected, it may significantly influence the pressure drop over a stenosis in the stagnant period of the flow pulse. More research is needed to quantify this influence of non-Newtonian blood rheology.

The choice of using a rigid domain instead of a more physiological compliant vessel wall, is based on the intention to compare our results to the experimentally obtained data from Young and Tsai (1973a,b), who used solid geometries to mimic the stenoses. Moreover, Moayeri and Zendehebudi (2003) already showed that the influence of the deformability of the vessel wall on the pressure drop over the stenosis is small.

4.5 Conclusion

Based on the results of numerical computations of blood flow through an axisymmetric stenosis, a relation between the pressure drop as a result of the presence of the stenosis and the local flow characteristics is developed. In comparison to the relation presented in Young (1979), now the viscous and unsteadiness contribution to the pressure drop are dependent on the oscillatory behaviour of the flow through the stenosis. When comparing the pressure drop based on the relation from Young to the pressure drop obtained from the numerical simulations, differences of up to 80% can be found, against differences of only about 10% when comparing the pressure drop from our relation to the numerical results.

Chapter 5

The pressure drop over aneurysms under physiological conditions

5.1 Introduction

One-dimensional wave propagation models of fluid flow in distensible tubes may be used to model blood flow through the human arterial system. An appropriate one-dimensional model can provide realistic and clinically relevant information on the pressure and the blood flow through the arterial tree. In the derivation of the one-dimensional balance-of-momentum, however, assumptions are made on the local lumen geometry and the resulting velocity profiles, that may not always hold in patient-specific arterial systems. Primarily, the axial change in lumen radius is assumed to be gradual so that the blood velocity in radial direction of the blood vessel is negligibly small with respect to its axial component. This assumption is used in the derivation of the one-dimensional equations from the fully three-dimensional Navier-Stokes equation, but also in the adoption of a velocity profile function to obtain realistic contributions of the friction and convection forces in the one-dimensional momentum balance (Bessems et al. (2007) and also chapter 2). It may well hold when modelling wave propagation through straight or slightly tapered vessels, but when modelling a patient-specific arterial tree, pathological regions such as stenoses and aneurysms can no longer be realistically modelled using one-dimensional theory. The velocity components in the radial direction are no longer negligibly small with respect to their axial counterpart and the velocity profiles can no longer be based on the theory of fully developed flow in straight vessels. So, to obtain a wave propagation method that is suited to model the propagation of pressure and flow waves travelling through patient-specific arterial systems, one-dimensional models of stenoses and aneurysms are needed. For the equation of mass conservation this means that an appropriate estimate for the local vessel compliance must be obtained by estimating the local lumen radius, the wall thickness and the mechanical properties of the vessel wall. For the equation of momentum balance, a relation between the pressure drop as a result of the presence of a stenosis or an aneurysm and the local flow characteristics must be obtained.

For stenoses, such a relation, based on experimental data, was introduced by Young (1979). In chapter 4 of this thesis, this relation was modified with respect to the dependency on the oscillatory behaviour of the viscous forces, based on the outcome of a computational study in a two-dimensional axisymmetric Navier-Stokes domain. For aneurysms, in the literature a lot of attention has been focussed on the time-dependent velocity field near its cavity (Wille (1981); Perktold (1987); Rathish-Kumar and Naidu (1996); Egelhoff et al. (1999); Finol et al. (2003); Wolters et al. (2005); Deplano et al. (2007)), with a focus on the stresses exerted on the aneurysm wall by the blood. Our interest, however, is mainly on the axial pressure drop as a result of the presence of the aneurysm, regardless of the corresponding velocity field. Although from a fluid dynamical perspective, we expect this pressure drop to be small in comparison to the physiological pressure level, still a detailed description of the pressure drop as a result of a vessel dilation is needed to support this expectation. The axial gradient in the flow $q(z, t)$ through the aneurysm, as a result of the compliance of its wall, is accounted for using the continuity equation in one-dimensional wave propagation.

In this research, a finite element method in a two-dimensional axisymmetric Eulerian domain, similar to the one used in chapter 4, is used to investigate the effect of the presence of an aneurysm on the pressure gradient in an otherwise straight tube. A relation between the flow characteristics and the pressure drop is sought, depending on the severity of the aneurysm. For low Reynolds numbers, we expect that the pressure drop Δp_a over the aneurysm can be predicted by assuming a fully developed flow situation (Poiseuille profiles) throughout the aneurysm, which results in a linear relation between the pressure drop and the flow q . For higher Reynolds numbers, this relation is expected to change. After all, near the wall of the aneurysm cavity, a boundary layer exists with a thickness that changes linearly with the char-

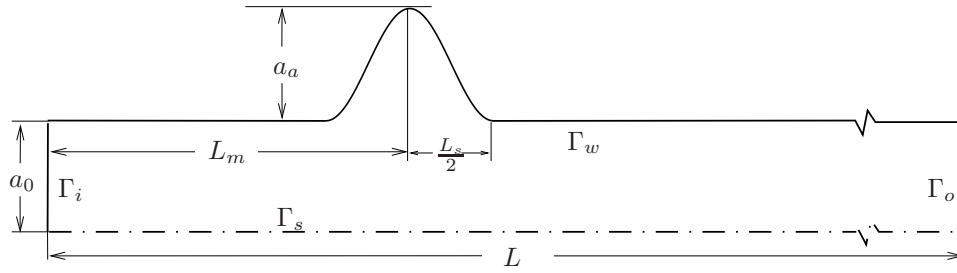


Figure 5.1: Scaled representation of the dilated vessel, indicating its measures and the boundaries used for the computations.

acteristic velocity in the cavity vortex. Because this vortex is driven by the mean flow in the straight part of the vessel and because the wall shear stress depends linearly on the characteristic velocity and on the boundary layer thickness, a quadratic relation between the wall shear stress and the flow is expected. Also, a boundary layer exists distal to the vessel dilation for the velocity profiles to re-develop. The thickness of this boundary layer is also linearly dependent on the characteristic velocity, so again a quadratic relation between the wall shear stress and the flow is expected. Therefore, also the pressure drop Δp_a is expected to depend quadratically on the flow q in the range of Reynolds numbers where a vortex is present in the cavity. For instationary flow, the addition of an extra term that depends on the flow change $\partial q/\partial t$ is expected. Similar to the relation for the pressure drop over a stenosis from chapter 4, we expect the viscous contribution to be dependent on the aneurysm geometry and on the frequency of the oscillatory flow through the aneurysm.

First, a steady flow situation is simulated to obtain a relation between the pressure and the flow at low ($0.2 \leq Re < 10$) and high ($10 \leq Re < 1000$) Reynolds numbers. Next, oscillatory flow of several frequencies is prescribed for low and high Reynolds numbers to quantify the contribution of the unsteadiness of the flow and the frequency dependency of the pressure drop. In conclusion, the relation obtained from these computations is validated by predicting the pressure drop over aneurysms of several different length when prescribing a physiological flow pulse and comparing the outcome to the pressure drop obtained from the numerical computation. The methods used as well as the final relation between the pressure drop and the flow characteristics are discussed.

5.2 Methods

To investigate the pressure drop over an aneurysm a two-dimensional axisymmetric finite element method based on the Navier-Stokes equations in cylindrical coordinates is used, identical to the one used in chapter 4. A representation of the Eulerian grid used is shown in figure 5.1. The radius of the healthy part of the dilated vessel is chosen to be $a_0 = 7 \cdot 10^{-3}$ [m]. The aneurysm geometry is described according to

$$a = a_0 + \frac{1+S}{2} \left[1 - \cos \left(2\pi \frac{z - L_m - L_a/2}{L_a} \right) \right] \quad \text{for } L_m - L_a/2 < z < L_m + L_a/2 \quad (5.1)$$

where S represents the severity of the aneurysm, defined as $S = a_a/a_0 - 1$ with a_a the maximum radius in the centre of the aneurysm. $L_m = 30a_0$ dictates the axial location of this centre

and z is the current axial position. The length of the aneurysm is set at $L_a = 15a_0$ based on a realistic representation of an abdominal aortic aneurysm (AAA). It will not be varied in the derivation of the relation between the pressure drop over the aneurysm and the flow, but it will be introduced as a variable in this relation. The vessel has a total length of $L = 150a_0$ to provide sufficient length distal to the aneurysm for the velocity field to develop. The spatial domain is discretised using 960 bi-quadratic quadrilateral Crouzeix-Raviart elements. In axial direction 120 elements are used, 20 element of which are between $0 \leq z < L_m$ and 100 are elements between $L_m \leq z \leq L$. The mesh is refined towards the aneurysm with a ratio of 1:3 between the length of the elements near the aneurysm and the ends of the fluid domain.

The fluid within the domain is modelled as Newtonian with density $\rho = 1.05 \cdot 10^3$ [kg/m³] and dynamic viscosity $\eta = 5 \cdot 10^{-3}$ [Pa·s]. At the inlet Γ_i a velocity profile is prescribed based on the Womersley solution corresponding to the investigated Womersley parameter α (Womersley (1957)). The vessel wall Γ_w is endowed with no slip conditions and the outlet Γ_o is left stress free. At the axis of symmetry Γ_s the radial velocity is constrained.

$$\begin{cases} v_z & = v_z(\alpha, t, r), & v_r = 0 & \text{at } \Gamma_i \\ v_z & = 0, & v_r = 0 & \text{at } \Gamma_w \\ v_r & = 0 & & \text{at } \Gamma_s \\ \boldsymbol{\sigma} \cdot \mathbf{n} & = 0 & & \text{at } \Gamma_o \end{cases} \quad (5.2)$$

with v_z and v_r the fluid velocities in axial and radial direction respectively, $\boldsymbol{\sigma}$ the Cauchy stress tensor and \mathbf{n} the vector normal to the outflow plane Γ_o . Aneurysms with severities S of 0.1, 0.2, 0.5, 1, 2, 3 and 4 are modelled, resulting in maximum radii of 0.77, 0.84, 1.05, 1.40, 2.10, 2.80 and 3.50 [10^{-2} m]. First, simulations are performed using steady flow conditions at the inlet Γ_i by providing Poiseuille profiles with a flow q of 0.01, 0.02, 0.04, 0.08, 1, 2, 4, 8, 10, 12, 14, 18, 20, 30, 40 and 50 [10^{-6} m³/s]. The corresponding Reynolds numbers Re , according to

$$Re = \frac{2\rho}{\pi\eta a_0} q, \quad (5.3)$$

are in a range of $Re = [0.2 - 1000]$. The results of the computations are divided into 2 regions, i.e. low Reynolds numbers ($0.2 \leq Re < 10$) and high Reynolds numbers ($10 \leq Re \leq 1000$). Next, computations are performed by prescribing oscillatory flow according to

$$q(t) = \bar{q}[1 - \cos(2\pi ft)] \quad (5.4)$$

at the inlet Γ_i , where t is the time and \bar{q} is the time average of the flow. Simulations with frequencies of $f = 0.1, 0.2, 0.4, 0.8, 1, 2, 4, 8$ and 10 [Hz] are performed and for each frequency 5 cycles are simulated, the last of which is monitored. The resulting Womersley parameter α , defined by

$$\alpha = a_0 \sqrt{\frac{2\pi\rho f}{\eta}} \quad (5.5)$$

varies between $\alpha = 2.5$ and $\alpha = 25$. The temporal discretisation Δt for each frequency is $\Delta t = T/(100)$ with T the cycle period of $T = 1/f$. The time-dependent velocity profiles that are prescribed at the inlet Γ_i , corresponding to each frequency, are based on the Womersley solution. For each frequency a broad range of Reynolds numbers ($Re = [0.2 - 1000]$) is again addressed with average flows \bar{q} of 0.005, 0.01, 0.02, 0.04, 0.05, 1, 2, 4, 5, 6, 7, 9, 10, 11, 12, 14 and 15 [10^{-6} m³/s]. A similar division is made into low and high Reynolds numbers.

Finally, a multi-harmonic physiological flow pulse through aneurysms with $S = 2$ is prescribed,

based on the shape of the flow pulse in the abdominal aorta as given by Olufsen and Peskin (2000). The shape of these aneurysms is chosen equal to that of the other simulations but next to the standard length $L_a = 15a_0$ now also length of $L_a = 7.5a_0$ and $L_a = 30a_0$ are chosen to evaluate the influence of this variable representing the length of the aneurysm.

The axial pressure distribution from each computations is obtained by taking the mean of the pressure over the discretised cross-sections. The pressure drop over the aneurysm Δp_a is obtained by subtracting the pressure drop over the straight ('healthy') part of the vessel (which has a length of $L_h = L - L_s$), based on the analytical solution for fully developed flow in a straight pipe by Womersley (1957), from the total pressure drop over the tube. This analytical pressure drop Δp_w can be derived by Womersley's theory using

$$\Delta p_w = Z_L L_h q \quad \text{with} \quad Z_L = 2i\pi f \frac{\rho}{\pi a_0^4} \frac{1}{1 - F_{10}(\alpha)}. \quad (5.6)$$

Here, $F_{10}(\alpha)$ is the Womersley function according to

$$F_{10}(\alpha) = \frac{2J_1(s)}{sJ_0(s)}, \quad \text{with} \quad s = i^{3/2}\alpha \quad (5.7)$$

and J_0 and J_1 are Bessel functions of the first kind of order 0 and 1 (see Abramowitz and Stegun (1964)). For steady flow ($\alpha=0$) this results in

$$\Delta p_w = R_0 \Delta L_h q \quad (5.8)$$

where $R_0 = 8\eta/(\pi a_0^4)$ represents the friction coefficient per unit of length for steady flow in a straight tube. Notice that the pressure drop is defined to be positive when the pressure gradient is negative, e.g. $\Delta p = p(\Gamma_i) - p(\Gamma_o)$.

5.3 Results

At low Reynolds numbers, the pressure gradient in the aneurysm is negligibly small with respect to the pressure gradient in the remainder of the tube, resulting in the plateau in the pressure development as can be seen for an aneurysm with $S = 2$ in figure 5.2. At higher Reynolds numbers, two peaks appear at the entrance (reduced pressure) and the exit of the aneurysm (increased pressure), caused by the sudden expansion and reduction respectively of the lumen's cross-sectional area. Distal to the aneurysm the velocity field slowly (depending on the Reynolds number) recovers to fully developed flow in a straight tube, which is visible in the pressure slowly returning to the pressure obtained from Poiseuille's law (figure 5.2). The streamlines corresponding to the steady flow situation through the aneurysm of $S = 1$, with a flow of $q = 50 \cdot 10^{-6}$ [m³/s] are illustrated in figure 5.3.

When considering steady flow at low Reynolds numbers, local velocity profiles are expected to approach the shape of the velocity profiles for fully developed flow, based on the local lumen radius. This means a linear relation is expected between the pressure drop over the aneurysm and the flow. For each aneurysm severity a linear relation between Δp_a and q is indeed found, according to

$$\Delta p_a = I_v q. \quad (5.9)$$

where I_v (see figure 5.4) corresponds to the analytically derived friction coefficient when assuming a developed flow situation (Poiseuille profile) at each position across the aneurysm,

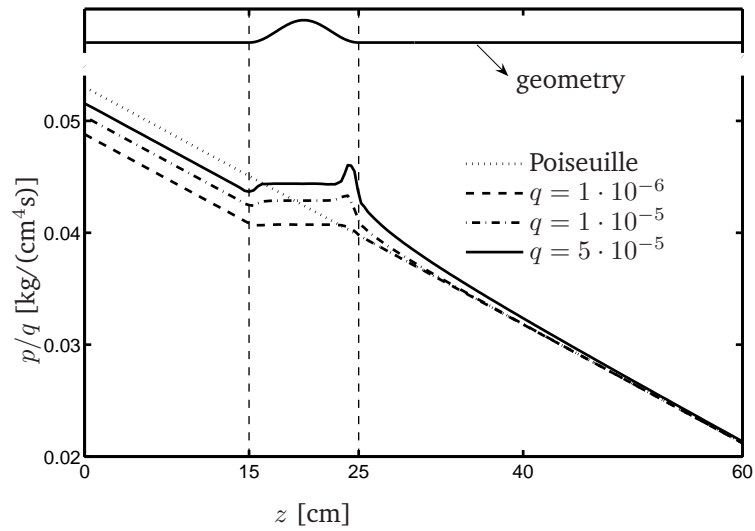


Figure 5.2: The pressure divided by the flow as a function of the axial position in the vessel, obtained from steady flow computations over the aneurysm with $S = 2$ and flows of 1, 10 and 50 [$10^{-6} \text{ m}^3/\text{s}$]. The dotted line shows the pressure based on Poiseuille flow in a straight tube

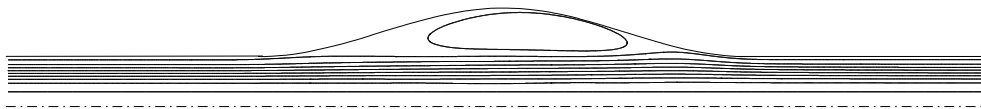


Figure 5.3: The velocity field near the aneurysm ($S = 1$), obtained from the steady flow computation with a flow of $q = 50 \cdot 10^{-6} \text{ [m}^3/\text{s]}$.

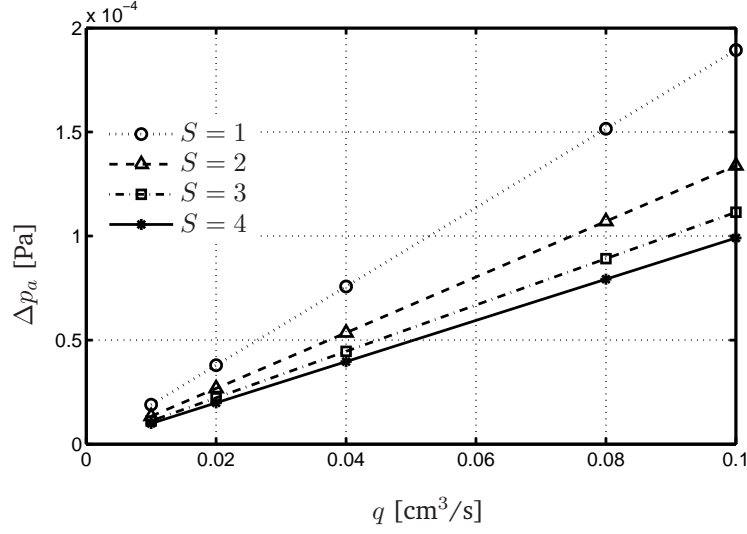


Figure 5.4: the pressure drop as a result of the aneurysm versus the flow, for the steady flow simulations through aneurysms with severities of $S = 1, 2, 3$ and 4 . The dashed lines show linear relations between Δp_a and q according to equation (5.9) with values for I_v as defined by (5.10).

following

$$I_v = R_a = \int_{L_a} R(z) dz = R_0 \int_{L_a} \frac{a_0^4}{a^4(z)} dz \quad \text{with} \quad R_0 = \frac{8\eta}{\pi a_0^4}. \quad (5.10)$$

So, for steady flow at low Reynolds numbers, the pressure drop over an aneurysm can be described as

$$\Delta p_a = R_a q \quad \text{with} \quad R_a = R_0 \int_{L_a} \frac{a_0^4}{a^4(z)} dz. \quad (5.11)$$

When increasing the flow, due to the vortex in the aneurysm sac and the flow development distal to the aneurysm, a quadratic relation between the pressure drop Δp_a and the flow is expected. $\Delta p_a - \Delta p_w$ is shown as a function of q for aneurysms with severities S of 0.1, 0.2, 0.5, 1, 2, 3 and 4 in figure 5.5 where Δp_w is the pressure drop over a length equal to the length of the aneurysm for the case no aneurysm is present ($S = 0$). For small aneurysms ($S < 0.5$) a clear severity dependency of the pressure drop is observed. In this range, even for larger Reynolds numbers, the pressure drop may be approximated by using relation (5.11). For more severe lumen dilations, the influence of the severity on the pressure drop over the aneurysm becomes small, and the differences in the pressure drop between the different aneurysms are negligible with respect to the total pressure drop of each of the aneurysms addressed. Figure 5.5 also indicates that, even for more severe aneurysms, the expected quadratic relation between Δp_a and q is small in comparison to its linear relation. This linear relation, however, is not similar to the linear relation from the computations at low Reynolds numbers. At

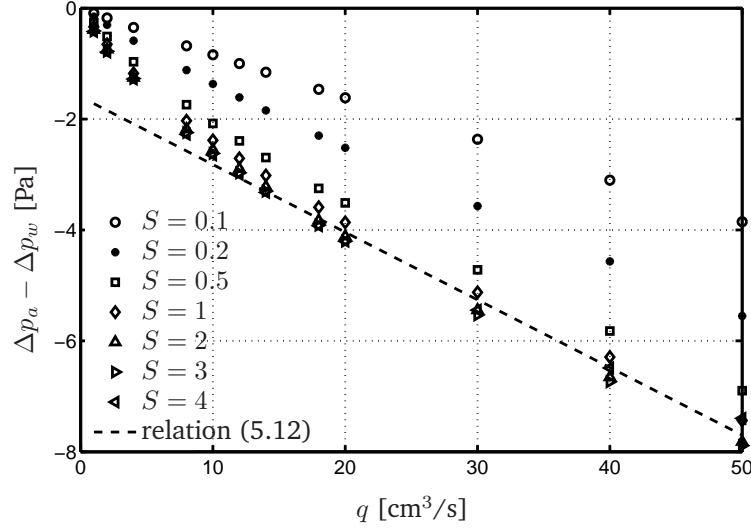


Figure 5.5: The pressure drop ($\Delta p_a - \Delta p_w$) at higher Reynolds numbers as a function of the flow in case of steady flow through aneurysms with severities of $S = 0.1, 0.2, 0.5, 1, 2, 3$ and 4 . The dashed line is described by equation (5.12)

higher Reynolds numbers, the pressure drop over aneurysms with severities of $S \geq 0.5$ can be approximated using

$$\Delta p_a = K_v R_0 L_a q - \Delta p_c \quad \text{with} \quad K_v = 0.75 \quad (5.12)$$

indicated with the dashed line in figure 5.5. Here, $\Delta p_c = 1.0$ [Pa] is the offset at an instantaneous flow of $q = 0$. Equation (5.12) accurately describes Δp_a at higher Reynolds numbers but it obviously falls short, and even gives negative values for Δp_a , in the case of low flow without vortex formation. Since aneurysms develop mainly in larger arteries with moderate to high Reynolds numbers, it is suggested that for steady flow situations the pressure drop over an aneurysm is described using

$$\Delta p_a = 0.75 R_0 L_a q \quad \text{with} \quad R_0 = \frac{8\eta}{\pi a_0^4}. \quad (5.13)$$

Next, time-dependent flow through the locally dilated vessel is investigated to determine the contribution of the unsteadiness term to the pressure drop over the aneurysm. Here, only the results for the aneurysm with severity $S = 2$ are presented, except when mentioned otherwise. The flow signal with a frequency of $f = 1$ [Hz] and $\bar{q} = 5 \cdot 10^{-7}$ [m³/s] is presented as a function of time in figure 5.6, along with the corresponding pressure drop over the aneurysm Δp_a and the pressure drop Δp_w over the length of the aneurysm L_a when no aneurysm is present ($S = 0$). To relate the pressure drop over the aneurysm to the local flow characteristics at low Reynolds numbers, an extra unsteadiness term is introduced into equation (5.11).

$$\Delta p_a = R_a q + I_u \frac{\partial q}{\partial t}, \quad (5.14)$$

with I_u the unsteadiness coefficient. By subtracting the known contribution of the friction

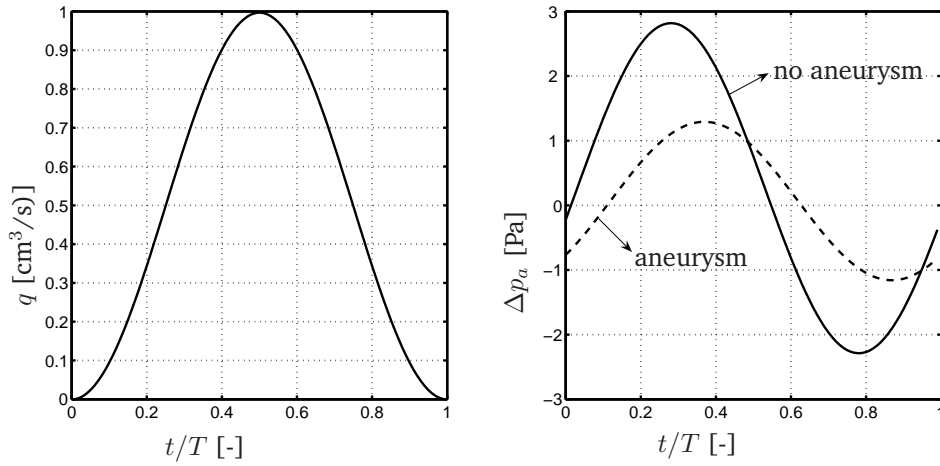


Figure 5.6: The flow (left) and pressure drop (right) as a function of time for oscillatory flow with a frequency of $f = 1$ [Hz] and a mean flow \bar{q} of $5 \cdot 10^{-6}$ [m^3/s]. The dashed line indicates the pressure drop as a results of the aneurysm ($S = 2$) and the solid line shows the pressure drop over a length of L_a when no aneurysm is present.

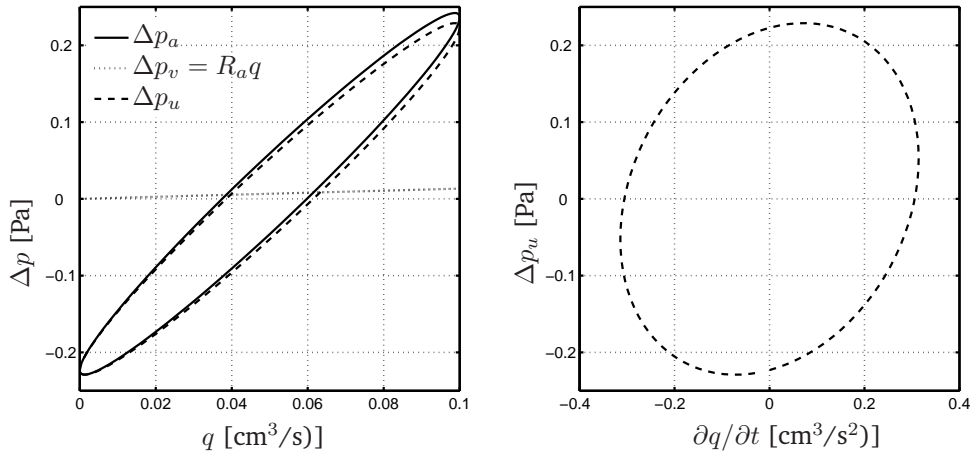


Figure 5.7: (left) The pressure drop as a function of the flow for $f = 1$ [Hz] and $\bar{q} = 5 \cdot 10^{-8}$ [m^3/s]. The solid line represents the pressure drop over the aneurysm ($S = 2$), the dotted line shows the viscous contribution to this pressure drop based on equation (5.11) and the dashed line indicates the remaining pressure drop $\Delta p_u = \Delta p_a - \Delta p_v$. (right) Δp_u as a function of the flow change $\partial q / \partial t$.

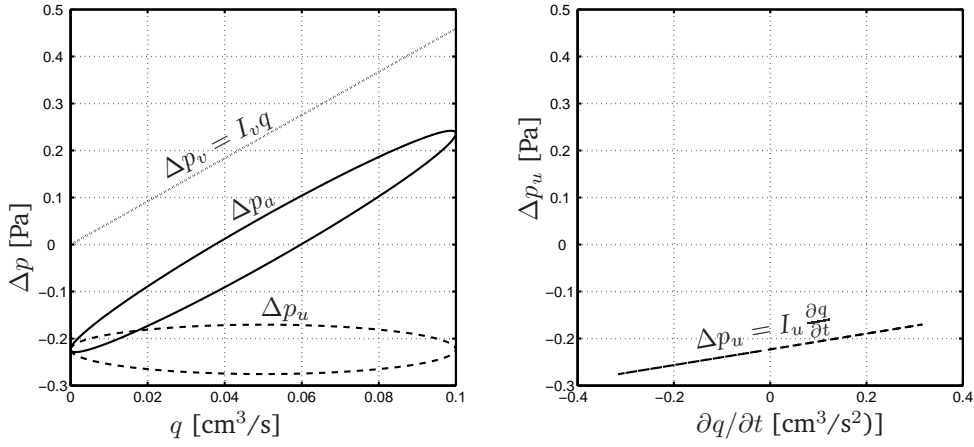


Figure 5.8: The same as figure 5.7 but now the dotted line is based on the adjusted viscous contribution $\Delta p_v = I_v q$ to the pressure drop. The remaining pressure drop Δp_u now shows a linear relation with $\partial q / \partial t$.

term obtained from the steady flow simulations from Δp_a , the pressure drop Δp_u caused by the unsteadiness of the flow remains, as is illustrated in figure 5.7. It also shows Δp_u as a function of $\partial q / \partial t$ and clearly no one-to-one relation between the two is found. By adjusting coefficient R_a , however, a linear relation between Δp_u and $\partial q / \partial t$ can be found as is shown in figure 5.8. Notice that for $\partial q / \partial t = 0$ the value of Δp_u is not equal to zero, so relation (5.14) becomes

$$\Delta p_a = I_v(\alpha)q + I_u(\alpha)\frac{\partial q}{\partial t} + \Delta p_c \quad (5.15)$$

where I_v is no longer equal to R_a but is dependent on the Womersley number. The procedure of optimising I_v to obtain a linear relation between Δp_u and $\partial q / \partial t$ is done for all unsteady computations. Neither the viscous contribution nor the unsteadiness term depend on \bar{q} , but they do change with the frequency. The viscous contribution to the pressure drop shows to be independent of the aneurysm severity (figure 5.9) and can be approximated by

$$I_v = K_v R_0 L_a \quad \text{with} \quad K_v = 0.75 + 0.12\alpha^2 \quad (5.16)$$

as depicted with a dashed line. In the limiting case of $\alpha \rightarrow 0$ for each aneurysm severity the relation between Δp_v and q approaches relation (5.11). For the unsteadiness term, a useful relation between I_u and α over the full range of α cannot be found (figure 5.9) but for larger α 's the constant value of I_u can be approximated using

$$I_u = L_u \quad \text{with} \quad L_u = \frac{\rho}{A_0} \int_{L_a} \frac{a_0^2}{a(z)^2}. \quad (5.17)$$

The offset Δp_c depends on both \bar{q} and the frequency as is shown in figure 5.10 and can be approximated using

$$\Delta p_c = K_c R_0 L_a \bar{q} \quad \text{with} \quad K_c = 0.06\alpha^2 \quad (5.18)$$

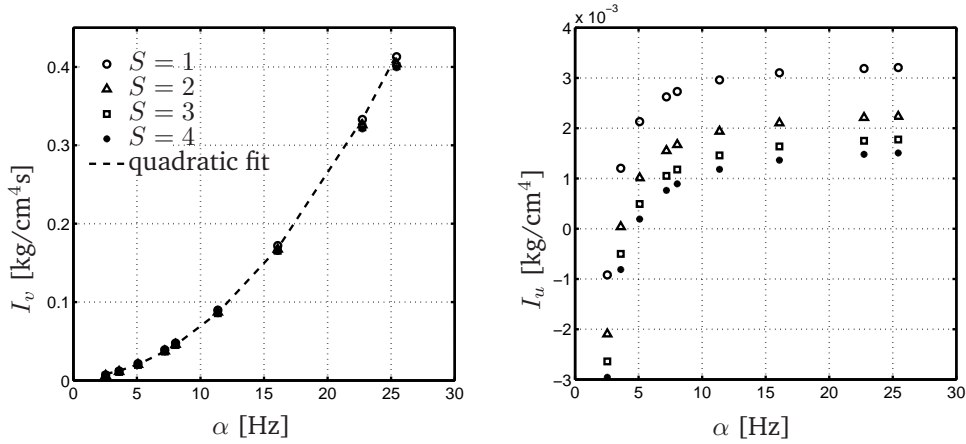


Figure 5.9: The viscous coefficient $I_v = K_v R_0 L_a$ (left) and the unsteadiness coefficient $I_u = L_u$ (right) as a function of α for aneurysms with severities of $S = 1, 2, 3$ and 4. The dashed line is described by equation (5.16)

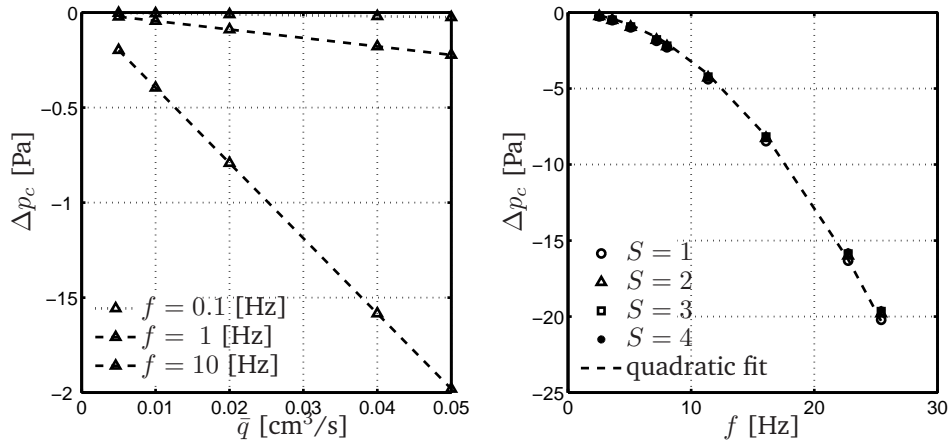


Figure 5.10: (left) the offset Δp_c as a function of the mean flow \bar{q} for frequencies of 0.1, 1 and 10 [hz] in an aneurysm of $S = 2$. The dashed lines indicate a linear relation between \bar{q} and I_c . (right) The offset Δp_c for all severe aneurysms and $\bar{q} = 1 \cdot 10^{-5} \text{ m}^3/\text{s}$ as a function of α , including a quadratic approximation.

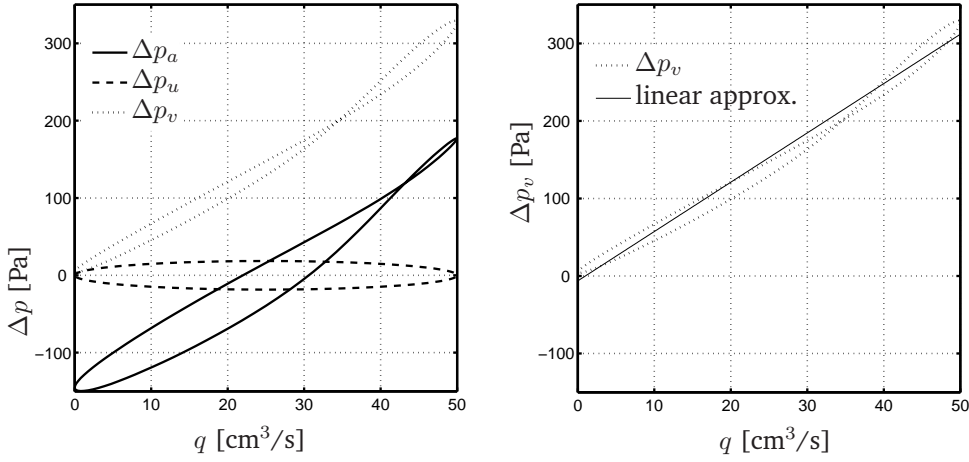


Figure 5.11: (left) The pressure drop as a function of the flow for $f = 1$ [Hz] and $\bar{q} = 5 \cdot 10^{-5}$ [m³/s]. The solid line represents the pressure drop over the aneurysm ($S = 2$) and the dashed line shows the contribution of the unsteadiness term to this pressure drop. The remaining pressure drop ($\Delta p_a - \Delta p_u$) is indicated with the dotted line. (right) The remaining pressure drop Δp_v (dotted) as a function of the flow, along with a linear approximation (solid).

for all aneurysm severities. Equation 5.15 now becomes

$$\Delta p_a = K_v(\alpha)R_0L_aq + L_u \frac{\partial q}{\partial t} + K_c(\alpha)R_0L_a\bar{q}. \quad (5.19)$$

Similar to the steady flow situation, at higher Reynolds numbers a different relation between Δp_a and q is expected. Figure 5.11 shows Δp_a as a function of the flow through the aneurysm ($S = 2$) for the case of $f = 1$ [Hz] and $\bar{q} = 5 \cdot 10^{-5}$ [m³/s]. Because in the case of steady flow a linear relation between the pressure drop and the flow was found, also here a linear relation is expected. The contribution of the unsteadiness term and the offset Δp_c as obtained earlier are subtracted from the pressure drop over the aneurysm to obtain the remaining pressure drop as shown in figure 5.11. Although the relation between this remaining pressure drop Δp_v and the flow is not a purely linear one, for all flow signals addressed, a linear approximation is found that fairly describes the pressure drop over the aneurysm. The values for I_v obtained are independent of \bar{q} but do change with the frequency as is shown in figure 5.12. Again, I_v does not change significantly with the aneurysm severity and again it depends on the Womersley parameter according to equation (5.16) as indicated with the dashed line. The pressure drop in oscillatory flow as a result of the presence of an aneurysm can now be approximated by

$$\Delta p_a = K_v(\alpha)R_0L_aq + L_u \frac{\partial q}{\partial t} + K_c(\alpha)R_0L_a\bar{q}. \quad (5.20)$$

with

$$K_v = 0.75 + 0.12\alpha^2 \quad \text{and} \quad K_c = 0.06\alpha^2 \quad (5.21)$$

Finally, expression (5.20) is used to predict the pressure drop over the aneurysm ($S = 3$) when imposing a multi-harmonic flow pulse based on the flow through the abdominal aorta

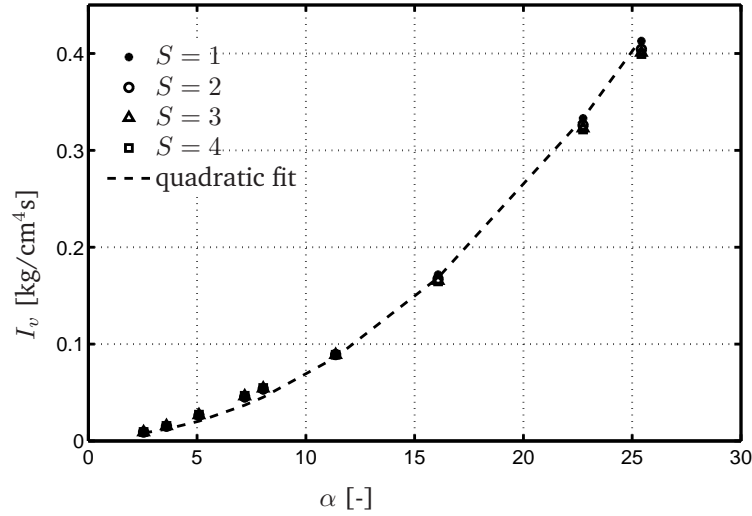


Figure 5.12: (left) The value of the friction coefficient I_v as a function of the Womersley parameter for aneurysms with severities of $S = 1, 2, 3$ and 4 . The dashed line indicates a quadratic fit through these data according to equation (5.16).

according to Olufsen and Peskin (2000). The frequency dependent parameters K_v and K_c are based on the fundamental harmonic of this flow signal, which has a frequency of $f = 1/T = 1$ [Hz]. Figure 5.13 shows the flow signal and the pressure drop over the aneurysm, based on the simulation and computed using equation (5.20) for the aneurysm with a length of $L_a = 15a_0$. For the aneurysms with a length of $L_a = 7.5a_0$ and $L_a = 30a_0$, the pressure drop obtained using relation (5.20) is demonstrated in figure 5.14, along with the pressure drop from the numerical computation.

5.4 Discussion

A finite element method in a rigid two-dimensional axisymmetric domain has been employed to investigate the effect of the presence of an aneurysm on the pressure drop over the dilated vessel. Steady as well as unsteady flow situations with varying frequencies have been simulated over a large range over Reynolds numbers. Also, several aneurysm severities were addressed. From this computational study, a relation between the pressure drop over the aneurysm and the flow was found according to

$$\Delta p_a = K_v(\alpha)R_0L_a q + L_u \frac{\partial q}{\partial t} + K_c(\alpha)R_0L_a \bar{q}, \quad \text{with}$$

$$R_0 = \frac{8\eta}{\pi a_0^4}, \quad L_u = \frac{\rho}{A_0} \int_{L_a} \frac{a_0^2}{a(z)^2}, \quad (5.22)$$

$$K_v = 0.12\alpha^2 + 0.75 \quad \text{and} \quad K_c = 0.06\alpha^2.$$

An important observation is that this relation is independent of the aneurysm severity. When imposing a multi-harmonic physiological flow pulse, the pressure drop as computed by

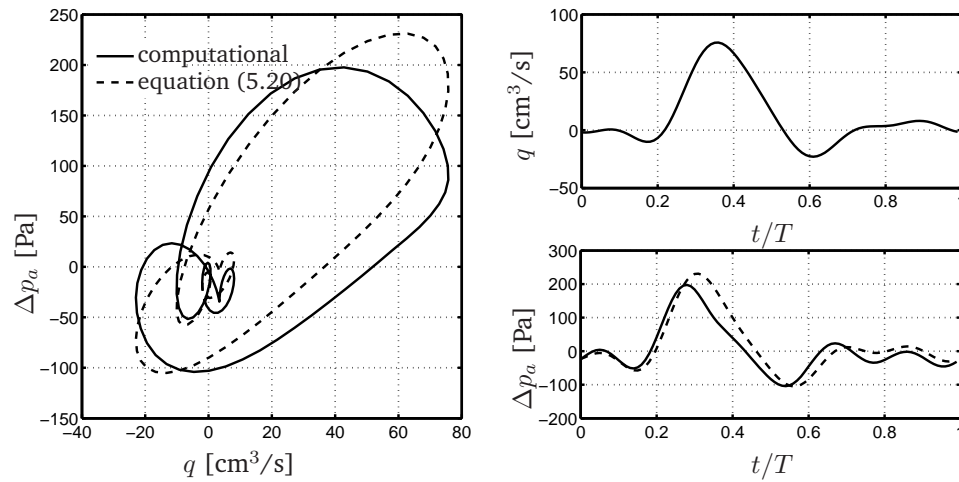


Figure 5.13: The pressure drop Δp_a as a function of the flow (left) and as a function of time (right) when imposing a physiological flow pulse through an aneurysms with severity $S = 3$. The solid line represents Δp_a obtained from the computation and the dashed line is computed by equation (5.20).

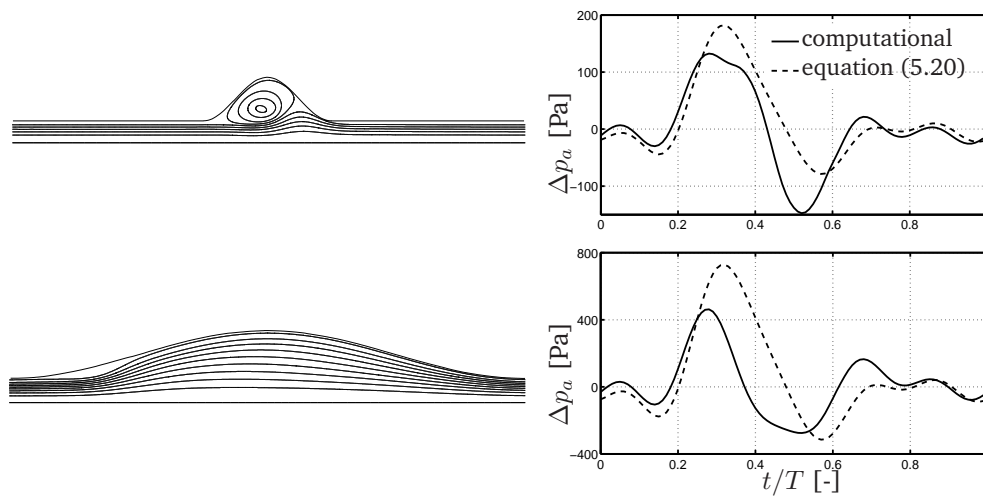


Figure 5.14: On the left the scaled velocity fields at $t = 0.4$ [s] around the aneurysm ($S = 2$) with a length of $L_a = 7.5a_0$ (top) and a length of $L_s = 30a_0$ (bottom) when imposing the physiological flow signal from figure 5.13, and on the right the pressure drop over these aneurysms as a function of time. The solid line represents the pressure drop obtained from the numerical simulation and the dashed line from our relation.

equation (5.22) fairly describes the pressure drop as obtained from the computational method. The coefficients K_v and K_c for this comparison were based on the fundamental harmonic of the flow signal. This illustrates that using equation (5.22), the pressure drop over an aneurysm can be predicted, regardless of the aneurysm severity in the pathological range.

The model of the aneurysm is based on an axisymmetric geometry whereas aneurysms in the abdominal aorta usually dilate in the ventral direction since in the dorsal direction the dilation is limited by the spine. Moreover, the presence of the aortic bifurcation just below the aneurysm is also neglected in the computational model. These geometrical shortcomings will influence the velocity field of the blood through the aneurysm, but a large influence on the pressure drop over the aneurysm is not expected as was also concluded by Finol et al. (2003). The pressure drop over the aneurysm as investigated in this work, is the absolute value of the pressure drop over the total tube as a result of the dilated region. This means that the pressure drop Δp_a does not necessarily occur at the dilation, as can be observed in figure 5.2. The precise pressure decay as a function of the axial position through the vessel, however, has not been investigated because we are only interested in the global effect of the presence of an aneurysm when modelling the arterial system using a 1D wave propagation method. The differential equation describing the pressure drop as a result of the aneurysm, based on a linear decay of the pressure within the aneurysm region, is given by

$$\frac{\partial q}{\partial t} + \frac{I_v}{I_u} q + \frac{L_s}{I_u} \frac{\partial p}{\partial z} + \frac{I_c}{I_u} \bar{q} = 0 \quad (5.23)$$

with the coefficients I_v , I_u and I_c defined by

$$I_v = K_v(\alpha)R_0L_a, \quad I_u = L_u \quad \text{and} \quad I_c = K_c(\alpha)R_0L_a \quad (5.24)$$

This momentum balance, together with the continuity equation

$$\frac{\partial A}{\partial t} + \frac{\partial q}{\partial z} = 0 \quad (5.25)$$

and a constitutive law, defining the compliance of the aneurysm, yields a set of equations describing the propagation of pressure and flow waves through a locally dilated vessel. This does imply, however, that an incorrect representation of the pressure just after the aneurysm will be obtained.

Also, in the aneurysm model the vessel lumen is assumed to contain flowing blood whereas the aneurysm sac is usually partially filled with thrombus. This will influence the velocity field within the aneurysm cavity and so the pressure drop over the aneurysm. For the application of the aneurysm model developed here, the cross-sectional area of the lumen without thrombus should be used. For the estimation of the compliance of the dilated vessel wall, next to the lumen radius, information is needed on the local wall thickness and the effective Young modulus of the vessel wall. In the literature, several studies (e.g. Lanne et al. (1992); Long et al. (2005)) have shown that the increased lumen radius does not necessarily result in an increased local compliance. The decrease in elastin content in the pathological wall results in an increased effective Young modulus and because of arterial wall adaptation the wall thickness is usually higher as well. For an appropriate estimate of the compliance, information on these quantities is needed. For reasons of simplicity, here the arterial wall is assumed to be rigid instead of being a more physiological compliant vessel wall. From Deplano et al. (2007) and Scotti and Finol (2007) we know that taking into account the compliance of the aneurysm significantly changes the velocity field and wall shear stress within the aneurysm. Since the main pressure drop over the aneurysm occurs distal to the aneurysm cavity, however, we believe that this pressure drop will not significantly change when modelling a compliant vessel wall. In the

numerical simulations the blood is modelled as a purely Newtonian fluid whereas it is known that blood is a shear thinning fluid (Chien and Jan (1973)). For blood flow in the abdominal aorta, however, the assumption of Newtonian behaviour is reasonable since the blood viscosity is relatively constant at the high shear rates found in this region (Milnor (1989)).

5.5 Conclusion

Based on the results of numerical computations of blood flow through a two-dimensional axisymmetric aneurysm, a relation between the pressure drop as a result of the presence of this aneurysm and the local flow characteristics is developed. This relation was expected to depend on the aneurysm shape, but for severe aneurysms ($S \geq 1$) the pressure drop no longer changed with increasing aneurysm severity. When comparing the pressure drop based on our relation to the pressure drop obtained from the numerical simulations when prescribing a physiological flow pulse, our relation showed suitable in predicting the pressure drop over a vessel with an aneurysm.

Chapter 6

Application and general discussion

6.1 Introduction

Computational models describing the propagation of pressure and flow waves through patient-specific arterial systems can be an aid in diagnosis and treatment of arterial pathologies. Because of the high computational costs involved in fully three-dimensional fluid structure interaction computations of the total arterial tree, one-dimensional wave propagation models may be more suited to provide clinically relevant information. In chapter 2 (see also Bessems et al. (2007)) a time domain based one-dimensional wave propagation model was described that can accurately predict the propagation of pressure and flow waves through straight or slightly tapered vessels. The velocity profile function used in this model provides first order approximations for the wall shear stress, an important parameter in the development of cardiovascular diseases and in the adaptation process of the vessel wall to changing rheological conditions. In chapter 3 a constitutive law, based on the behaviour of a Kelvin body (standard linear solid model) was developed to model the viscoelastic properties of the arterial wall in one-dimensional wave propagation. These viscoelastic properties may significantly influence the attenuation characteristics of the pressure and flow waves travelling through the arterial system. Since the one-dimensional wave propagation model holds only in straight or slightly tapered vessels, in chapters 4 and 5 additional models were developed for stenoses and for aneurysms. Based on finite element computations in two-dimensional axisymmetrical fluid domains, the pressure drop over rigid stenoses and aneurysms is related to the flow characteristics through these pathologies, as a function of the local vessel geometry. By assuming that this pressure drop occurred by a linear decay of the pressure over the length of the pathological region, a one-dimensional differential equation similar to the one-dimensional momentum balance from chapter 2, was derived.

In this chapter, a one-dimensional wave propagation model of the total arterial system is presented, based on the findings from the previous chapters. Using this model, the influence of the model parameters introduced in these previous chapters are investigated to determine their contribution in the full physiological range. In section 6.2, the various components of the model will be briefly repeated, including the non-linear fluid mechanics, the viscoelastic arterial wall properties and the pathological regions such as stenoses and aneurysms. To connect the models of the individual arterial segments into a model of the arterial tree, in section 6.2 also appropriate boundary and interface conditions will be introduced. Moreover, a synthetic arterial tree, based on the table of Westerhof et al. (1969) is presented and the acquisition of a patient-specific arterial tree based on MR images is briefly presented. Using the synthetic arterial tree, in section 6.3 the effect of some of the model assumptions made in the previous chapters on the wave characteristics will be investigated. The influence of the assumed velocity profile on the pressure and flow waves will be illustrated, the wave attenuation as a result of the constitutive law will be addressed and the influence of the presence of a pathological region on the wave phenomena will be dealt with. Next, the applicability of the model will be demonstrated by showing the resulting pressure and flow obtained from several computations based on the patient-specific arterial tree. Finally, in the general discussion, the methods used and the various results of the present thesis will be discussed, recommendations for future work will be proposed and some possible applications of the developed model will be presented.

6.2 Methods

The propagation of pressure and flow waves through straight or slightly tapered compliant vessels is described using three equations: mass balance, momentum balance and the constitutive

equation for the vessels compliance. From chapter 2 the following set of equations is taken:

$$\begin{cases} \frac{\partial A}{\partial t} + \frac{\partial q}{\partial z} = -\Psi \\ \frac{\partial q}{\partial t} + \frac{\partial}{\partial z} \left(\delta_1 \frac{q^2}{A} \right) + (2 - c_p) \frac{A}{\rho} \frac{\partial p}{\partial z} = Af_z + c_q R_0 q + \frac{\eta}{\rho} \frac{\partial^2 q}{\partial z^2} \\ p(z, t) = \bar{p}(A(z, t); z, t) \end{cases} \quad (6.1)$$

with

$$c_q = \frac{\alpha}{4\sqrt{2}} \left(1 - \frac{\sqrt{2}}{2\alpha} \right)^{-1}, \quad c_p = 1 + \frac{\sqrt{2}}{\alpha} \left(1 - \frac{\sqrt{2}}{2\alpha} \right) \quad \text{for} \quad \alpha > \sqrt{2} \quad (6.2)$$

and

$$c_q = \frac{1}{2}, \quad c_p = \frac{3}{2} \quad \text{for} \quad \alpha \leq \sqrt{2}. \quad (6.3)$$

Here, $q(z, t)$ is the flow, Ψ represents the leakage of fluid per unit of length as a result of side branches, symbol a indicates the local instantaneous lumen radius and with f_z body forces acting on the fluid are included. The blood is modelled as a homogeneous and Newtonian fluid with density ρ and dynamic viscosity η . Furthermore, R_0 is the friction coefficient in a straight pipe according to Poiseuille's law.

$$R_0 = \frac{8\eta}{\pi a^4} \quad (6.4)$$

The parameters c_p , c_q and δ_1 are a function of the Womersley parameter α . A detailed description of these parameters and the derivation of equations (6.1) can be found in chapter 2. The corresponding wall shear stress is written as

$$\tau_w = -\frac{a}{2} \left[c_q R_0 q - (c_p - 1) \frac{\partial p}{\partial z} \right]. \quad (6.5)$$

The constitutive relation is based on thin walled cylinder theory using either linear elastic material properties, or linear viscoelastic material properties. In case of purely elastic material properties, the constitutive relation can be written as

$$\frac{\partial A}{\partial t} = \frac{\partial A}{\partial p} \frac{\partial p}{\partial t} \equiv C_0 \frac{\partial p}{\partial t}, \quad (6.6)$$

with C_0 the compliance per unit of length of the vessel according to

$$C_0 = \frac{2\pi(1 - \mu^2)a_0^3}{hE}. \quad (6.7)$$

Here, h is the wall thickness, μ the Poisson ratio, E represents Young's modulus and a_0 is the lumen radius at $p = p_0$. By a substitution of equation (6.6) into the equation of mass conservation from (6.1), we obtain

$$\begin{cases} C_0 \frac{\partial p}{\partial t} + \frac{\partial q}{\partial z} = -\Psi \\ \frac{\partial q}{\partial t} + \frac{\partial}{\partial z} \left(\delta_1 \frac{q^2}{A} \right) + \frac{A}{\rho} \frac{\partial p}{\partial z} = Af_z + \frac{2\pi a}{\rho} \tau_w + \frac{\eta}{\rho} \frac{\partial^2 q}{\partial z^2} \end{cases} \quad (6.8)$$

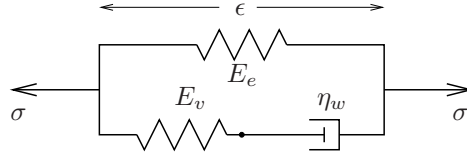


Figure 6.1: Representation of the standard linear solid model used to model the viscoelastic behaviour of the arterial wall in circumferential direction

For the model using viscoelastic material properties, the constitutive relation is based on the viscoelastic behaviour of the standard linear solid model (figure 6.1). The governing differential equation is given by

$$\frac{a}{h}p + \tau_\epsilon \frac{\partial}{\partial t} \left(\frac{a}{h}p \right) = \frac{E_e}{1 - \mu^2} \left(\frac{A - A_0}{2A_0} + \frac{\tau_\sigma}{2A_0} \frac{\partial A}{\partial t} \right) \quad (6.9)$$

with τ_ϵ and τ_σ the relaxation times for constant strain and constant stress respectively, defined as

$$\tau_\epsilon = \frac{\eta_w}{E_v} \quad \text{and} \quad \tau_\sigma = \frac{\eta_w}{E_e} \left(1 + \frac{E_e}{E_v} \right). \quad (6.10)$$

Here E_e is the stiffness of the parallel spring, E_v is the stiffness of the serial spring and η_w is the dashpot's coefficient of viscosity.

6.2.1 Boundary conditions

At the proximal site of the arterial tree, either the pressure $p(t)$ or the flow $q(t)$ can be prescribed, mimicking the behaviour of the heart. In this work, the flow as obtained from Olufsen and Peskin (2000) will be prescribed at the aortic root. A network of vessels is constructed by coupling the individual arterial segments using interface conditions at each bifurcation. As a first condition, conservation of mass can be applied by assuming that there is no fluid leakage at the bifurcations, so the outflow from the parent artery ($_p$) must be equal to the inflow of the 2 child arteries ($_{c_1}$ and $_{c_2}$) added.

$$q_p = q_{c1} + q_{c2} \quad (6.11)$$

Furthermore, we assume that the pressure loss due to vortices and secondary flow patterns created at the bifurcation can be cancelled out by the pressure that is gained by the increase in total cross-sectional area (and so a decrease in the mean velocity) that usually occurs over bifurcations. Therefore, as a second condition we assume pressure continuity at the bifurcation, according to

$$p_p = p_{c1} = p_{c2}, \quad (6.12)$$

When a structure such as the circle of Willis, a collateral network around a stenosis or an artificial bypass occurs in the arterial network, also a merging relation is used according to

$$q_{p1} + q_{p2} = q_c \quad \text{and} \quad p_{p1} = p_{p2} = p_c. \quad (6.13)$$

Now the summed flow of the two joining parent arteries should be equal to the flow in the child artery. At the distal end of each truncated artery a terminal impedance is prescribed

using a three-element Windkessel model, consisting of a resistance R_c in series with a parallel combination of a capacitor C_t and another resistance R_p . In a formula this means

$$\frac{\partial q}{\partial t} = \frac{1}{R_t} \frac{\partial p}{\partial t} + \frac{p}{R_c R_p C_t} - \left(\frac{R_c}{R_p} + 1 \right) \frac{q}{R_c C_t} \quad (6.14)$$

where $R_t = R_c + R_p$ is the total peripheral resistance of the truncated branch. For each terminal branch, the parameters R_c , R_p and C_t must be provided. The characteristic resistance R_c is chosen equal to the characteristic impedance Z_0 of the truncated artery, as

$$R_c \equiv Z_0 = \sqrt{\frac{\rho h E}{2\pi^2(1-\mu^2)a_0^5}} \quad (6.15)$$

to result in minimal reflection at each transition from the 1D to the 0D domain. To determine the total resistances R_t , a division of the flow over the truncated branches must be defined. Here, a flow division proportional to a_0^3 for each truncated artery is assumed, based on the principle of minimum work for quasi-steady flow (see Murray (1926)). The total resistances R_t is then computed by

$$R_t = \frac{\bar{p} a_0^3}{\bar{q} a_t^3} \quad \text{with} \quad a_t^3 = \sum_{i=1}^{N_t} a_{0,i}^3 \quad (6.16)$$

Here, \bar{p} is the mean (over time) systemic pressure, \bar{q} is the mean (over time) flow entering the system through the inlet and N_t is the total number of truncated branches. The terminal compliance C_t for each truncated branch is estimated using

$$C_t = \tau / R_p \quad (6.17)$$

with $\tau = 1.5$ the time constant defining the decay of the pressure signal (see Stergiopoulos et al. (1999)). Values of R_c , R_p and C_t for each truncated branch are listed in table 6.2.

6.2.2 Stenoses and aneurysms

Since blood flow through vessels with sudden changes in cross-sectional area, such as stenoses and aneurysms, does not obey the 1D momentum balance from equation (6.1), two alternative relations are introduced, based on the work in chapters 4 and 5. For a stenosis of length L_s , a relation between the pressure drop and the flow was found according to

$$\Delta p_s = K_v(\alpha) R_s q + \frac{\rho K_t}{2A_0^2} \left(\frac{A_0}{A_s} - 1 \right)^2 |q|q + K_u(\alpha) L_u \frac{\partial q}{\partial t} + K_c(\alpha, \bar{q}). \quad (6.18)$$

Here, A_0 is the cross-sectional area of the vessel proximal to the stenosis and A_s is the cross-sectional area at the neck of the stenosis. Expressions for K_v , K_t , K_u and K_c are empirically determined by means of finite element computations in a 2D axisymmetrical Navier-Stokes domain as presented in chapter 4. Note that this relation is different from the relation by Young (1979) because here the coefficients K_v and K_u are dependent on the fundamental harmonic of the local flow signal and an extra constant $K_c(\alpha, \bar{q})$ is added. Also, the stenosis shape dependency of the viscous and unsteadiness term are not included in K_v and K_u respectively but is expressed by R_s and L_u , according to

$$R_s = \frac{8\eta}{\pi a_0^4} \int_{L_s} \frac{a_0^4}{a_s^4(z)} dz \quad \text{and} \quad L_u = \frac{\rho}{\pi a_0^2} \int_{L_s} \frac{a_0^2}{a_s^2(z)} dz \quad (6.19)$$

where $a_s(z)$ is the local radius of the vessel lumen in the stenosis and a_0 is the radius of the vessel proximal to the stenosis. By assuming that the pressure drop as a result of the stenosis occurs linearly over the length of the stenosis, equation (6.18) can be transformed into the following differential equation:

$$\frac{\partial q}{\partial t} + \frac{K_v R_s}{K_u L_u} q + \frac{\rho K_t}{2A_0^2 K_u L_u} \left(\frac{A_0}{A_s} - 1 \right)^2 q^2 + \frac{L_s}{K_u L_u} \frac{\partial p}{\partial z} + \frac{K_c R_s}{K_u L_u} = 0. \quad (6.20)$$

For the equation of mass conservation, the compliance C_0 per unit of length is based on the assumption that the local Young's modulus does not change with respect to the healthy vessel and the outer radius of the vessel wall is constant.

According to chapter 5 the pressure drop over an aneurysm with a length of L_a can be expressed as

$$\Delta p_a = K_v(\alpha) R_0 L_a q + L_u \frac{\partial q}{\partial t} + K_c(\alpha) R_0 L_a \bar{q} \quad (6.21)$$

Here, the friction coefficient R_0 is based on the radius of the vessel distal to the aneurysm. Equation (6.21) does not include any severity dependency because in chapter 5 we saw that for severe aneurysms (the dilated part has a lumen radius that is at least 1.5 times the radius of the vessel lumen proximal to the aneurysm) the pressure drop over the aneurysm did not depend significantly on its severity. By assuming that the pressure drop over the aneurysm occurs linearly over the length of the aneurysm L_a , equation (6.21) can be transformed into the following differential equation:

$$\frac{\partial q}{\partial t} + \frac{K_v R_0 L_a}{L_u} q + \frac{L_s}{L_u} \frac{\partial p}{\partial z} + \frac{K_c R_0 L_a}{L_u} \bar{q} = 0. \quad (6.22)$$

The estimation of the aneurysm compliance is not straight-forward. Although, according to equation 6.7, the increase of the radius would yield a cubic increase in the compliance, literature shows that the compliance of a dilated vessel is not necessarily different from healthy abdominal arteries (Lanne et al. (1992); Long et al. (2005)). The aneurysm cavity is often filled with thrombus that decreases the lumen radius and increases the wall thickness, thereby reducing the increase of the aneurysm compliance. Moreover, adaptation of the arterial vessel wall can result in a higher effective Young Modulus which also decreases the compliance. Here, we will model the aneurysm compliance to be 1, 5 and 10 times the compliance of the healthy abdominal aorta as computed from table 6.1 using equation (6.7).

6.2.3 Computational Method

A spectral element method is employed to solve the above sets of equations in a (p, q) -formulation and in a (A, q, p) -formulation by a discretisation of the spatial domain using sixth order one-dimensional spectral elements. A Galerkin weighted residuals method is used to transform the set of partial differential equations into a spectral element space as demonstrated in chapter 1. The time derivatives are treated using a second order backward differencing scheme and at each time step $\Delta t = T/1000$ [s] a Newton-Raphson iterative scheme is deployed to handle the non-linear terms. For each computation, ten cardiac cycles are simulated, the last two of which are used for visualisation. The coupling relations at the bifurcations are included by introducing equations (6.11) and (6.12) into the total assembled stiffness matrix. To ensure they are sufficiently accounted for, they should be of similar order of magnitude as the other components in the matrix. Based on estimates of these components in the physiological situation a multiplication factor of $\lambda = 10^4$ is introduced by which equations (6.11) and (6.12) are

multiplied when being inserted into the stiffness matrix. In the range of $\lambda = 10^2$ to $\lambda = 10^6$ identical results are obtained, showing that the solution is insensitive to this parameter.

6.2.4 Physiological data

The system of large arteries is based on the geometrical data from Stergiopoulos et al. (1992), resulting in an arterial network consisting of the 51 arterial segments of table 6.1 as visualised in figure 6.2. This figure also shows that each segment is again divided into a number of elements as given by N in table 6.1. For each segment, a proximal and distal radius (a_p and a_d) is given and within the segment a linear decay of the radius is assumed. The wall thickness h and the elastic Young's modulus E as given in table 6.1 are assumed constant over the segment length. The circled points indicated with characters A through H in figure 6.2 are the monitoring positions used in the next section. The terminal resistances R_c and R_p and compliance C_t , computed as discussed earlier, are listed in table 6.2. For computations using viscoelastic material properties of the vessel wall, the segments of the arterial tree are divided into three groups. The first group exists of the arteries with an elastic modulus of $E = 4 \cdot 10^5$ [Pa] according to table 6.1. These arteries are the most proximal to the heart and the least viscoelastic. Based on data from Learoyd and Taylor (1966) a viscous fraction of $f_v = 0.2$ has been assumed for these arteries. For the standard linear solid model, this viscous fraction is defined as

$$f_v = \frac{(\tau_\sigma - \tau_\epsilon)\omega}{1 + \tau_\sigma\tau_\epsilon\omega^2}. \quad (6.23)$$

where for $\omega = 2\pi f$ a frequency of $f = 1$ [Hz] has been assumed. The arteries with an elastic modulus of $E = 8 \cdot 10^5$ [Pa] according to table 6.1 obtain a viscous fraction of $f_v = 0.4$ and the most distal arteries with $E = 1.6 \cdot 10^6$ [Pa] have an assumed viscous fraction of $f_v = 0.6$. The corresponding values for parameters E_e , E_v and η_w are listed in table 6.3. The Poisson ratio for all computations is set to $\mu = 0.5$ to model incompressible material. The blood is assumed to be a Newtonian fluid with a constant dynamic viscosity of $\eta = 4.5 \cdot 10^{-3}$ [Pa·s] and density $\rho = 1.05 \cdot 10^3$ [kg/m³].

Using the current model of the arterial tree, simulations are performed to demonstrate the influence of the model parameters. First, the influence of the velocity profile function used is demonstrated by performing simulations (referred to as profile) using frictional forces and the non-linear term according to the approximate velocity profile function of chapter 2, according to Poiseuille's law and by assuming frictionless flow (flat profiles). Table 6.4 gives the values of c_p , c_q and δ_1 for each of these cases. Here, parameters $c_p(\alpha)$ and $c_q(\alpha)$ are computed at each cross-sectional area by equations (6.2) and (6.3).

Next, to determine the influence of the viscoelasticity of the arterial wall, in simulations called constitutive both the purely elastic material properties and the material properties based on the standard linear solid model with the model parameters as defined in table 6.3 are used. The influence of the presence of a stenosis in the left femoral artery is illustrated by the simulations referred to as stenosed. Here, a stenosis with varying severities S of 70%, 80% and 90% is added in the third element of this artery. In the simulations aneurysm, a computation with a severe abdominal aortic aneurysm is performed by inserting an aneurysm element into the abdominal aorta part D.

Finally, simulations (referred to as patient) based on a geometry obtained from MR images are performed. To obtain these images, a contrast-enhanced three-station imaging technique called MobiTrak (Busch et al. (1999)) is used. Three individual, partially overlapping volumes are scanned using a Gadolinium-based contrast agent. These three three-dimensional MR images

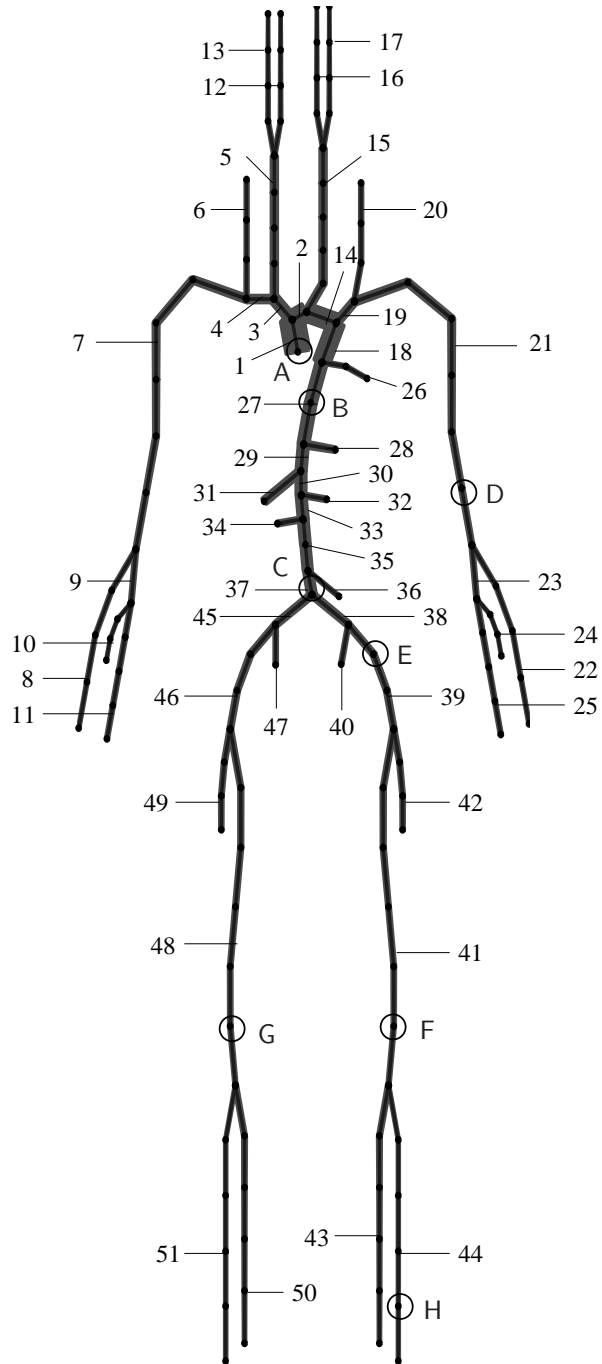


Figure 6.2: Representation of the 51 main arteries in the human arterial system. The numbers correspond to the artery numbers listed in table 6.1 and the characters indicate the monitoring sites for visualising the computational results.

Nr.	artery name	N	L [cm]	a_p [cm]	a_d [cm]	h [10^{-2} mm]	E [10^6 Pa]
1	ascending aorta	1	4.0	1.470	1.440	16.30	0.4
2	aortic arch A	1	2.0	1.120	1.120	12.60	0.4
3	innominate	1	3.4	0.620	0.620	8.00	0.4
4	r. subclavian A	1	3.4	0.423	0.423	6.70	0.4
5	r. carotid	4	17.7	0.370	0.370	6.30	0.4
6	r. vertebral	3	14.8	0.188	0.183	4.50	0.8
7	r. subclavian B	6	42.2	0.403	0.236	6.70	0.4
8	r. radial	4	23.5	0.174	0.142	4.30	0.8
9	r. ulnar A	1	6.7	0.215	0.215	4.60	0.8
10	r. interosseous	3	7.9	0.091	0.091	2.80	1.6
11	r. ulnar B	4	17.1	0.203	0.183	4.60	0.8
12	r. int. carotid	4	17.7	0.177	0.083	4.50	0.8
13	r. ext. carotid	4	17.7	0.177	0.083	4.20	0.8
14	aortic arch B	1	3.9	1.070	1.070	11.50	0.4
15	l. carotid	5	20.8	0.370	0.370	6.30	0.4
16	l. int. carotid	4	17.7	0.177	0.083	4.50	0.8
17	l. ext. carotid	4	17.7	0.177	0.083	4.20	0.8
18	thoracic aorta A	1	5.2	0.999	0.999	11.00	0.4
19	l. subclavian A	1	3.4	0.423	0.423	6.60	0.4
20	l. vertebral	3	14.8	0.188	0.186	4.50	0.8
21	l. subclavian B	6	42.2	0.403	0.236	6.70	0.4
22	l. radial	4	23.5	0.174	0.142	4.30	0.8
23	l. ulnar A	1	6.7	0.215	0.215	4.60	0.8
24	l. interosseous	3	7.9	0.091	0.091	2.80	1.6
25	l. ulnar B	4	17.1	0.203	0.183	4.60	0.8
26	intercostals	2	8.0	0.200	0.150	4.90	0.4
27	thoracic aorta B	2	10.4	0.675	0.645	10.00	0.4
28	celiac	1	1.0	0.300	0.300	6.40	0.4
29	abdom. aorta A	1	5.3	0.610	0.610	9.00	0.4
30	abdom. aorta B	1	1.0	0.600	0.600	8.00	0.4
31	sup. mesenteric	1	5.9	0.435	0.435	6.90	0.4
32	l. renal	1	3.2	0.260	0.260	5.30	0.4
33	abdom. aorta C	1	1.0	0.590	0.590	8.00	0.4
34	r. renal	1	3.2	0.260	0.260	5.30	0.4
35	abdom. aorta D	2	10.6	0.580	0.548	7.50	0.4
36	inf. mesenteric	1	5.0	0.160	0.160	4.30	0.4
37	abdom. aorta E	1	1.0	0.520	0.520	6.50	0.4
38	l. common iliac	1	5.8	0.368	0.350	6.00	0.4
39	l. ext. iliac	3	14.4	0.320	0.270	5.30	0.8
40	l. int. iliac	1	5.0	0.200	0.200	4.00	1.6
41	l. femoral	6	44.3	0.259	0.190	5.00	0.8
42	l. deep femoral	3	12.6	0.255	0.186	4.70	0.8
43	l. post. tibial	5	32.1	0.247	0.141	4.50	1.6
44	l. ant. tibial	5	34.3	0.130	0.130	3.90	1.6
45	r. common iliac	1	5.8	0.368	0.350	6.00	0.4
46	r. ext. iliac	3	14.4	0.320	0.270	5.30	0.8
47	r. int. iliac	1	5.0	0.200	0.200	4.00	1.6
48	r. femoral	6	44.3	0.259	0.190	5.00	0.8
49	r. deep femoral	3	12.6	0.255	0.186	4.70	0.8
50	r. post. tibial	5	32.1	0.247	0.141	4.50	1.6
51	r. ant. tibial	5	34.3	0.130	0.130	3.90	1.6

Table 6.1: physiological and geometrical data of the arterial tree base on Stergiopoulos et al. (1992).

Nr.	artery name	R_c [kg cm ⁻⁴ s ⁻¹]	R_p [kg cm ⁻⁴ s ⁻¹]	C_t [10 ⁻³ cm ⁴ s ² kg ⁻¹]
6	r. vertebral	11.2	25.5	58.7
8	r. radial	20.6	58.0	25.9
10	r. interosseous	71.4	227.0	6.6
11	r. ulnar B	11.3	25.4	59.0
12	r. int. carotid	80.5	313.0	4.8
13	r. ext. carotid	77.8	315.0	4.8
16	l. int. carotid	80.5	313.0	4.8
17	l. ext. carotid	77.8	315.0	4.8
20	l. vertebral	11.2	25.5	58.7
22	l. radial	20.6	58.0	25.9
24	l. interosseous	71.4	227.0	6.6
25	l. ulnar B	11.3	25.4	59.0
26	intercostals	13.5	53.1	28.3
28	celiac	2.7	5.6	268.0
31	sup. mesenteric	11.2	1.6	931.0
32	l. renal	3.6	9.2	162.0
34	r. renal	3.6	9.2	162.0
36	inf. mesenteric	10.8	44.1	34.0
40	l. int. iliac	11.9	16.2	92.6
42	l. deep femoral	10.9	24.0	62.5
43	l. post. tibial	30.3	49.9	30.0
44	l. ant. tibial	34.5	67.8	22.1
47	r. int. iliac	11.9	16.2	92.6
49	r. deep femoral	10.9	24.0	62.5
50	r. post. tibial	30.3	49.9	30.0
51	r. ant. tibial	34.5	67.8	22.1

Table 6.2: parameters used for the Windkessel models.

E 10 ⁶ [Pa]	f_v [-]	E_e 10 ⁶ [Pa]	E_v 10 ⁶ [Pa]	η_w 10 ⁶ [Pa]
0.4	0.2	0.4	0.2	2.5
0.8	0.4	0.8	0.9	1.0
1.6	0.6	1.6	3.4	3.0

Table 6.3: parameters used for the standard linear solid model, depending on the elastic modulus E according to table 6.1.

velocity profile	c_p	c_q	δ_1
$v_z(\alpha, z, t)$	$c_p(\alpha)$	$c_q(\alpha)$	$\delta_1(\alpha)$
Poiseuille	1	1	4/3
no friction	1	0	1

Table 6.4: values for c_p , c_q and δ_1 for each assumed velocity profile.

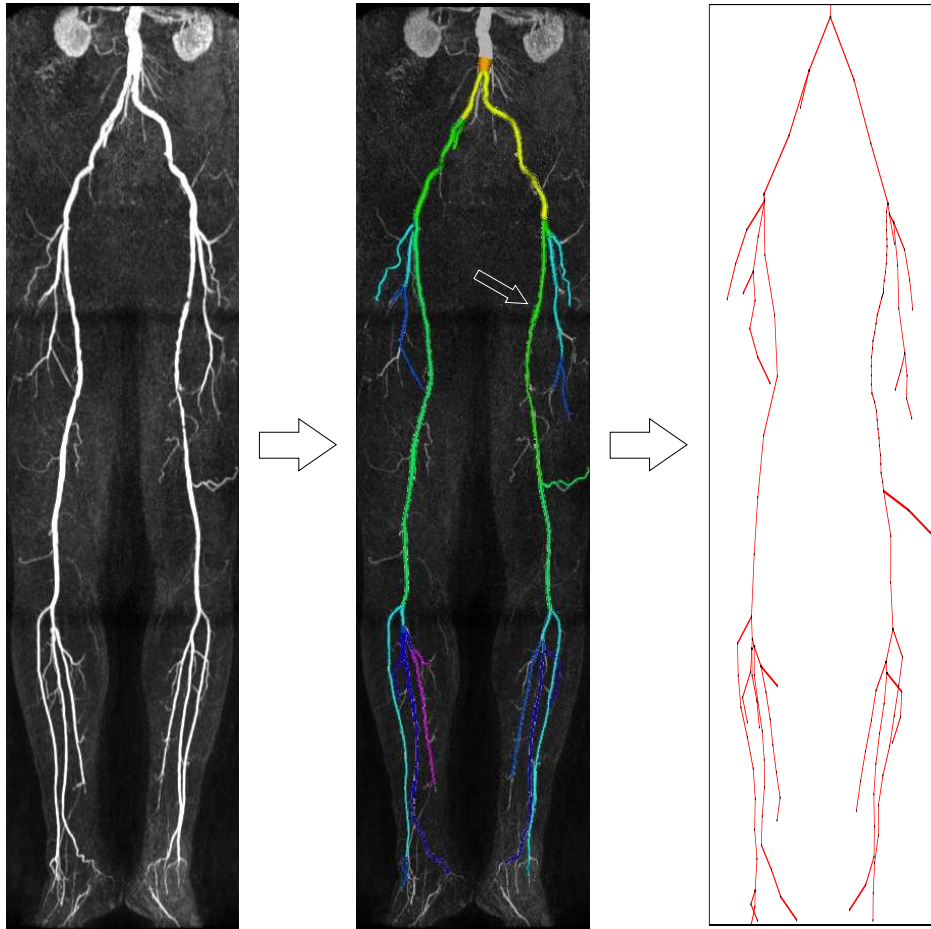


Figure 6.3: (left) Three-station MR image of the lower extremities, by Philips Medical Systems (PMS, Best, The Netherlands). (centre) The same MR image now including the segmented arteries, where the colours represent the segments generation (by PMS). (right) Mapping of this segmentation into a one-dimensional mesh. Here, the angles between the individual segments are purely illustrative.

are then merged into one image set (left of figure 6.3) and by selecting a starting point just above the aortic bifurcation, an automatic vessel-tree tracking algorithm (Bülow et al. (2004)) is initiated to find the centerline of the vessels tree in both legs. The local vessel lumen radius a_0 is automatically detected using the full-width-half-maximum of the lumen intensity as a threshold to obtain a segmentation as shown in the centre of figure 6.3. In the translation of the current segmentation into one-dimensional finite elements, for each individual segment a mean element length L_m is defined, based on the mean radius a_m of the segments lumen. In this case a relation of $L_m = 30a_m$ is chosen, resulting in 150 elements for the total mesh. The radius of the individual elements is then based on a quadratic fit through the radius of each segment. Since the vessel wall cannot be determined from the images obtained, it is assumed to have a local thickness of $h = 0.125a_0$ [m] and a constant Young modulus of $E = 1.00 \cdot 10^6$ [Pa], roughly based on the physiological data of table 6.1.

The segment representing the left femoral artery as indicated in figure 6.3 is clearly narrowed at the indicated location so at this position a stenosis element is used defined by equation (6.20). Next, four computations are executed. The first with the stenotic region intact, the second after balloon angioplasty of this stenosis, a third where also the remainder of this segment is repaired by balloon angioplasty and finally a computation is performed where the total pathological region of this vessel is bypassed using a vessel with a lumen radius of $a_0 = 2.0$ [mm], a wall thickness of $h = 0.25$ [mm] and a Young modulus of $E = 1 \cdot 10^6$ [Pa].

6.3 Results

For each computation based on the geometric data from table 6.1, the pressure and flow at positions A through H as indicated in figure 6.2 are monitored. Figures 6.4 and 6.5 show the pressure and the flow respectively at positions A, B, C, D, F and H for the profile computations without pathological regions, using linear elastic wall behaviour for the three velocity profile functions discussed earlier. Figure 6.5A confirms that, when assuming a flat frictionless velocity profile, the total pressure drop over the arterial tree is the least, since both the contribution of the non-linear term (δ_1) and the friction term is smaller than they are for the other two assumed velocity profiles. It also shows that the differences between the use of the approximate velocity profiles function and Poiseuille profiles are only minor. In the region of the arterial tree where the frictional forces are dominantly present, the approximate velocity profile function approaches Poiseuille profiles, whereas in the inertia dominated regions, where the approximate profiles are more flat, frictional forces no longer significantly influence the pressure and flow waves. Figure 6.6 shows the wall shear stress τ_w as a function of time at positions A, B, C, D, F and H for the Poiseuille based velocity profiles and the velocity profiles based on the approximate velocity profile function. It shows that the assumption of Poiseuille profiles in the larger arteries provides an under-estimation of the wall shear stress at peak systole. In the smaller arteries, this under-estimation becomes less profound. Also, the time averaged wall shear stress obtained from the approximate velocity profile function is of the same order of magnitude throughout the arterial system, whereas for Poiseuille profiles it increases towards the distal ends.

Figures 6.7 and 6.8 show the pressure and the flow for the constitutive computations with linear elastic and viscoelastic properties of the arterial wall. The model using viscoelastic wall properties clearly shows a higher attenuation of the pressure and flow waves travelling through the arterial system. The increased pressure in the systolic phase in the aorta (A through C) of the model using viscoelastic wall properties is caused by the increase in the effective Young's modulus using this model. This increase also results in an increased wave speed throughout

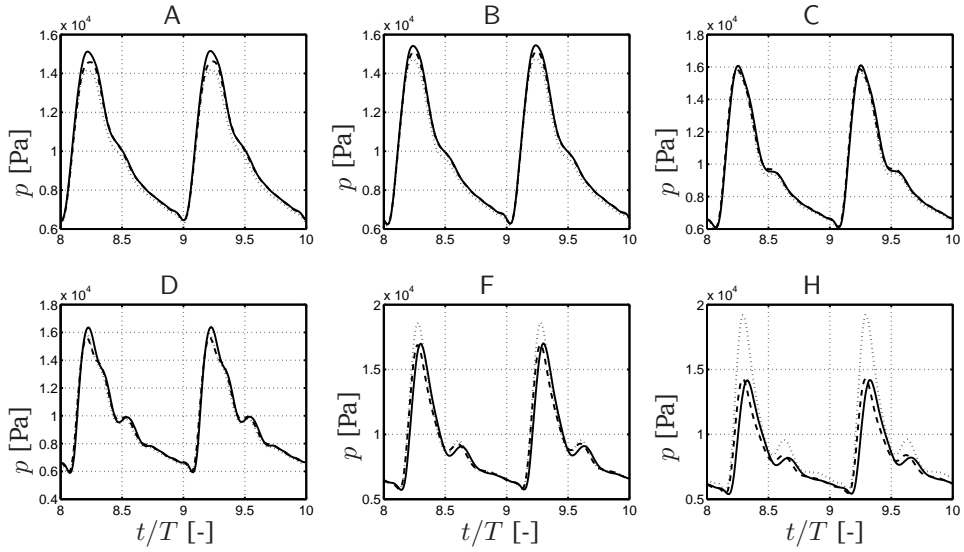


Figure 6.4: The pressure as a function of time, monitored at positions A, B, C, D, F and H of simulations profile. The solid line is obtained by using the approximate velocity profile function, the dashed line is based on the assumption of Poiseuille profiles and the dotted line indicates the pressure when assuming frictionless fluid flow.

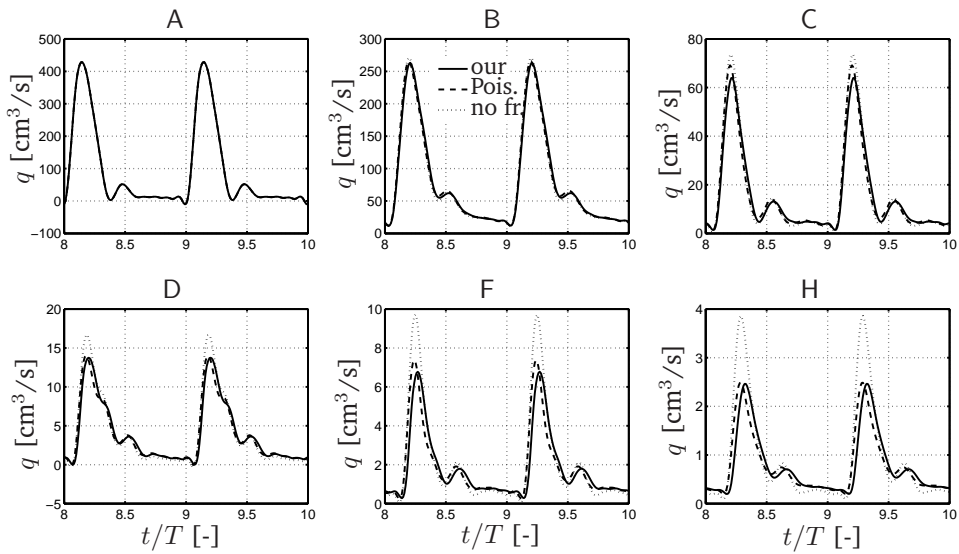


Figure 6.5: The same as figure 6.4, but now the flow as a function of time is shown.

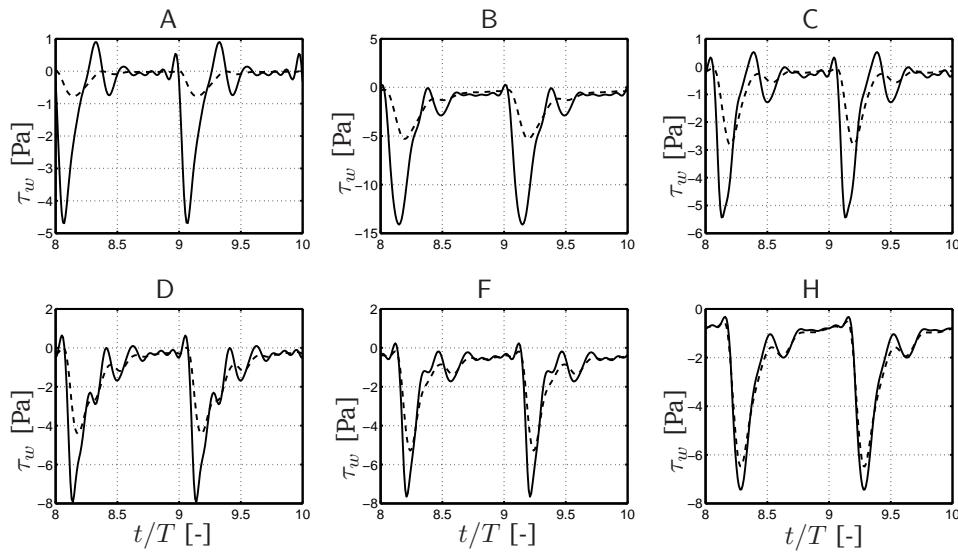


Figure 6.6: The wall shear stress as a function of time, monitored at positions A, B, C, D, F and H, obtained from the profile simulations. The solid line is obtained by using the approximate velocity profile function and the dashed line is based on the assumption of Poiseuille profiles.

the arterial tree, as can be seen by the phase lag of the pressure and flow pulses in points F and H.

Next, the influence of the presence of a stenosis based on the stenosed simulations is demonstrated. Figures 6.9 and 6.10 show the pressure and the flow respectively at positions A, B, C, E, F and G obtained from computations with stenoses of 70, 80 and 90% in the femoral artery. Clearly, the presence of such stenosis lowers the perfusion of the organs distal to the pathological region. The results of the 70% stenosed artery shows only a small decrease in flow distal to the pathological region, whereas the 90% stenosis severely lowers the perfusion of the peripheral beds. In the remainder of the arterial system, hardly any influence of the stenosis is observed.

The influence of a severe abdominal aortic aneurysm as computed with the aneurysm simulations is shown in figures 6.11 and 6.12. When modelling the compliance of the aneurysm to be equal to the vessel compliance without an aneurysm, no significant differences can be detected between the results with and without an aneurysm in the abdominal aorta. Apparently, the influence of the pressure drop over the aneurysm as described by equation 6.21 is small with respect to the physiological pressure pulse. Increasing the aneurysms compliance as a result of the increased lumen radius, results in a reflection of part of the systolic pressure wave, which significantly changes the wave characteristics throughout the arterial system.

The pressure and flow resulting from the patient computations on the patient-specific arterial tree obtained from MR images are presented in figures 6.13 and 6.14. In the atherosclerotic femoral artery, a clear pressure drop with respect to the unobstructed femoral artery is shown, together with a significant decrease in blood flow through the obstructed vessel. By repairing the proximal stenosis, indicated with S1 in the MR image, a slight improvement of the blood flow through this segment is achieved, but only angioplasty of the distal narrowing (S2) results

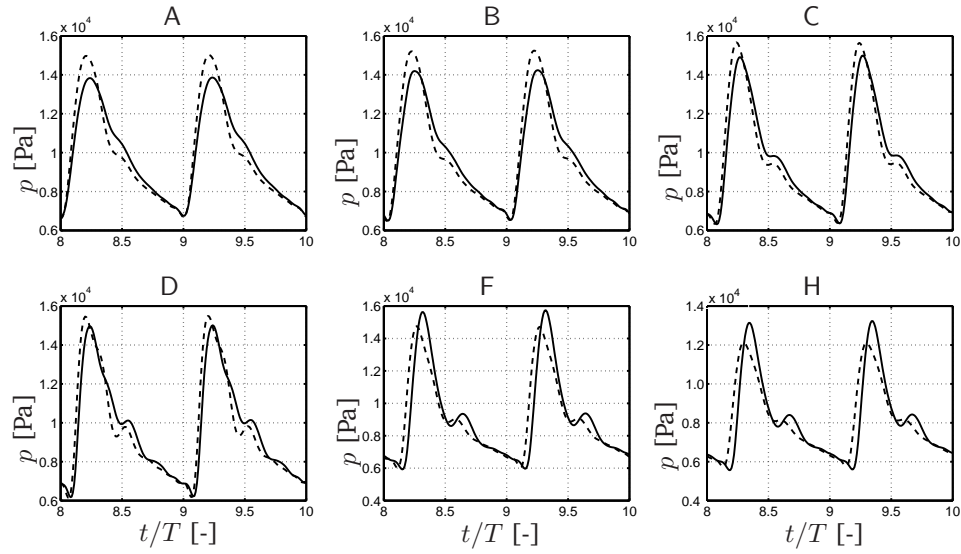


Figure 6.7: The pressure as a function of time, monitored at positions A, B, C, D, F and H obtained from the constitutive simulations. The solid line is obtained from computations using linear elastic arterial wall behaviour and the dashed line is based on the computations with viscoelastic wall properties.

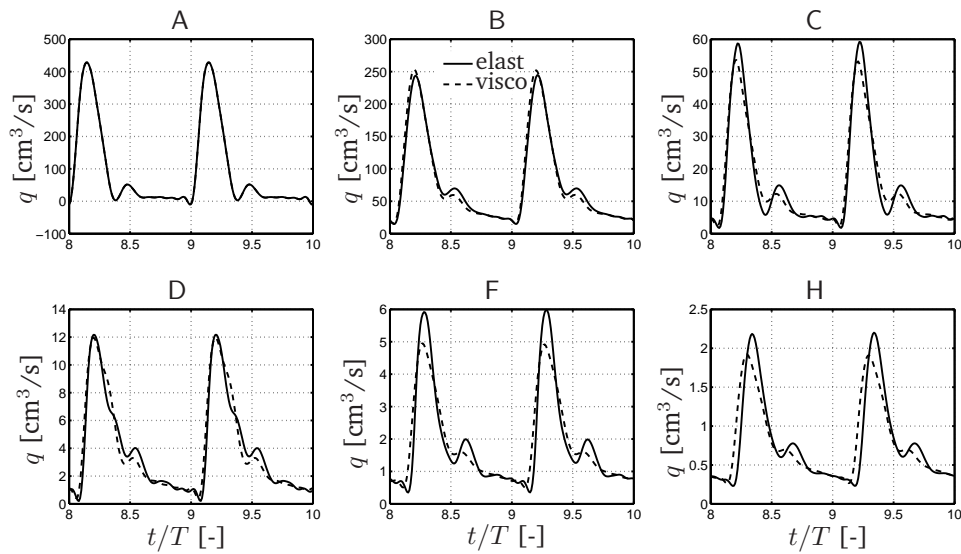


Figure 6.8: The same as figure 6.7 but now the flow is shown.

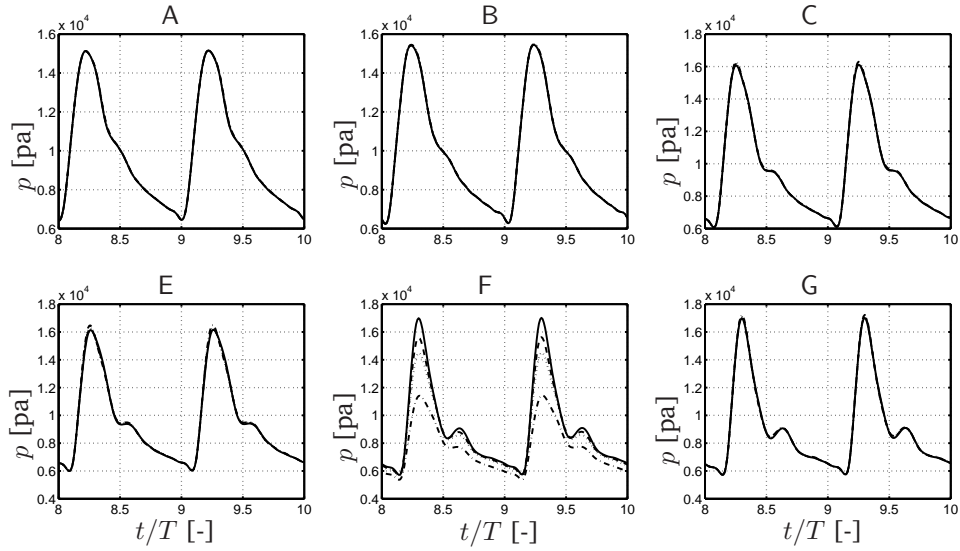


Figure 6.9: The pressure as a function of time, monitored at positions A, B, C, E, F and G as obtained from the stenosed simulations where a stenosis of 0 (solid line), 70 (dashed line), 80 (dotted line) and 90% (dash-dotted line) is present in the 3rd element of the left a. femoralis.

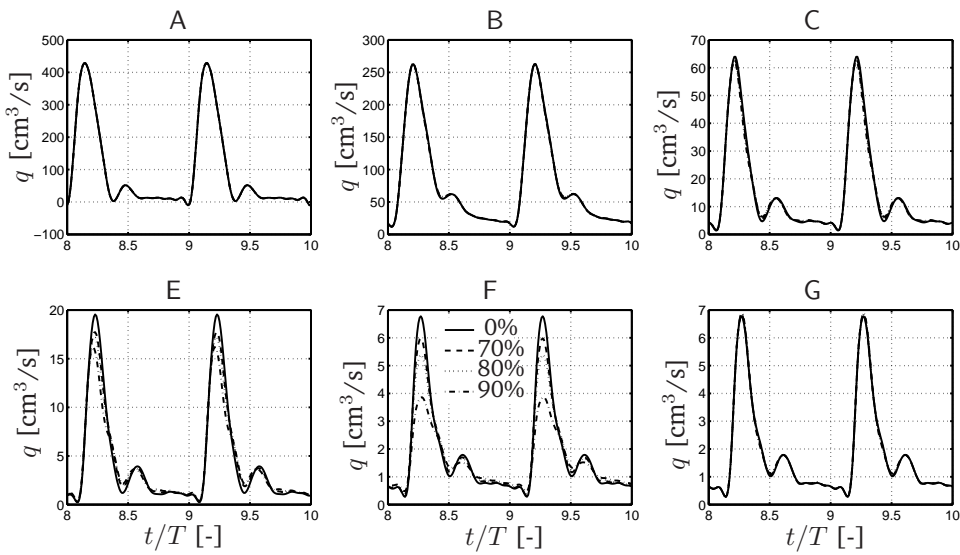


Figure 6.10: The same as figure 6.9, but now the flow as a function of time is depicted.

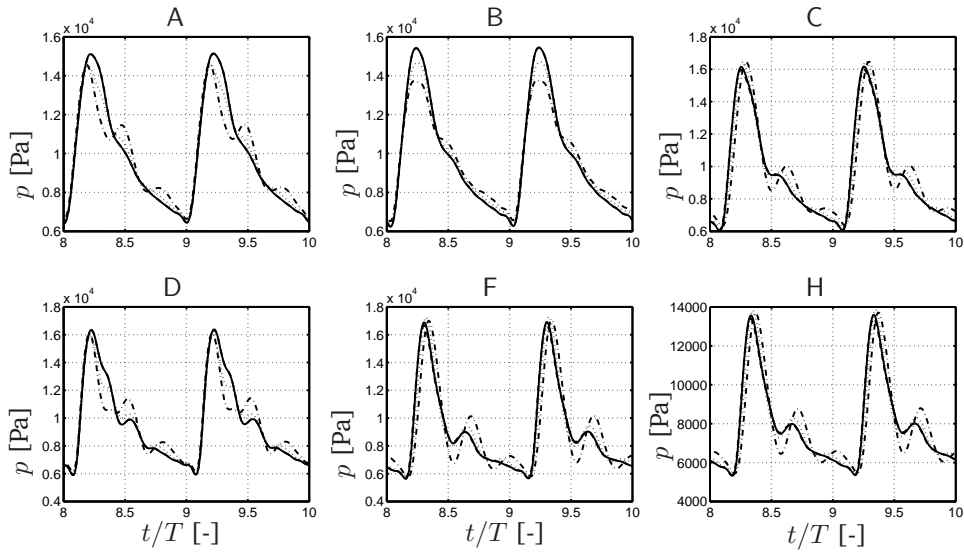


Figure 6.11: The pressure as a function of time, monitored at positions A, B, C, D, F and H as obtained from the aneurysm simulations with an aneurysm present in the abdominal aorta part D. Results are shown of simulations without an aneurysm (solid line) and with an aneurysm where the compliance is 1 (dashed line), 5 (dotted line) and 10 (dash-dotted line) times the compliance of situation without an aneurysm.

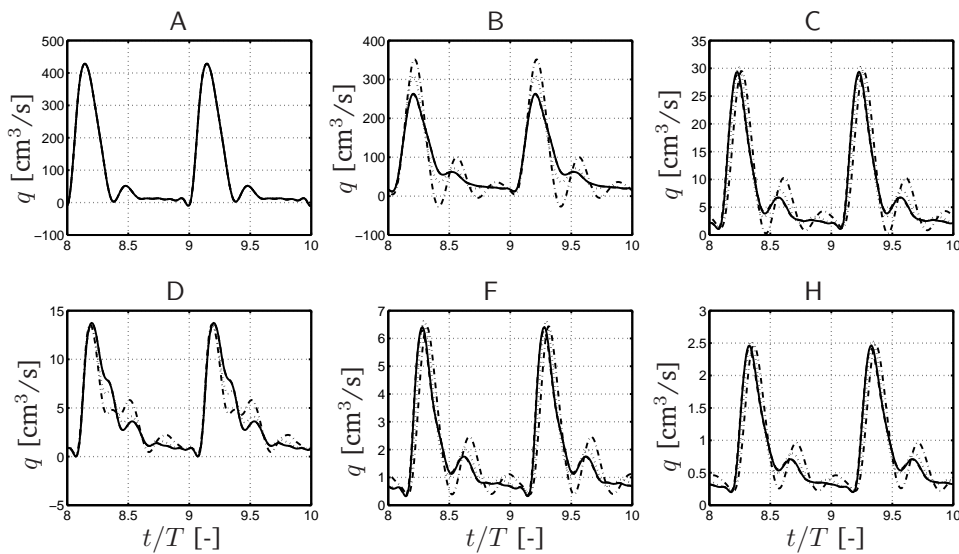


Figure 6.12: The same as figure 6.11, but now the flow as a function of time is depicted.

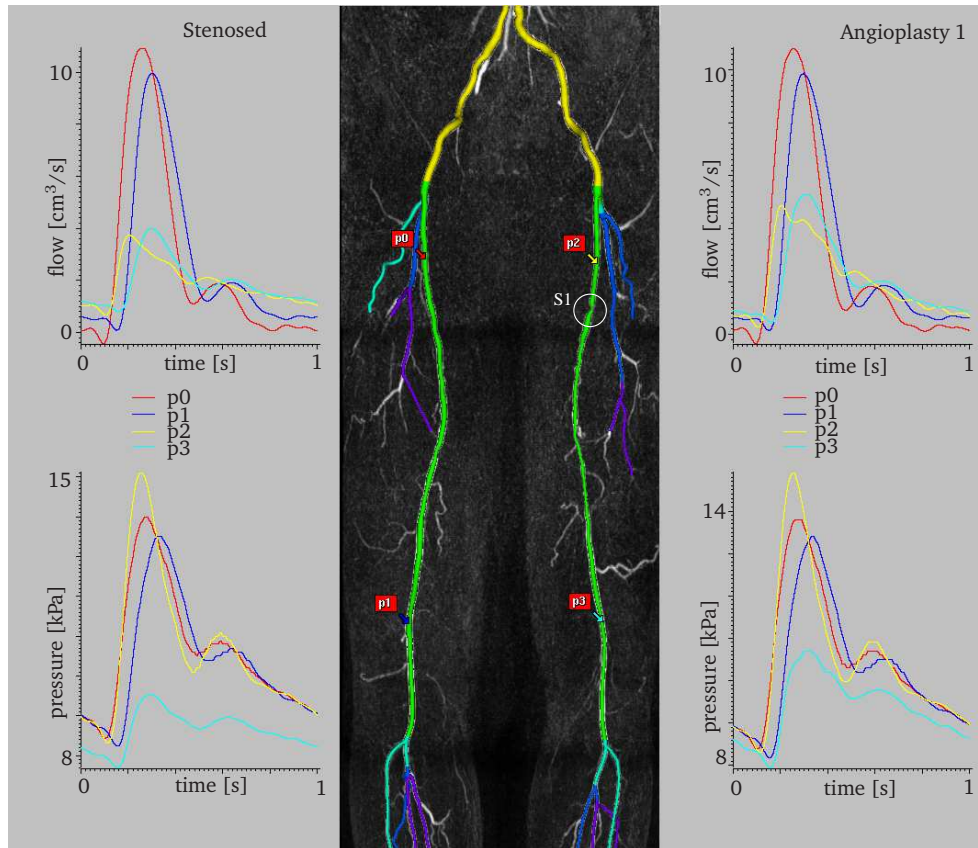


Figure 6.13: Pressure (top) and flow (bottom) as a function of time, computed at four positions in the patient-specific arterial system. On the left the results of the computation using the original geometry and on the right the results after removing the proximal stenosis (S1) by balloon angioplasty. In the middle plot the monitoring positions are indicated (by Philips Medical Systems, Best, The Netherlands).

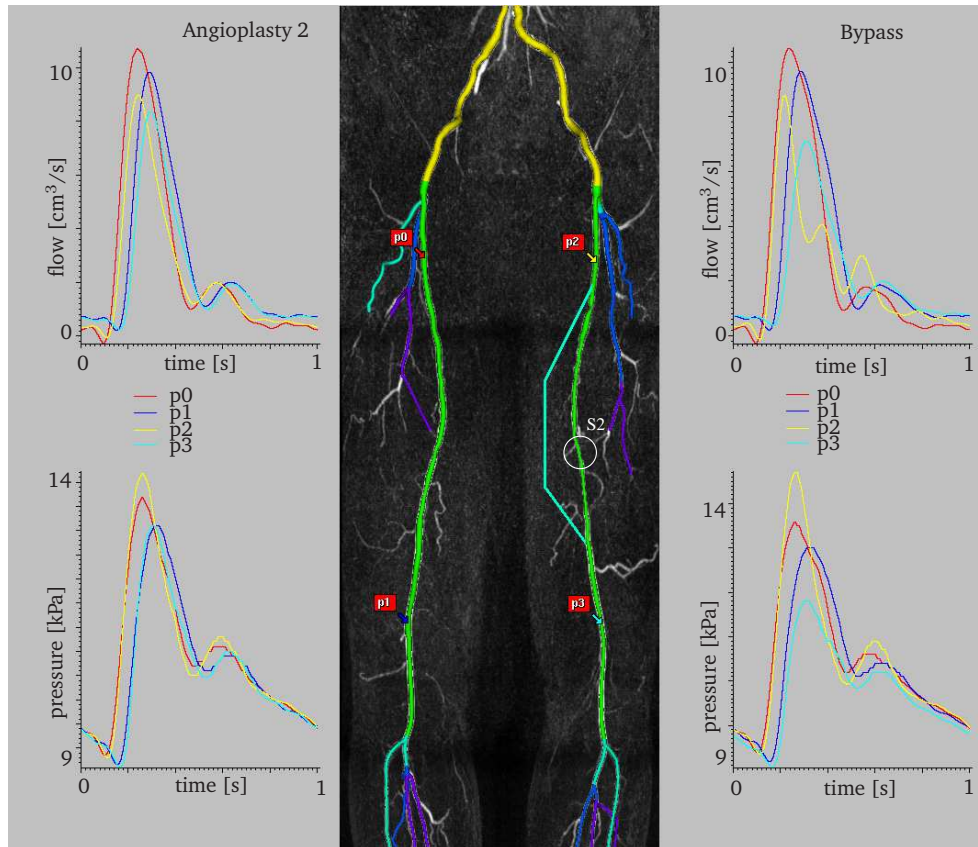


Figure 6.14: Pressure (top) and flow (bottom) as a function of time, computed at four positions in the patient-specific arterial system. On the left the results of the computation after 2 angioplasty interventions (S1 and S2) and on the right the results after placing a bypass graft around the stenotic region. In the middle plot the bypass graft and the monitoring positions are indicated (by Philips Medical Systems, Best, The Netherlands).

in sufficient perfusion of the distal vascular bed. The computations with a bypass around the stenosed region, as illustrated in figure 6.14 also shows sufficient blood flow to the distal regions. The pressure and flow waves, however, are partially reflected as a result of the discrete transition from the artery to the bypass graft. Choosing a graft with a different lumen radius or more appropriate mechanical properties of the tubes wall, can yield better results.

6.4 General Discussion

In the present thesis, a wave propagation model of the patient-specific arterial system has been presented. For the propagation of pressure and flow waves through the individual arterial segments a one-dimensional wave propagation model is used that models the non-linear flow behaviour in linear elastic or viscoelastic tapered vessels. By assuming pressure continuity and conservation of mass over each bifurcation, a coupling model is developed that interconnects the individual arterial models into the model of an arterial system. The peripheral bed for each truncated artery is modelled using a three-element Windkessel model. Moreover, special stenosis and aneurysm models are introduced to relate the pressure drop across these pathological regions to the local flow characteristics.

To obtain appropriate estimates for the frictional forces and the non-linear term in the momentum balance of the one-dimensional wave propagation model, in chapter 2 a velocity profile function is introduced that is a function of the flow, the pressure gradient and the Womersley parameter α . It is based on the division of the flow in a vessel into an inviscid core flow and a friction-dominated boundary layer flow that can behave out-of-phase. The thickness of this boundary layer is dependent on the Womersley number corresponding to the fundamental harmonic of the local flow. For single-harmonic as well as multi-harmonic physiological flow signals this velocity profile function yields estimates for the wall shear stress and convection forces that are in good agreement with the analytical solution for fully developed flow in a rigid vessel by Womersley (1957). In the present chapter, by means of the profile simulations, the influence of this newly developed velocity profile function on the pressure and flow wave propagation through the arterial system is demonstrated with respect to the commonly assumed Poiseuille profiles and flat inviscid profiles. The model based on flat frictionless velocity profiles yields significantly different wave characteristics than the models that use our approximate velocity profiles or Poiseuille profiles. The differences between the latter two are only minor throughout the arterial system. The corresponding wall shear stresses do differ significantly, especially in the larger inertia-dominated vessels. The time averaged mean wall shear stress obtained from the approximate velocity profiles is constant over the total arterial system whereas for the Poiseuille based profiles it increases towards the peripheral beds. Since the approximate velocity profile function provides the most physiologically realistic contributions of the frictional and convection forces in the one-dimensional momentum balance, as discussed in chapter 2, the results using this approach are most likely to describe the physiological situation.

In chapter 3 a constitutive law, that is based on the viscoelastic behaviour of the standard linear solid model, is introduced into the one-dimensional wave propagation model to relate the local instantaneous cross-sectional area to the local instantaneous pressure. A comparison to the pressure and flow obtained from an experimental setup shows that using our model the pressure and flow wave propagation, reflections and attenuation through straight and slightly tapered vessels can be accurately predicted. With respect to the total arterial tree, in the current chapter the computational results using a linear elastic constitutive law are compared to the results obtained from the computations with the constitutive law based on the standard

linear solid model (constitutive simulations). The viscoelastic properties of the vessel walls of the more muscular-type vessels are shown to significantly contribute to the pressure and flow wave attenuation and should be taken into account when modelling the propagation of pressure and flow waves travelling through the arterial system.

To incorporate also the effect of pathological regions in the one-dimensional wave propagation model of the arterial system, in chapters 4 and 5 the pressure drop over stenoses and aneurysms respectively as a function of the local flow characteristics has been investigated. For stenoses this resulted in a relation between the pressure drop and the flow that is dependent on the Womersley number and the shape of the restriction. The commonly used stenosis model from Young (1979), which is based on experimental work, uses a relation between the pressure drop and the flow that is dependent only on the length of the stenosis and on the maximum severity and not on the actual shape of the stenosis and on the Womersley number. By assuming that the pressure drop over the stenosis occurs linearly over the length of the pathological region, a one-dimensional momentum balance is obtained that can be used to model one-dimensional propagation of pressure and flow waves through this region. The effect of a stenosis in the femoral artery on the perfusion of the peripheral beds is demonstrated by showing results of the stenosed computations with stenoses of 70, 80 and 90% restriction of the lumen's cross-sectional area. It illustrates that a stenosis of 80% or less in the femoral artery does not lead to a significant decrease in perfusion of the peripheral beds distal to the stenosis, as was also found by Stergiopoulos et al. (1992) for patients in a resting condition. Even for more severe stenoses the distal bed is able to adjust to the decreased oxygen delivery by lowering, to a certain extent, the peripheral resistance by vasodilation. For physiologically relevant aneurysms, a relation between the pressure drop and the flow is found to depend only on the Womersley number. The shape of the aneurysm is important only for less severe aneurysms that can also be modelled using standard one-dimensional wave propagation theory. Again, the pressure drop over the pathological region is assumed to occur linearly over the length of the aneurysm, to obtain a one-dimensional momentum balance that can be used in the modelling of one-dimensional wave propagation through this region. The aneurysm computations including an aneurysm in the abdominal aorta indicate that the pressure drop over such an aneurysm is negligible with respect to the magnitude of the local pressure pulse. The sudden change in local compliance caused by the vessel dilation, however, causes wave reflections that influence the wave characteristics throughout the arterial system. Note, that in the physiological situation, the changing morphology of the aneurysm wall leads to an increase in the effective Young's modulus (Long et al. (2005)), thereby decreasing the local compliance of the aneurysm. This same effect is obtained by the formation of thrombus in the aneurysm sac, resulting in a decrease in the lumen's effective cross-sectional area.

The computations based on the patient-specific arterial system (patient) indicate that the one-dimensional wave propagation model can be used as an aid in the diagnosis and treatment of arterial diseases. Using this model, the effect of an arterial abnormality on the hemodynamics of the total arterial system can be assessed. Moreover, because of its predictive nature, the one-dimensional wave propagation model can be used to pre-operatively determine the effect of balloon angioplasty or other methods of intervention, to be used in surgical planning.

6.4.1 Model restrictions

In the current chapter, the individual arterial segments are interconnected using a bifurcation model. In the derivation of this model pressure continuity over the bifurcation is assumed, thereby stating that the pressure loss due to the viscous effects in the bifurcation are coun-

terbalanced by the pressure gained by the expansion of the total cross-sectional area over the bifurcation according to Bernoulli's law. Also, in the derivation of the 1D wave equations, the axes of the arterial segments are assumed to be straight. This means that the balancing forces for fluid flow through bends such as the aortic arch are assumed to be the same as for fluid flow through a straight vessel. These assumptions for both bifurcations and bends may be plausible in some situations but to be certain, proper estimates of the balancing forces acting in these regions must be obtained by parametric analysis using fully three-dimensional fluid structure interaction computations or laboratory experiments.

In the derivation of the velocity profile function from chapter 2, blood is assumed to behave purely Newtonian whereas it is known that the blood viscosity is shear and history dependent as a result of the deformation and aggregation of erythrocytes that are suspended in the plasma (Chien and Jan (1973)). This shear thinning behaviour of blood causes the velocity profiles and so the wall shear stress in blood vessels to differ from purely Newtonian fluid flow through such vessels. To incorporate such behaviour into the model, a shear thinning model should be adopted in the derivation of the velocity profile function.

Furthermore, the constitutive law for both the elastic and the viscoelastic model is based on thin walled tube theory. The assumption of a thin vessel wall with respect to the lumen radius cannot be used without caution because in many cases this ratio is of $\mathcal{O}(0.1)$. By adopting a piecewise linear effective Young's modulus depending on the current pressure, however, a first order appropriate model can still be derived using thin walled cylinder theory.

The computations including a stenosis in the femoral artery demonstrate the local pressure drop over this pathological region as a function of the flow characteristics. The effect of this pressure drop on the wave phenomena and on the blood division throughout the arterial tree, however, do not represent the physiological situation where the distal peripheral bed is known to adapt its resistance to a decrease in oxygen delivery. Such a response could be included in the computational model by relating the Windkessel parameter R_p to the mean local flow.

To investigate whether the model assumptions made in the previous and current chapters are valid in the physiological situation, a comparison between the pressure and flow characteristics obtained from the one-dimensional wave propagation model and an *in-vitro* model of the arterial tree is needed. In comparison to the human arterial system, from an *in-vitro* setup, all model parameters can be obtained and any possible difference between the model results and the experimental results can be ascribed to imperfections of the computational model. When modelling the propagation of pressure and flow waves through the patient-specific arterial system, based on the segmentation of MR images, minor errors in the estimation of the lumen radius can significantly influence the pulse wave velocity and attenuation. Moreover, the thickness of the local vessel wall and its mechanical properties are difficult to obtain throughout the arterial system. Therefore, here the parameters defining the constitutive relation and the ratio between the lumen radius and vessel wall thickness were based on the literature. Possible ways to estimate the arterial wall properties are by locally measuring the pulse wave velocity using an ultrasound probe and by simultaneously measuring the local arterial wall distension and the local centre-line blood velocity (Brands et al. (1996)). Using this approach, the local compliance of the vessel can be determined without a need for the wall thickness and the Young modulus. Also, the morphological components of the vessel wall can be obtained from MR images and by providing the mechanical properties for each individual material, the effective Young modulus can be derived (Dam (2007)).

6.4.2 Perspectives

Using the current one-dimensional wave propagation model, the pressure and the shear stress exerted by the blood on the vessel wall can be estimated throughout the arterial system. Since both these parameters are crucial stimuli in the remodelling process of the arterial wall, using this wave propagation model and an appropriate adaptation law, the adaptation of the vessel wall to changing physiological conditions can be predicted. This added value of the present wave propagation model can be used e.g. to predict the outcome of the surgical placement of an arteriovenous shunt in the lower arm of a hemodialysis patient to increase the blood flow through this extremity. The purpose of such a direct connection between the lumen of the radial artery to the lumen of a larger vein in the lower arm, is to bypass the highly resistive peripheral bed and thereby increasing the blood flow through these vessels and so through the hemodialysis apparatus attached to them. This increased blood flow induces an increase of the wall shear stress in both the arteries and the veins in the arm that will start an adaptation process of the vessel wall to increase the lumen diameter. Also, the pressure in the connecting veins has increased enormously, resulting in the thickening of the venous wall. To what extent these maturation processes take place is dependent on the position of the shunt placement and on the architecture of the arterial and venous system in the lower arm. The current one-dimensional wave propagation model, in combination with a suitable adaptation law can be used to predict this maturation process to pre-operatively decide on the optimal location and size of the arteriovenous shunt.

In the computations performed in this chapter, the proximal end of the arterial tree was closed using a periodic flow $q(t)$ boundary condition. A more physiological and interactive approach would be to couple the one-dimensional wave propagation model to a model of the heart (Bovendeerd et al. (2006)) that will generate a pressure and flow pulse, dependent on the total peripheral resistance, inertance and compliance.

6.5 Conclusion

A wave propagation model of the patient-specific arterial system has been developed, that is able to provide the pressure, flow and wall shear stress throughout the arterial system. The effects of different friction models on these parameters has been demonstrated and the influence of viscoelastic properties for the arterial wall model has been shown. Also, the effect of a femoral stenosis and an abdominal aortic aneurysm has been investigated.

References

- M. Abramowitz and I. Stegun. *Handbook of mathematical functions*. Dover Publications, Dover, 1964.
- M. Anliker, W. Moritz, and E. Ogden. Transmission characteristics of axial waves in blood vessels. *J. Biomech.*, 1:235–246, 1968.
- M. Anliker, L. Rockwell, and E. Ogden. Nonlinear analysis of flow pulses and shock waves in arteries. *Z. Angew. Math. Phys.*, 22:217–246, 1971.
- I. Bakirtas and N. Antar. Effect of stenosis on solitary waves in arteries. *Int. J. Eng. Sc.*, 43:730–743, 2005.
- S. Balar, T. Rogge, and D. Young. Computer simulations of blood flow in the human arm. *J. Biomech.*, 22:692–697, 1989.
- D. Bessems, M. Rutten, and F. van de Vosse. A wave propagation model of blood flow in large vessels using an approximate velocity profile function. *J. Fluid Mech.*, 580:145–168, 2007.
- P. Bovendeerd, P. Borsje, T. Arts, and F. van de Vosse. Dependence of intramyocardial pressure and coronary flow on ventricular loading and contractility: a model study. *An. Biomed. Engr.*, 34:1833–1845, 2006.
- P. Brands, A. Hoeks, M. Rutten, and R. Reneman. A non-invasive method to estimate arterial impedance by means of the assessment of the local diameter change and the local centre-line blood flow velocity using ultrasound. *Ultrasound Med. Biol.*, 7:895–905, 1996.
- T. Bülow, C. Lorenz, and S. Renisch. A general framework for tree segmentation and reconstruction from medical volume data. *LNCS*, 3216:533–540, 2004.
- H. Busch, H. Hoffmann, C. Metzner, and W. Oettinger. Mra of the vessels of the pelvis and legs with automatic table movement (mobitrak): results in 100 patients. *MedicaMundi*, 43(1):10–16, 1999.
- C. Canuto, M. Hussaini, A. Quarteroni, and T. Zang. *Spectral Methods in Fluid Dynamics*. Springer, New York, 1988.
- S. Cavalcanti. Hemodynamics of an artery with mild stenosis. *J. Biomech.*, 28:387–399, 1995.
- S. Chakravarty and P. Mandal. Two-dimensional flow through tapered arteries under stenotic conditions. *Int. J. Non-Linear Mech.*, 35:779–793, 2000.
- S. Chien and K.-M. Jan. Ultrastructural basis of the mechanism of rouleaux formation. *Microvascular Res.*, 5:155–166, 1973.
- R. H. Cox. Wave propagation through a newtonian fluid contained within a thick-walled viscoelastic tube. *Biophys. J.*, 8:691–709, 1968.
- R. H. Cox. Wave propagation through a newtonian fluid contained within a thick-walled viscoelastic tube: the influence of wall compressibility. *J. Biomech.*, 3:317–335, 1970.

- E. Dam. *Morphology and mechanical properties of abdominal aortic aneurysms*. Thesis, University of Technology Eindhoven, the Netherlands, 2007.
- V. Deplano, Y. Knapp, E. Bertrand, and E. Gaillard. Flow behaviour in an asymmetric compliant experimental model for abdominal aortic aneurysms. *J. Biomech.*, in press, 2007.
- C. Egelhoff, R. Budwig, D. Elger, T. Khraishi, and K. H. Johansen. Model studies of the flow in abdominal aortic aneurysms during resting and exercise conditions. *J. Biomech.*, 32:1319–1329, 1999.
- E. Finol, K. Keyhani, and C. Amon. The effect of asymmetry in abdominal aortic aneurysms under physiologically realistic pulsatile flow conditions. *J. Biomech. Eng.*, 125:207–217, 2003.
- L. Formaggia, J. Gerbeau, F. Nobile, and A. Quarteroni. On the coupling of 3d and 1d navier-stokes equations for flow problems in compliant vessels. *Comput. Methods Appl. Mech. Eng.*, 191:561–582, 2001.
- Y. Fung. *Biomechanics: mechanical properties of living tissues*. Springer, Berlin, Germany, 1993.
- C. Giannopapa. *Fluid structure interaction in flexible vessels*. University of London, London, England, 2004.
- F. Gijssen, F. van de Vosse, and J. Janssen. Influence of the non-newtonian properties of blood on the flow in large arteries: Steady flow in a carotid bifurcation model. *J. Biomech.*, 32:601–608, 1999a.
- F. Gijssen, F. van de Vosse, and J. Janssen. Influence of the non-newtonian properties of blood on the flow in large arteries: Unsteady flow in a 90-degree curved tube. *J. Biomech.*, 32:705–713, 1999b.
- T. Hughes and J. Lubliner. On the one-dimensional theory of blood flow in the large vessels. *Math. Biosci.*, 18:161–170, 1973.
- J. Humphrey. Mechanics of the arterial wall: Review and directions. *Critical Rev. Biomed. Engr.*, 23:1–162, 1995.
- T. Ishikawa, L. Guimaraes, S. Oshima, and R. Yamane. Effect of non-newtonian property of blood on flow through a stenosed tube. *Fluid Dyn. Res.*, 22:251–264, 1998.
- P.-Y. Lagrée. An inverse technique to deduce the elasticity of a large artery. *Eur. Phys. J. Ap.*, 9:153–163, 2000.
- T. Lanne, B. Sonesson, D. Bergqvist, H. Bengtsson, and D. Gustafsson. Diameter and compliance in the male human abdominal aorta: influence of age and aortic aneurysm. *Eur. J. Vasc. Surg.*, 6:178–184, 1992.
- B. Learoyd and M. Taylor. Alterations with age in the viscoelastic properties of human arterial walls. *Circ. Res.*, 18:278–292, 1966.
- A. Long, L. Rouet, A. Bissery, P. Rossignol, D. Mouradian, and M. Sapoval. Compliance of abdominal aortic aneurysms evaluated by tissue doppler imaging: Correlation with aneurysm size. *J. Vasc. Surg.*, 42:18–26, 2005.
- Q. Long, X. Xu, K. Ramnarine, and P. Hoskins. Numerical investigation of physiologically realistic pulsatile flow through arterial stenosis. *J. Biomech.*, 34:1229–1242, 2001.
- P. Mandal. An unsteady analysis of non-newtonian blood flow through tapered arteries with a stenosis. *Int. J. Non-Linear Mech.*, 40:151–164, 2005.
- W. Milnor. *Hemodynamics*. Williams & Wilkins, London, England, 1989.
- M. Moayeri and G. Zendehebudi. Effects of elastic property of the wall on flow characteristics through arterial stenoses. *J. Biomech.*, 36:525–535, 2003.

- C. Murray. The physiological principle of minimum work. i. the vascular system and the cost of blood volume. *Physiology*, 12:207–214, 1926.
- M. Olufsen. Structured tree outflow condition for blood flow in larger systemic arteries. *Am. J. Physiol.*, 276:H257–H268, 1999.
- M. Olufsen and C. Peskin. Numerical simulation and experimental validation of blood flow in arteries with structured-tree outflow conditions. *Ann. of Biomed. Eng.*, 28:1281–1299, 2000.
- L. Pater and J. Berg. An electrical analogue of the entire human circulatory system. *Med. Electron. and Biol. Eng.*, 2:161–166, 1964.
- T. Pedley. *The fluid mechanics of large blood vessels*. Cambridge University Press, Cambridge, 1980.
- K. Perktold. On the path of fluid particles in an axisymmetrical aneurysm. *J. Biomech.*, 20:311–317, 1987.
- G. Porenta, D. Young, and T. Rogge. A finite element model of blood flow in arteries including taper, branches and obstructions. *J. Bio. Eng.*, 108:161–167, 1986.
- W. Pritchard, P. Davies, Z. Derafshi, D. Polacek, R. D. R. Tsao, S. Jones, and D. Giddens. Effects of wall shear stress and fluid recirculation on the localization of circulating monocytes in a three-dimensional flow model. *J. Biomech.*, 28:1459–1469, 1995.
- J. Raines, M. Jaffrin, and A. Shapiro. A computer simulation of arterial dynamics in the human leg. *J. Biomech.*, 7:77–91, 1974.
- B. Rathish-Kumar and K. Naidu. Hemodynamics in aneurysm. *Computers and biomedical research*, 2:119–139, 1996.
- E. Rooz, D. Young, and T. Rogge. A finite-element simulation of pulsatile flow in flexible obstructed tubes. *J. Biomech. Eng.*, 104:119–124, 1982.
- B. Schaaf. Digital computer simulation of human systemic arterial pulse wave transmission. *J. Biomechanics*, 5:345–364, 1972.
- H. Schlichting. *Boundary Layer Theory*. McGraw-Hill, New York, 1960.
- C. Scotti and A. Finol. Compliant biomechanics of abdominal aortic aneurysms: A fluid-structure interaction study. *Comput. struct.*, in press, 2007.
- B. Seeley and D. Young. Effect of geometry on pressure losses across models of arterial stenoses. *J. Biomech.*, 9:439–448, 1976.
- S. Sherwin, L. Formaggia, J. Peiró, and V. Franke. Computational modelling of 1d blood flow with variable mechanical properties and its application to the simulation of wave propagation in the human arterial system. *Int. J. Num. Meth. Fluids*, 43:673–700, 2003.
- M. Siouffi, R. Pelissier, D. Farahifar, and R. Rieu. The effect of unsteadiness on the flow through stenoses and bifurcation. *J. Biomech.*, 17:299–315, 1984.
- M. Siouffi, V. Deplano, and R. Pelissier. Experimental analysis of unsteady flows through a stenosis. *J. Biomech.*, 31:11–19, 1998.
- B. Steele, J. Wan, J. Ku, T. Hughes, and C. Taylor. In vivo validation of a one-dimensional finite-element method for predicting blood flow in cardiovascular bypass grafts. *IEEE Trans. BioMed. Eng.*, 50:649–656, 2003.
- N. Stergiopoulos, D. Young, and T. Rogge. Computer simulation of arterial flow with application to arterial and aortic stenoses. *J. Biomech.*, 25:1477–1488, 1992.
- N. Stergiopoulos, M. Spiridon, F. Pythoud, and J.-J. Meister. On the wave transmission and reflection properties of stenoses. *J. Biomech.*, 29:31–38, 1996.

- N. Stergiopoulos, B. Westerhof, and N. Westerhof. Total arterial inertance as the fourth element of the windkessel model. *Am. J. Physiol.*, 276:H81–H88, 1999.
- C. Taylor, T. Hughes, and C. Zarins. Finite element modeling of blood flow in arteries. *Comput. Meth. Appl. Mech. Eng.*, 158:155–196, 1998.
- G. Tortora and N. Anagnostakos. *Principles of anatomy and physiology*. Harper and Row Publishers, Nw York, 1990.
- F. Tsou, P. Chou, S. Frankel, and A. Hahn. An integral method for the analysis of blood flow. *Bull. of Math. Biophys.*, 33:117–128, 1971.
- C. Tu and M. Deville. Pulsatile flow of non-newtonian fluids through arterial stenoses. *J. Biomech.*, 29:899–908, 1996.
- C. Tu, M. Deville, L. Dheur, and L. Vanderschuren. Finite element simulation of pulsatile flow through arterial stenosis. *J. Biomech.*, 25:1141–1152, 1992.
- F. van de Vosse, J. Hart, C. van Oijen, D. Bessems, T. Gunther, A. Segal, B. Wolters, J. Stijnen, and F. Baaijens. Finite-element-based computational methods for cardiovascular fluid-structure interaction. *J. of Eng. Math.*, 47:335–368, 2003.
- J. Wan, B. Steele, S. Spicer, S. Strohsand, C. Feijoo, T. Hughes, and C. Taylor. A one-dimensional finite element method for simulation-based medical planning for cardiovascular disease. *Comput. Meth. Biomech. Biomed. Eng.*, 5:195–206, 2002.
- J. Wang and H. Parker. Wave propagation in a model of the arterial circulation. *J. Biomech.*, 37:457–470, 2004.
- N. Westerhof, F. Bosman, C. de Vries, and A. Noordergraaf. Analog studies of the human systemic arterial tree. *J. Biomech.*, 2:121–143, 1969.
- S. Wille. Pulsatile pressure and flow in an arterial aneurysm simulated in a mathematical model. *J. Biomed. Engng.*, 3:153–158, 1981.
- K. Witzig. *Über erzwungene Wellenbewegungen zäher, incompressibler Flüssigkeiten in elastischen Röhren, Inaugural Dissertation*. University of Bern, Bern, 1914.
- B. Wolters, M. Rutten, G. Schurink, U. Kose, J. de Hart, and F. van de Vosse. A patient-specific computational model of fluid-structure interaction in abdominal aortic aneurysms. *Med. Eng. Phys.*, 27(10):871–883, 2005.
- J. Womersley. An elastic tube theory of pulse transmission and oscillatory flow in mammalian arteries. *Technical Report WADC-TR-56-614*, 1957.
- D. Young. Fluid mechanics of arterial stenosis. *J. Biomech. Eng.*, 101:157–175, 1979.
- D. Young and F. Tsai. Flow characteristics in models of arterial stenoses-i. steady flow. *J. Biomech.*, 6:395–410, 1973a.
- D. Young and F. Tsai. Flow characteristics in models of arterial stenoses-ii. unsteady flow. *J. Biomech.*, 6:547–559, 1973b.
- M. Zagzoule, J. Khalid-Naciri, and J. Mauss. Unsteady wall shear stress in a distensible tube. *J. Biomech.*, 24:435–439, 1991.

Appendix A

Derivation of non-linear part

The derivation of $\gamma(p, q) = A\overline{v_z^2}$ is illustrated by determining the square of the velocity profile $v_z(p, q)$ and integrating the result over cross sectional area A . The velocity profile as presented in (2.18) is taken as the point of departure:

$$v_z = \frac{-\ln \hat{\zeta}}{1 - \zeta_c} \bar{v}_z - \frac{a^2}{4\eta} \left[1 - \hat{\zeta} + \frac{1}{2}(\zeta_c + 1) \ln \hat{\zeta} \right] \frac{\partial p}{\partial z} \quad (\text{A.1})$$

or

$$v_z = \phi_1 \bar{v}_z + \phi_2 v_p \quad (\text{A.2})$$

with ϕ_1 and ϕ_2 defined as

$$\phi_1 = \frac{-\ln \hat{\zeta}}{1 - \zeta_c} \quad \text{and} \quad \phi_2 = 1 - \hat{\zeta} + \frac{1}{2}(\zeta_c + 1) \ln \hat{\zeta} \quad (\text{A.3})$$

and

$$v_p = -\frac{a^2}{4\eta} \frac{\partial p}{\partial z}. \quad (\text{A.4})$$

From this, v_z^2 is given by

$$v_z^2 = \phi_1^2 \bar{v}_z^2 + 2\phi_1\phi_2 \bar{v}_z v_p + \phi_2^2 v_p^2. \quad (\text{A.5})$$

Taking the mean of this term and multiplying by A results in

$$A\overline{v_z^2} = 2\pi \left(\int_0^a \phi_1^2 r dr \right) \bar{v}_z^2 + 2\pi \left(\int_0^a 2\phi_1\phi_2 r dr \right) \bar{v}_z v_p + 2\pi \left(\int_0^a \phi_2^2 r dr \right) v_p^2 \quad (\text{A.6})$$

or, choosing a more appropriate notation and using $\bar{v}_z \equiv q/A$,

$$A\overline{v_z^2} = \int_0^1 \phi_1^2 d\zeta \frac{q^2}{A} - \int_0^1 2\phi_1\phi_2 d\zeta q v_p + A \int_0^1 \phi_2^2 d\zeta v_p^2. \quad (\text{A.7})$$

Introducing functions δ_1 , δ_2 and δ_3 according to

$$\begin{aligned}\delta_1(\zeta_c) &= \int_0^1 \phi_1^2 d\zeta = \frac{2 - 2\zeta_c(1 - \ln \zeta_c)}{(1 - \zeta_c)^2} \\ \delta_2(\zeta_c) &= -2 \int_0^1 \phi_1 \phi_2 d\zeta = \frac{1 + 4\zeta_c(1 + \ln \zeta_c) - \zeta_c^2(5 - 2 \ln \zeta_c)}{1 - \zeta_c} \\ \delta_3(\zeta_c) &= \int_0^1 \phi_2^2 d\zeta = \frac{1}{3} + \zeta_c(3 + 2 \ln \zeta_c) - \zeta_c^2(3 - 2 \ln \zeta_c) - \frac{1}{3}\zeta_c^3\end{aligned}\tag{A.8}$$

yields the expression for $\gamma(p, q)$:

$$\gamma(p, q) = \delta_1 \frac{q^2}{A} + \delta_2 q \frac{a^2}{4\eta} \frac{\partial p}{\partial z} + \delta_3 A \left(\frac{a^2}{4\eta} \frac{\partial p}{\partial z} \right)^2\tag{A.9}$$

Appendix B

Spatial discretisation

Strong form

Consider spatial domain $\Omega = [\Gamma_{in}, \Gamma_{out}] \subset \mathbb{R}$ and a time period $T = [0, T_e]$. Assume that $\mathbf{N}(\mathbf{u}, z, t)$, $\mathbf{D}(\mathbf{u}, z, t)$, $\mathbf{H}(\mathbf{u}, z, t)$ and $\mathbf{f}(\mathbf{u}, z, t)$ are matrices of known functions from $\Omega \rightarrow \mathbb{R}$. The strong form of the one-dimensional wave propagation problem is then given by:
find $\mathbf{u}(z, t) = [u_1(z, t), u_2(z, t)] : \Omega \times T \rightarrow \mathbb{R} \times \mathbb{R}$ that is a solution of:

$$\left. \begin{aligned} \frac{\partial \mathbf{u}}{\partial t} + \mathbf{N} \frac{\partial \mathbf{u}}{\partial z} - \mathbf{D} \frac{\partial^2 \mathbf{u}}{\partial z^2} + \mathbf{H} \mathbf{u} &= \mathbf{f} && \text{in } \Omega \\ u_2(z, t) &= u_{2in}(t) && \text{for } z = \Gamma_{in}, \\ u_1(z, t) &= u_{1out}(t) && \text{for } z = \Gamma_{out}, \\ \mathbf{u}(z, 0) &= \mathbf{u}^0(z) && \text{for } t = 0, \end{aligned} \right\} \quad (\text{B.1})$$

with $u_1 = p$ the pressure and $u_2 = q$ the flow. Functions u_{2in} and u_{1out} define the boundary conditions and $\mathbf{u}^0(z) = (u_1^0(z), u_2^0(z))$ is a given function that defines the initial condition.

Weak form

To derive a weak form of the problem (B.1) we define the space of trial functions that satisfy the Dirichlet boundary conditions at Γ_{in} and Γ_{out} :

$$\mathbf{U} = \{\mathbf{u} | \mathbf{u} \in H^1(\Omega) \times H^1(\Omega), u_1|_{\Gamma_{out}} = u_{1out}, u_2|_{\Gamma_{in}} = u_{2in}\}. \quad (\text{B.2})$$

Moreover, we define a set of test functions that satisfy the homogeneous Dirichlet conditions:

$$\mathbf{W} = \{\mathbf{w} | \mathbf{w} \in H^1(\Omega) \times H^1(\Omega), w_1|_{\Gamma_{out}} = 0, w_2|_{\Gamma_{in}} = 0\}. \quad (\text{B.3})$$

Here $H^1(\Omega)$ is the Hilbert space defined by:

$$H^1(\Omega) = \{v \in L^2(\Omega) | \int_{\Omega} \left(\frac{\partial v}{\partial z} \right)^2 d\Omega < \infty\} \quad (\text{B.4})$$

with $L^2(\Omega)$ the space of square integrable functions:

$$L^2(\Omega) = \{v \mid \int_{\Omega} v^2 d\Omega < \infty\} \quad (\text{B.5})$$

endowed with the inner product:

$$(u, w)_{L^2} = \int_{\Omega} u w d\Omega \quad (\text{B.6})$$

The corresponding weak form of (B.1) is:
find $\mathbf{u}(z, t) \in \mathbf{U}$ such that $\forall \mathbf{w} \in \mathbf{W}$:

$$\begin{aligned} & \int_{\Omega} w_l \frac{\partial u_l}{\partial t} d\Omega + \sum_{k=1}^2 \int_{\Omega} w_l N_{lk} \frac{\partial u_k}{\partial z} d\Omega + \int_{\Omega} \frac{\partial w_l}{\partial z} \cdot D_{lk} \frac{\partial u_k}{\partial z} d\Omega + \\ & + \int_{\Omega} w_l H_{lk} u_k d\Omega = \int_{\Omega} w_l f_l d\Omega \quad \text{for } l = 1, 2 \end{aligned} \quad (\text{B.7})$$

with N_{lk} , D_{lk} , H_{lk} and f_l the matrix components of matrices \mathbf{N} , \mathbf{D} , \mathbf{H} and \mathbf{f} , as defined in (2.43) and (2.44), respectively. Note that the boundary integral resulting from the partial integration of diffusion term \mathbf{D}

$$\int_{\Gamma} \mathbf{w} \mathbf{D} \frac{\partial \mathbf{u}}{\partial z} d\Gamma = -w_2 D_{22} \frac{\partial u_2}{\partial z} \Big|_{\Gamma_{out}} \quad (\text{B.8})$$

has been omitted. Since this term \mathbf{D} -term is small and is only kept for numerical stability, this will not induce strong constraints on u_1 and u_2 .

Discrete form

With the aid of the basis functions $\phi_i(z)$ we define the subspaces $\mathbf{U}^h \subset \mathbf{U}$ and $\mathbf{W}^h \subset \mathbf{W}$ according to

$$\mathbf{U}^h = \{\mathbf{u}^h \mid \mathbf{u}^h(z, t) = \sum_{i=1}^N \mathbf{u}_i(t) \phi_i(z), u_1^h|_{\Gamma_{out}} = u_{1_{out}}, u_2^h|_{\Gamma_{in}} = u_{2_{in}}\}, \quad (\text{B.9})$$

$$\mathbf{W}^h = \{\mathbf{w}^h \mid \mathbf{w}^h(z) = \sum_{i=1}^N \mathbf{w}_i \phi_i(z), w_1^h|_{\Gamma_{out}} = 0, w_2^h|_{\Gamma_{in}} = 0\}, \quad (\text{B.10})$$

so after introduction of

$$\underline{v}^T = [v_1, \dots, v_N] \quad \text{for } v = u_1, u_2, w, f, \phi \quad (\text{B.11})$$

and using translations

$$\sum_{i=1}^N \mathbf{u}_i(t) \phi_i(z) = \underline{\mathbf{u}}^T \cdot \underline{\phi} \quad \text{and} \quad \sum_{i=1}^N \mathbf{w}_i(t) \phi_i(z) = \underline{\mathbf{w}}^T \cdot \underline{\phi}, \quad (\text{B.12})$$

the Galerkin weak form of (B.1) is:
find $\mathbf{u}^h(z, t) \in \mathbf{U}^h$ such that $\forall \mathbf{w}^h \in \mathbf{W}^h$:

$$\begin{aligned} & \int_{\Omega} \mathbf{w}_l^T \underline{\phi} \cdot \dot{\mathbf{u}}_l^T \underline{\phi} \, d\Omega + \sum_{k=1}^2 \int_{\Omega} \mathbf{w}_l^T \underline{\phi} \cdot N_{lk} \mathbf{u}_k^T \frac{\partial \underline{\phi}}{\partial z} \, d\Omega + \int_{\Omega} \mathbf{w}_l^T \frac{\partial \underline{\phi}}{\partial z} \cdot D_{lk} \mathbf{u}_k^T \frac{\partial \underline{\phi}}{\partial z} \, d\Omega + \\ & + \int_{\Omega} \mathbf{w}_l^T \underline{\phi} \cdot H_{lk} \mathbf{u}_k^T \underline{\phi} \, d\Omega = \int_{\Omega} \mathbf{f}_l^T \underline{\phi} \cdot \mathbf{w}_l^T \underline{\phi} \, d\Omega \quad \text{for } l = 1, 2 \end{aligned} \quad (\text{B.13})$$

or, when considering that these equations must hold for all admissible $w \in \mathbf{W}^h$:
Find $\mathbf{u}^h(z, t) \in \mathbf{U}^h$ such that $\forall \mathbf{w}^h \in \mathbf{W}^h$:

$$\begin{aligned} & \int_{\Omega} \underline{\phi} \underline{\phi}^T \, d\Omega \, \dot{\mathbf{u}}_l + \sum_{k=1}^2 \int_{\Omega} \underline{\phi} N_{lk} \frac{\partial \underline{\phi}^T}{\partial z} \, d\Omega \, \mathbf{u}_k + \int_{\Omega} \frac{\partial \underline{\phi}}{\partial z} D_{lk} \frac{\partial \underline{\phi}^T}{\partial z} \, d\Omega \, \mathbf{u}_k + \\ & + \int_{\Omega} \underline{\phi} H_{lk} \underline{\phi}^T \, d\Omega \, \mathbf{u}_k = \int_{\Omega} \underline{\phi} \underline{\phi}^T \, d\Omega \, \mathbf{f}_l \quad \text{for } l = 1, 2. \end{aligned} \quad (\text{B.14})$$

With the introduction of the matrices:

$$\begin{aligned} \underline{M} &= \int_{\Omega} \underline{\phi} \underline{\phi}^T \, d\Omega, & \underline{N}_{lk} &= \int_{\Omega} \underline{\phi} N_{lk} \frac{\partial \underline{\phi}^T}{\partial z} \, d\Omega, \\ \underline{D}_{lk} &= \int_{\Omega} \frac{\partial \underline{\phi}}{\partial z} D_{lk} \frac{\partial \underline{\phi}^T}{\partial z} \, d\Omega, & \underline{H}_{lk} &= \int_{\Omega} \underline{\phi} H_{lk} \underline{\phi}^T \, d\Omega, \end{aligned} \quad (\text{B.15})$$

this yields

$$\underline{M} \dot{\mathbf{u}}_l + \sum_{k=1}^2 \underline{N}_{lk} \mathbf{u}_k + \underline{D}_{lk} \mathbf{u}_k + \underline{H}_{lk} \mathbf{u}_k = \underline{M} \mathbf{f}_l \quad \text{for } l = 1, 2 \quad (\text{B.16})$$

Spectral element approximation

First the basis functions ϕ are restricted to functions that satisfy:

$$\phi_i(z_j) = \delta_{ij}, \quad i = 1, \dots, N, \quad (\text{B.17})$$

with δ_{ij} the Kronecker delta function and z_j a set of collocation points such that $\Gamma_{in} \leq z_j \leq \Gamma_{out}$ for $j = 1, \dots, N$. Consequently the values of the parameters \mathbf{u}_i are equal to the approximate solution at the collocation point:

$$\mathbf{u}_l^h(z_j) = \sum_{i=1}^N \mathbf{u}_{l,i} \phi_i(z_j) = \mathbf{u}_{l,j}, \quad j = 1, \dots, N. \quad (\text{B.18})$$

Secondly the domain Ω is decomposed into a finite number N_e of sub-domains (elements) Ω_e . The integrations that appear in (B.15) then can be carried out element by element according to:

$$\int_{\Omega} f \, d\Omega = \sum_{e=1}^{N_e} \int_{\Omega_e} f_e \, d\Omega \quad (\text{B.19})$$

where f_e is the restriction of f on Ω_e . If we choose the element boundaries to coincide with a subset of the collocation points, to satisfy (B.17), we can define the basis functions by the Lagrange interpolation polynomials through the $n + 1$ collocation points in each element:

$$\phi_i(z) = \frac{\prod_{k=0, k \neq i}^n (z - z_k)}{\prod_{k=0, k \neq i}^n (z_i - z_k)} \quad i = 0, \dots, n \quad (\text{B.20})$$

Finally we use a Legendre-Gauss-Lobatto integration and choose the Lagrange interpolation points to be equal to the Legendre-Gauss-Lobatto points:

$$\int_{\Omega_e} f(z) dz = \int_{-1}^1 f(\xi) \frac{dz}{d\xi} d\xi \approx \sum_{k=0}^n f(\xi_k^{gl}) J(\xi_k^{gl}) w_k^{gl} \quad (\text{B.21})$$

with ξ_k^{gl} the Legendre-Gauss-Lobatto integration points defined as the zeros of the first derivative of the n -th order Legendre polynomial $L_n(\xi)$ extended with the element boundary $\xi_0 = -1$, $\xi_n = 1$, $J(\xi_k^{gl})$ the Jacobian $dz/d\xi$, and w_k^{gl} the Legendre-Gauss-Lobatto weight functions defined by Canuto et al. (1988):

$$w_k^{gl} = \frac{2}{n(n+1)} \frac{1}{L_n^2(\xi_k)} \quad k = 0, \dots, n \quad (\text{B.22})$$

Appendix C

Linearisation of equations

Before linearising the general set of equations a few assumptions are introduced. First, the arterial wall thickness is assumed constant in time, hence $\partial h/\partial t = 0$. The velocity profile functions δ_1 , c_p and c_q as well as the compliance C and resistance R are computed using the initial radius a_0 . Newton-Raphson linearisation of the non-linear parts of equation (3.17) is accomplished by approximations

$$f(A, q, p) \approx f(A_i, q_i, p_i) + \frac{\partial}{\partial A} \left(f(A_i, q_i, p_i) \right) (A - A_i) + \frac{\partial}{\partial q} \left(f(A_i, q_i, p_i) \right) (q - q_i) + \frac{\partial}{\partial p} \left(f(A_i, q_i, p_i) \right) (p - p_i) \quad (\text{C.1})$$

where f is the nonlinear term and subscript i indicates the solution of the previous iteration. By repeatedly solving the system of equations, the iterative solution should approach a converged state. First, the individual parts of the convective term are linearised:

$$\begin{aligned} 2\delta_1 \frac{q}{A} \frac{\partial q}{\partial z} &\approx \left[2\delta_1 \frac{1}{A_i} \frac{\partial q_i}{\partial z} \right] q + \left[2\delta_1 \frac{q_i}{A_i} \right] \frac{\partial q}{\partial z} + \left[-2\delta_1 \frac{q_i}{A_i^2} \frac{\partial q_i}{\partial z} \right] A \\ -\delta_1 \left(\frac{q}{A} \right)^2 \frac{\partial A}{\partial z} &\approx \left[-2\delta_1 \frac{q_i}{A_i^2} \frac{\partial A_i}{\partial z} \right] q + \left[2\delta_1 \frac{q_i^2}{A_i^3} \frac{\partial A_i}{\partial z} \right] A + \left[-\delta_1 \frac{q_i^2}{A_i^2} \right] \frac{\partial A}{\partial z} \\ \frac{q^2}{A} \frac{\partial \delta_1}{\partial z} &\approx \left[2 \frac{q_i}{A_i} \frac{\partial \delta_1}{\partial z} \right] q + \left[-\frac{q_i^2}{A_i^2} \frac{\partial \delta_1}{\partial z} \right] A \end{aligned} \quad (\text{C.2})$$

where the terms between straight brackets indicate the contribution of each part to the eventual linear system of equations (3.17). Next, the contribution of the pressure gradient is linearised.

$$\frac{A}{\rho} (2 - c_p) \frac{\partial p}{\partial z} \approx \left[\frac{1}{\rho} (2 - c_p) \frac{\partial p_i}{\partial z} \right] A + \left[\frac{A_i}{\rho} (2 - c_p) \right] \frac{\partial p}{\partial z} + \left[-\frac{A_i}{\rho} (2 - c_p) \frac{\partial p_i}{\partial z} \right] \quad (\text{C.3})$$

The last term in the momentum balance to be linearised is the friction term.

$$\frac{A}{\rho} c_q R q \approx \left[\frac{q_i}{\rho} c_q R \right] A + \left[\frac{A_i}{\rho} c_q R \right] q + \left[-\frac{A_i}{\rho} c_q R q_i \right] \quad (\text{C.4})$$

Conclusively, the non-linear terms of the constitutive law are linearised.

$$\frac{a}{h} p = \frac{\sqrt{\frac{A}{\pi}}}{h} p \approx \left[\frac{\sqrt{\frac{A_i}{\pi}}}{h} \right] p + \left[\frac{p_i}{2h\sqrt{A_i\pi}} \right] A - \left[\frac{\sqrt{\frac{A_i}{\pi}}}{2h} p_i \right] \quad (\text{C.5})$$

$$\frac{a}{h} \frac{\partial p}{\partial t} = \frac{\sqrt{\frac{A}{\pi}}}{h} \frac{\partial p}{\partial t} \approx \left[\frac{\sqrt{\frac{A_i}{\pi}}}{h} \right] \frac{\partial p}{\partial t} + \left[\frac{1}{2h\sqrt{A_i\pi}} \frac{\partial p_i}{\partial t} \right] A - \left[\frac{\sqrt{\frac{A_i}{\pi}}}{2h} \frac{\partial p_i}{\partial t} \right] \quad (\text{C.6})$$

$$\frac{p}{h} \frac{\partial a}{\partial t} = \frac{p}{h} \frac{\partial}{\partial t} \left(\sqrt{\frac{A}{\pi}} \right) \approx \left[\frac{1}{h} \frac{\partial}{\partial t} \left(\sqrt{\frac{A_i}{\pi}} \right) \right] p + \left[\frac{p_i}{2h} \frac{\partial}{\partial t} \left(\frac{1}{\sqrt{A_i\pi}} \right) \right] A - \left[\frac{p_i A_i}{2h} \frac{\partial}{\partial t} \left(\frac{1}{\sqrt{A_i\pi}} \right) \right]. \quad (\text{C.7})$$

Samenvatting

Om bij cardiovasculaire chirurgie preoperatief de verschillende interventie mogelijkheden te kunnen evalueren zijn patiëntspecifieke fysiologische data zoals de bloeddruk, het bloeddebiet en de wandschuifspanning nodig. Deze data kunnen worden verkregen met behulp van numerieke modellen van het arteriële systeem. Aangezien volledig driedimensionale numerieke modellen slechts een klein segment van de arteriële boom kunnen modelleren, zijn ééndimensionale golfvoortplantingsmodellen van het gehele arteriële systeem meer geschikt om klinisch relevante informatie te verkrijgen. Huidige ééndimensionale golfvoortplantingsmodellen van het arteriële stelsel maken gebruik van aannames met betrekking tot de wrijvingsterm en de niet-lineaire term in de momenten balans, die de fysiologische situatie incorrect representeren. De constitutieve wet, die de bloeddruk koppelt aan het oppervlak van de dwarsdoorsnede van het lumen, is veelal gebaseerd op lineair elastisch materiaalgedrag. Uit de literatuur is echter bekend dat de arteriële wand viscoelastische eigenschappen bezit die het golfgedrag kunnen beïnvloeden. Ook zijn bestaande ééndimensionale golfvoortplantingsmodellen enkel bruikbaar in arteriële segmenten waarin de radiale snelheid van het bloed verwaarloosbaar klein is ten opzichte van de axiale component. In pathologische gebieden, zoals bij stenosen en aneurysmata, is dit door de sterke axiale gradiënt in het lumen oppervlak vaak niet het geval.

In dit onderzoek is een ééndimensionaal golfvoortplantingsmodel ontwikkeld, dat gebruik maakt van een snelheidsprofielfunctie die fysiologische benaderingen geeft voor de wrijvingssterm en de niet-lineaire term. De hieruit resulterende waarden voor de wandschuifspanning en convectieve term komen sterk overeen met hun analytisch verkregen waarden voor pulserende stroming door een rechte starre buis. Wat betreft het wandgedrag van de vaten, is er een constitutieve relatie geïntroduceerd die gebaseerd is op het mechanische gedrag van het Kelvin model. Het resulterende ééndimensionale golfvoortplantingsmodel is gevalideerd door de gesimuleerde druk en het debiet te vergelijken met data verkregen uit een experimentele opstelling waarmee vloeistofstroming door rechte en taps toelopende polyurethane vaten gemodelleerd kan worden. Om het verkregen ééndimensionale golfvoortplantingsmodel toe te kunnen passen op patiëntspecifieke arteriële netwerken is een bifurcatie model geïmplementeerd om de druk en het debiet in de moederarterie te koppelen aan de druk en het debiet in de dochterarterieën. Daarnaast zijn er afsluitimpedanties geïntroduceerd die gebaseerd zijn op een drie-elementen Windketel model om hiermee geschikte randvoorwaarden te creëren voor de uiteinden van de arteriële boom. Aangezien er in patiëntspecifieke modellen van het arteriële stelsel stenosen en aneurysmata voor kunnen komen zijn voor deze vaatsegmenten speciale ééndimensionale golfvoortplantingsmodellen ontwikkeld. Deze modellen zijn gebaseerd op een numerieke studie van bloedstroming door tweedimensionale axisymmetrische starre geometrieën van stenosen en aneurysmata en zijn afhankelijk van de geometrische eigenschappen van de pathologische gebieden en van de karakteristieke eigenschappen van de bloedstroming door deze gebieden. Het uiteindelijk verkregen model is toegepast op een geïdealiseerde ar-

teriële boom bekend uit de literatuur om hiermee de invloed van de verschillende modelaannames op de bloeddruk, het debiet en de wandschuifspanning te kunnen onderzoeken. De bloeddruk en het debiet, berekend met het ééndimensionale golfvoortplantingsmodel dat gebruik maakt van de snelheidsprofielfunctie verschilt weinig van de bloeddruk en het debiet verkregen met simulaties gebaseerd op Poiseuille profielen. De verkregen wandschuifspanning verschilt wel significant tussen de beide modellen. Er is aangetoond dat de geïntroduceerde viscoelastische eigenschappen van de vaatwand significant bijdragen aan de uitdamping van de druk- en debietgolven. Ook wordt de invloed van een stenose in de arteria femoralis en van een aneurysma in de abdominale aorta getoond.

Concluderend: het ontwikkelde ééndimensionale golfvoortplantingsmodel kan gebruikt worden om patiëntspecifieke arteriële systemen te modeleren en daarmee fysiologische data te verkrijgen die relevant kunnen zijn bij de evaluatie van verschillende interventie mogelijkheden in de cardiovasculaire chirurgie.

Dankwoord

Graag wil ik een aantal personen bedanken die bijgedragen hebben aan het tot stand komen van dit proefschrift. Allereerst Frans van de Vosse, die mij de afgelopen jaren zeer enthousiast begeleid heeft. Al sinds mijn stage in Milaan ruim zes jaar geleden heb ik onze gesprekken als zeer prettig en nuttig ervaren. Naast het nodige enthousiasme heb je me vertrouwen gegeven op momenten dat ik er zelf misschien iets minder in geloofde en heb je me gemotiveerd wanneer onder andere de Fransman voor tegenslag zorgde. Daarnaast wil ik ook Marcel Rutten bedanken voor de vele discussie sessies die uiteindelijk hebben bijgedragen in het tot stand komen van deze lees unit. Ook de mensen die betrokken waren bij het Hemodyn project en de Hemoloco bijeenkomsten wil ik bedanken voor de fijne samenwerking en het geven van een frisse kijk op problemen wanneer ik zelf geen oplossing zag.

Het meest sfeerbepalend gedurende de laatste vier jaren op de TU/e zijn toch mijn kamergenoten van WH 4.11 geweest. Berent, Hanna, Ihor, Karlien, Lisette, Martijn, Mirjam, Rolf, Reinder, Tijmen en Wilco; ik heb erg genoten van de etentjes, de verjaardagstaarten en natuurlijk van onze vele gesprekken. Bedankt dat jullie mij de mogelijkheid hebben gegeven om als eerste van onze kamer te promoveren en ik hoop dat hiermee de vloek is opgeheven... Ik zal jullie missen! Heren van het voetbalteam, maar ook de dames en heren waarmee ik regelmatig getennist heb, het sporten en de bijbehorende gesprekken waren een zeer aangename afwisseling op de uren die ik doorgaans achter de pc doorbracht. En als ik het over sporten heb kan ik natuurlijk mijn fitness maatje Raoul niet vergeten. Onze gesprekken tijdens het sporten (of was het meer sporten tijdens onze gesprekken?) waren erg amusant! Ik wens jou en Roosje een hele mooie tijd toe in Wales.

Ook een aantal mensen buiten de werkkring wil ik bedanken. Ten eerste Bart, Oscar en Tijmen; ook al zijn jullie een stelletje wankers (dat snap ik!!), toch kan ik onze vele eten+film avondjes, onze vakanties, Ardennen Offensieven en andere tripjes altijd erg waarderen. Ik hoop dat we hier, ongeacht onze carrière en woonplaats veranderingen nog lang mee door zullen gaan. Ron, jij hebt al sinds het begin van mijn studie een stempel op mijn wetenschappelijke en sociale 'carrière' gedrukt. Je belangrijkste bijdrage was toch wel dat de bierglazen op Stratumseind geen standaard 200 cc maar 150 cc bier bevatten. En Bedankt!

Tijmen, je hebt zowel 'op de zaak' als daarbuiten een belangrijke rol vervuld bij het tot stand komen van dit boekje. Daarnaast zijn we goede vrienden geworden en hebben we veel mooie ervaringen gedeeld! Het is dan ook een eer om jou als paranimf aan mijn zij te hebben. Maud, mijn grote zus! We zijn er altijd al voor elkaar geweest (oké, behalve jouw eerste 16 maanden dan), en we zullen er ook altijd voor elkaar zijn. Het zal dan ook geen wonder zijn dat ik het heerlijk vind om ook jou aan mijn zij te hebben als paranimf.

Pa en Ma, jullie wil ik in het bijzonder bedanken voor alle steun en het onvoorwaardelijke vertrouwen dat jullie altijd in me hebben gehad. Jullie hebben mij gevormd tot wie ik nu ben en daarvoor ben ik jullie eeuwig dankbaar. Zou de 'kliertied' dan toch zijn vruchten afgeworpen hebben!?

De laatste dankwoorden zijn gereserveerd voor mijn Miekie. Jij zorgde er, met je motiverende woorden en je heerlijke humor, iedere avond weer voor dat thuis mijn werk op de tweede plaats kwam. Zonder die ontspannende avonden en weekenden met jou samen was dit boekje er nooit geweest! Sinds jij bij mij woont is thuiskomen écht thuiskomen!

curriculum vitae

David Bessems werd geboren op 16 februari 1977 in Maastricht. In 1995 behaalde hij zijn VWO-diploma aan het Sint-Maartenscollege te Maastricht. Tijdens zijn opleiding aan de Technische Universiteit Eindhoven, faculteit werktuigbouwkunde met als afstudeerrichting Werktuigbouwkundige Medische Technologie, liep hij stage aan de Politecnico di Milano, dipartimento di bioingegneria. Hier deed hij met behulp van de eindige elementen methode onderzoek naar de bloedstroming in de aortaboog van kinderen waarbij als gevolg van een geboren hartafwijking een Fontan procedure is uitgevoerd. Zijn afstudeerwerk aan de faculteit Werktuigbouwkunde bestond uit het ontwikkelen en valideren van een nieuwe driedimensionale elementvorm die met behulp van de eindige elementen methode gebruikt kan worden om vloeistofstroming in ongestructureerde domeinen te analyseren. In 2003 studeerde hij af waarna hij startte met een promotieonderzoek aan de faculteit Biomedische Technologie van de Technische Universiteit Eindhoven. Dit promotie onderzoek heeft hij gedaan binnen de vakgroep Cardiovasculaire Biomechanica en heeft geleid tot dit proefschrift.

